Delft University of Technology

MSE MSc Thesis
MS53035

Extending the Lifespan of HVAF Sprayed Hastelloy Coatings in H$_2$S-Containing Environments by Using Sol-Gel Sealants

---

Date: August 18, 2025

Student: Yu-Shen Chiang

Number: 5920310

Supervisors: Prof. Yaiza Gonzalez-Garcia (TU Delft MSE)

Ir. Frank van der Klift (Shell Pernis)

ACKNOWLEDGEMENT

I ABSTRACT

This research study aims to enhance the performance and extend the service life of High Velocity Air Fuel (HVAF) sprayed Hastelloy C276 corrosion resistant coatings in hydrogen sulfide (H_2S)-containing environments. A sol-gel sealing strategy using SiO_2/ZrO_2 as the primary sealing material was employed to improve the mechanical strength, corrosion resistance, and hydrogen induced cracking (HIC) resistance of the coated system under H_2S-containing conditions. Dip coating was used to deposit sol-gel layers with two different thicknesses, including two-layer and five-layer systems. The coated samples were evaluated through microhardness testing, tribological wear testing, electrochemical characterization (open circuit potential (OCP), potentiodynamic polarization (PDP), and electrochemical impedance spectroscopy (EIS)), and an immersion test in an H_2S environment following the NACE TM0284 standard.

Electrochemical results revealed that the sample with five layers of SiO_2/ZrO_2 sol-gel sealant exhibited the lowest corrosion rate and the highest impedance after 21 days of corrosion exposure. Both adding two-layer and five-layer sol-gel sealed samples demonstrated significantly lower corrosion rates compared to the unsealed HVAF Hastelloy C276 coated sample, and the performance improvement correlates with the number of sol-gel layers. However, in terms of wear resistance, microhardness, and HIC resistance, the addition of the sol-gel layer did not result in noticeable improvements. This lack of enhancement is likely due to the limited thickness of the sol-gel film, which may not provide sufficient mechanical reinforcement or protection against external corrosive substances in such aggressive environments.

To sum up, although the proposed SiO_2/ZrO_2 sol-gel sealing layer did not significantly prolong the lifetime of HVAF sprayed Hastelloy C276 coatings under H_2S exposure, it did exhibit excellent anti-corrosive performance in the air. This suggests its potential applicability as a cost-effective protective strategy in industrial settings where H_2S-containing environments are not present.

II CONTENTS

III   LIST OF ABBREVIATIONS

HE Hydrogen Embrittlement

HIC Hydrogen Induced Cracking

SSC Sulfide Stress Cracking

SCC Stress Corrosion Cracking

HSC Hydrogen Stress Cracking

CTR Crack Thickness Ratio

HVAF High Velocity Air Fuel

PC Pitting Corrosion

CF Corrosion Fatigue

HELP Hydrogen Enhanced Localized Plasticity

HEDE Hydrogen Enhanced Decoherence

AIDE Adsorption Induced Dislocation Emission

PWHT Post-Weld Heat Treatment

HVOF High Velocity Oxygen Fuel

D-Gun Detonation Gun

APS Atmospheric Plasma Spray

VPS Vacuum Plasma Spray

CGSM Cold Gas Spraying Method

WS Warm Spray

CIS Conventional Impregnation Sealing

UES Ultrasonic Excitation Sealing

VC Vacuum Sealing

CLR Crack Length Ratio

MAO Micro-Arc Oxidation

EIS Electrochemical Impedance Spectroscopy

CVD Chemical Vapor Deposition

ALD Atomic Layer Deposition

UMAO Ultrasonic Micro-Arc Oxidation

TEOS Tetraethoxysilane

γ-MAPTS γ-Methacryloxypropyltrimethoxysilane

HF Hydrofluoric Acid

OCP Open Circuit Potential

PDP Potentiodynamic Polarization

SEM Scanning Electron Microscopy

TTIP Titanium Isopropoxide

WE Working Electrode

RE Reference Electrode

CE Counter Electrode

SCE Saturated Calomel Electrode

SHE Standard Hydrogen Electrode

AC Alternating Current

OM Optical Microscopy

EDS Energy Dispersive Spectroscopy

Ra Arithmetic Average Roughness

Rz Maximum Profile Height

Rq Root Mean Square Roughness

CSR Crack Sensitivity Ratio

SOHIC Stress Oriented Hydrogen Induced Cracking

PVD Physical Vapor Deposition

WAS Waterborne Silicone Modified Acrylic Sealant

IV LIST OF FIGURES

V LIST OF TABLES

1   INTRODUCTION

Petroleum and natural gas are valuable resources on Earth, driving more than half of the world's energy demands [13]. The demand for petroleum products also plays a crucial role in population growth and industrial development. With the increasing need for new sites for crude oil and natural gas, as well as their ongoing discovery, oil and gas are frequently transported through pipelines that span distances ranging from a few kilometers to thousands of kilometers [14]. These pipelines are primarily made of carbon steel. In addition to pipelines, various units in the petroleum industry, such as reactors and catalyst regenerators, also have walls constructed from carbon steel. However, these carbon steel components face significant corrosion related challenges, which represent a common and critical issue in the oil and gas industry. Harsh and corrosive operating environments often lead to various corrosion mechanisms, resulting in equipment and infrastructure failures that pose risks to health, safety, and the environment [15].

Among the various industrial corrosion mechanisms, acidic corrosion is the most prevalent in the oil and gas industry. It typically occurs when metals are exposed to dissolved wet hydrogen sulfide (H_2S). On average, acidic corrosion accounts for approximately 18% of total failures in the oil and gas sector annually. This type of corrosion can be further classified into hydrogen embrittlement (HE), hydrogen induced cracking (HIC), sulfide stress cracking (SSC), and so on [13]. Among these, hydrogen induced cracking is the most prevalent in oil pipelines constructed from plate materials, which leads to the degradation of mechanical properties. When carbon steel is exposed to an environment containing hydrogen sulfide (H_2S), the hydrogen atoms, which are formed by the reaction of H_2S reacting with Fe [16]. Hydrogen atoms that diffuse into the interior of carbon steel tend to accumulate at defects such as grain boundaries, dislocations, and vacancies. These hydrogen atoms then recombine to form molecular hydrogen (H_2). As the concentration of hydrogen gas increases, bubbles are formed, generating internal pressure. When the internal pressure exceeds the material's tolerance limit, microcracks develop and gradually propagate, ultimately leading to ductile or even brittle fracture of the carbon steel [17–19].

A previous study [6] demonstrated a corrosion resistant alloy, $Ni_{57}Cr_{15}Mo_{16}W_4$ (commercially known as Hastelloy C276), which is suitable for acidic environments, can be effectively applied as a coating on carbon steel surfaces using high velocity air fuel (HVAF) spraying technology to prevent HIC. This approach successfully mitigates the corrosion issues of carbon steel. However, it was also observed that the corrosion potential of the Hastelloy C276 coating is higher than that of carbon steel. This implies that in scenarios where the coating is damaged or contains defects, galvanic interactions could accelerate the corrosion of the substrate. This study also confirmed that a 250 μm coating exhibits superior corrosion resistance compared to 375 μm and 500 μm coatings, attributed to its lower residual stress, resulting in a reduced corrosion rate. However, the 250 μm coating had larger pore sizes and a higher fraction of porosity than the thicker coatings, leading to reduced mechanical strength and wear resistance. Consequently, the likelihood of corrosive substances penetrating the coating increases, making the longevity of the 250 μm coating the shortest among the tested thicknesses.

This study aims to explore strategies for extending the service life of 250 μm-thick HVAF sprayed Hastelloy C276 corrosion-resistant coatings. Given that HVAF is a relatively novel and costly technique, increasing the thickness of coating further raises the overall expense. As a result, this research focuses on the 250 μm coating thickness, among the mentioned options, the thinnest and least expensive, but also with the shortest expected lifespan, to evaluate its performance and potential enhancement. Inspired by the work of Huang et al., who proposed that dual-layer coating systems can serve as effective solutions to improve durability [20], this research adopts a similar approach. Specifically, two-layer and five-layer SiO_2/ZrO_2 sol-gel sealants were applied on top of 250 μm thick Hastelloy C276 HVAF coatings. These sol-gel layers are designed to act as protective barriers, preventing the ingress of moisture, oxygen, and other corrosive agents, while also indirectly shielding the underlying metallic coating from mechanical damage.

To evaluate the effectiveness of the sol-gel sealing layers, a comprehensive set of tests was conducted from three perspectives, mechanical properties (including wear resistance and microhardness), corrosion resistance, and resistance to HIC in sulfide-rich environments. HIC resistance is listed separately from corrosion resistance here because their mechanisms are entirely different. The mechanism of HIC resistance involves hydrogen penetrating into the material, with the corrosive medium being wet hydrogen sulfide and acidic environments. In contrast, the mechanism of corrosion resistance involves surface oxidation, with the corrosive medium being oxygen and moisture. By comparing the performance of the samples with and without the sol-gel layer, this study assesses whether the addition ofSiO_2/ZrO_2 sol-gel is a viable strategy to enhance the durability and performance of HVAF Hastelloy C276 coatings under aggressive conditions. Furthermore, the study investigates whether increasing the number of sol-gel layers leads to incremental improvements in protection and performance.

2 THEORETICAL BACKGROUND

The following sections will provide a detailed overview of the theoretical background relevant to this study. The topics include the HIC corrosion mechanisms associated with hydrogen sulfide (H_2S), thermal spray techniques and high velocity air fuel (HVAF), and some information of sealants.

2.1 HYDROGEN SULFIDE (H_2S) AND HYDROGEN INDUCED CRACKING (HIC)

In petroleum industry applications, the most common corrosion mechanisms for carbon steel include hydrogen embrittlement (HE), hydrogen-induced cracking (HIC), pitting corrosion (PC), corrosion fatigue (CF), and sulfide stress cracking (SSC). These mechanisms can lead not only to crack formation or localized pitting but also to wall thickness loss. As a general reference, the wall loss rate is typically around 0.10–0.30 mm/year. Among these five corrosion mechanisms, only CF can occur without the presence of moisture, whereas the other four are classified as aqueous corrosion, requiring a humid environment to develop. Among them, HE, HIC, SSC are triggered by the hydrogen atoms, which are generated by the reaction of steel with H_2S. These corrosion phenomena result in degradation or deterioration of material performance. The underlying cause of corrosion lies in the chemical or electrochemical interactions between the material and its environment. The following sections provide a brief introduction to the chemical H_2S, and a detailed discussion of HIC, which is the main corrosion mechanism of this study [13].

2.1.1 Hydrogen Sulfide (H_2S)

Crude oil is the primary source of hydrogen sulfide (H_2S) in refineries. The primary sources of H_2S in oil and gas pipelines can be broadly classified into three categories. First, natural formation within geological reservoirs, where certain oil and gas fields contain acid gas reservoirs. In these cases, sulfide minerals or sulfur salts present in formation water decompose under high temperature and high pressure conditions, producing H_2S that is carried into the pipelines along with crude oil or natural gas. Second, formation via chemical reactions, in which organic sulfur compounds in crude oil, such as thiols and sulfides, undergo thermal decomposition at elevated temperatures, or where acidic fluids react with sulfide deposits to release H_2S. Third, thermal decomposition of sulfur-containing additives or corrosion inhibitors, as well as anaerobic reduction reactions occurring during storage and transportation, can also contribute to H_2S generation. Hydrogen sulfide is a toxic, corrosive, colorless, and flammable gas with a strong. When gaseous H_2S dissolves in water, it forms hydrogen sulfide in its aqueous state, $H_2S(aq)$, a weakly acidic solution. In aqueous media, H_2S readily dissociates into bisulfide ions but does not fully decompose into sulfide ions. When exposed to air, H_2S rapidly oxidizes due to the presence of free radicals and other oxidizing agents, forming sulfate and sulfur dioxide (SO_2). The figure below summarizes the physical and chemical properties of H_2S [21, 22].

When H_2S gas dissolves in water, forming aqueous hydrogen sulfide, the overall environment becomes acidic. Upon dissolution, H_2S rapidly ionizes, producing H^+ and HS^- ions. Additionally, the HS^- ions may undergo secondary ionization, releasing a small amount of S^{2-} ions and additional H^+ ions. The ionization reactions of H_2S are represented by the following equations:

$$H_2S \rightleftharpoons H^+ + HS^- \tag{1}$$

$$HS^- \rightleftharpoons H^+ + S^{2-} \tag{2}$$
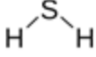
Characteristic	Detail
Chemical structure	H–S–H structure
Molar weight	34.08 g mol^{-1}
Odor	Offensive and strong odor of rotten eggs
Color	Colorless
Taste	Sweetish taste
Density	1.5392 g/L
Specific gravity	1.189
Boiling point	−60.25 °C
Melting point	−82 °C
Physical state	Gas
Upper explosive limit (UEL)	44%
Lower explosive limit (LEL)	4%
Auto-ignition temperature	500 °F (260 °C)
Henry's law constant at 25 °C	$0.0098 \text{ atm-m}^3/\text{mol}$
Vapor pressure at 25 °C	13,600 mmHg
Solubility in water (H_2O)	4 g dm^{-3} (at 20 °C)

Figure 1: The list of physical and chemical properties of H_2S [1]

When H^+ ions come into contact with the steel surface, they acquire electrons from the metal and undergo a reduction reaction, forming hydrogen atoms, which subsequently combine to produce hydrogen gas (H_2). This process represents the cathodic reaction, as shown in Equation 3. On the other hand, metal atoms tend to release electrons. Taking iron (Fe), the primary component of the substrate used in this study, as an example. After Fe releases electrons, it reacts with sulfide ions (S^{2-}) to form iron sulfide (FeS), which constitutes the anodic reaction. This process is illustrated in Equation 4 and 5 [1].

$$2\,H^+ + 2\,e^- \longrightarrow 2\,H \tag{3}$$

$$Fe \longrightarrow Fe^{2+} + 2\,e^- \tag{4}$$

$$Fe^{2+} + S^{2-} \longrightarrow FeS \tag{5}$$

$$Fe + H_2S \longrightarrow FeS + 2\,H\,(H_2) \tag{6}$$

From the total reaction equation (Equation 6), it can be inferred that an increase in the partial pressure of H_2S leads to a decrease in the solution's pH, thereby accelerating metal corrosion. Furthermore, in the

presence of H_2S or HS^-, the conversion of hydrogen atoms into molecular hydrogen is inhibited, resulting in the accumulation of excess hydrogen atoms and an increase in internal pressure. These excess hydrogen atoms can induce hydrogen embrittlement in steel or diffuse into the metal, accumulating as hydrogen gas and causing hydrogen induced cracking (HIC). The detailed mechanisms of these processes will be elaborated in the following sections [1].

2.1.2 Hydrogen Induced Cracking (HIC)

As mentioned previously, hydrogen induced cracking (HIC) is a common corrosion mechanism in the petroleum industry. HIC shares some similarities with hydrogen embrittlement as both involve material degradation caused by hydrogen atoms. HIC occurs when hydrogen atoms from the environment diffuse into a metallic material, accumulate at defects, and form molecular hydrogen gas. The hydrogen gas creates high internal pressures, eventually leading to crack initiation and material failure. Although HIC and HE are somewhat similar, there are notable differences between the two. Hydrogen embrittlement is characterized by a loss of ductility due to the presence of hydrogen atoms in the metal lattice, without the precipitation of molecular hydrogen within the material. Additionally, hydrogen embrittlement can affect a wide range of metals and occurs under various conditions, including mild environments or dry hydrogen atmospheres. Furthermore, hydrogen embrittlement is often reversible; once hydrogen is removed from the material, its ductility can be restored. In contrast, HIC primarily affects non-austenitic steels and occurs under aqueous conditions, resulting in irreversible damage to the material. The following paragraphs will provide a more detailed explanation of the mechanisms underlying HIC [2, 23, 24].

In acidic environments, steel can undergo various corrosion processes. Among them, the primary concern for hydrogen induced cracking (HIC) is the absorption of atomic hydrogen, as a prerequisite for HIC is the significant ingress of hydrogen into carbon steel. The degree of hydrogen absorption depends on several environmental factors, including temperature, pH, and the partial pressures of H_2S, CO_2, and H_2O. Moreover, stress oriented hydrogen induced cracking (SOHIC) and blistering are also related to hydrogen induced cracking, all of them are degradation mechanisms associated with the formation of hydrogen blisters in the metal that occur when it is charged with atomic hydrogen produced by aqueous corrosion of the metal surface. These hydrogen-charging conditions are commonly produced by corrosion in the presence of water and hydrogen sulphide (H_2S). The H_2S also serves as a poison to the recombination of atomic hydrogen to form molecular hydrogen gas, thus promoting entry of the atomic hydrogen into the metal. [2, 25].

During H_2S exposure, FeS_{1-x} compounds form on the surface. Simultaneously, the anodic dissolution of iron reduces hydrogen ions to atomic hydrogen, which can diffuse into the steel matrix. High concentrations of H_2S increase the formation of FeS_{1-x}, acidify the steel surface, and enhance the absorption of hydrogen ions by the metal [2, 26, 27].

In addition to H_2S, other environmental factors, such as pH, play a crucial role in the hydrogen charging process. Generally, lower pH values (more acidic environments) tend to increase hydrogen uptake. A combination of low pH and high H_2S concentrations results in the maximum diffusion of hydrogen into the material [28].

Once hydrogen atoms enter the crystal lattice, they diffuse through interstitial sites according to Fick's laws of diffusion, ideally forming a predictable distribution. However, various microstructural features in the material act as traps that alter the distribution profile of hydrogen in steel. These hydrogen capture traps are classified as reversible or irreversible, depending on the difficulty of releasing the trapped hydrogen. Grain boundaries and dislocations are typically considered reversible traps, while incoherent precipitates are categorized as irreversible traps.These traps capture hydrogen atoms that have diffused into the structure, allowing them to accumulate and form molecular hydrogen, which increases the internal pressure. Once the amount of hydrogen reaches a critical level, cracks begin to initiate [2].

When the concentration of hydrogen atoms at certain trapping sites exceeds the solubility limit of the material, molecular hydrogen precipitates from the lattice. This molecular hydrogen, or hydrogen gas, is considered a critical factor for crack initiation. Because molecular hydrogen has a larger volume than atomic hydrogen, it cannot be accommodated within the same space, thereby creating pressure that induces cracks to open and form additional voids. Consequently, internal cracks are formed by the accumulation of gaseous hydrogen at various defects, such as micropores or inclusions. Once a crack forms, continued accumulation of gaseous hydrogen at the crack site increases internal pressure, driving crack propagation. Conversely, if insufficient hydrogen is introduced into the material to maintain adequate pressure within the crack, its propagation will cease. If the crack reaches the surface of the steel, the hydrogen gas escapes into the environment [2, 29].
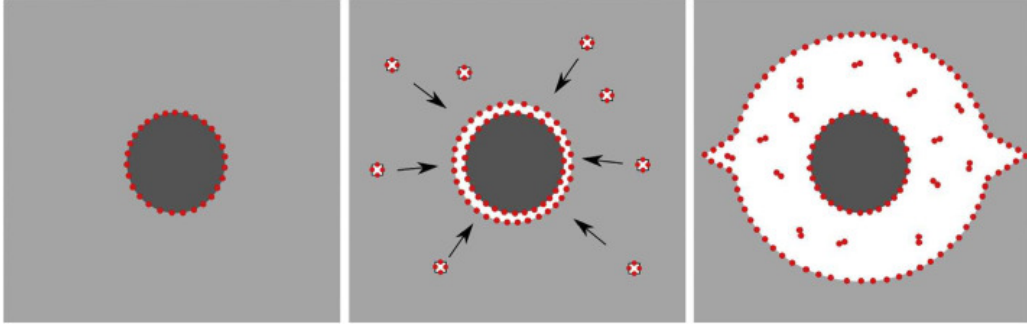
Figure 2: Schematic diagrams of the mechanism of hydrogen induced cracking [2].

Figure 2 illustrates the mechanism of hydrogen induced cracking. In the schematic, the dark gray circles represent inclusions, the light gray areas represent the matrix, and the red dots represent hydrogen atoms. In the first image at the left-hand side , hydrogen atoms are trapped along the interface between the inclusions and the matrix. In the second image, the interface between the inclusion and the matrix has opened, with both free surfaces decorated by hydrogen atoms. Vacancies containing hydrogen diffuse toward the interface, further increasing the open volume. Then, in the final image, hydrogen gas precipitates within the expanded volume, initiating the formation of cracks.

From the previous discussion, it is evident that hydrogen induced cracking (HIC) can occur without the application of external stress. However, when external stress is present, it influences the crack propagation direction, a phenomenon known as stress oriented hydrogen induced cracking (SOHIC). External stress can either mitigate or exacerbate the internal stress generated by hydrogen gas or bubble pressure within the crack, thereby affecting the location of crack nucleation and linkage. If stress is applied after crack nucleation, the impact of external stress can be observed as the crack reorients its propagation direction, leading to more complex crack morphologies [30–32].

When HIC occurs near the steel surface, the pressure within the cracks can elevate the surface layer, resulting in noticeable deformation known as blistering. These blisters typically appear as circular formations on surfaces exposed to the corrosive environment, which is shown as Figure 3. Due to their proximity to the surface, cracks forming these gas-filled bubbles often curve toward the surface as a result of intense hydrogen-assisted shear stress ahead of the crack tip. Eventually, these cracks may intersect with the surface, at which point the hydrogen gas is released, halting further crack and bubble growth. Blistering frequently occurs alongside HIC and appears so similar that many studies speculate they may represent the same underlying phenomenon. However, a key distinction lies in the location and visibility of blistering. It occurs near the free surface and is accompanied by noticeable surface elevation, making it visible to the naked eye or under low-magnification optical microscopy. Therefore, blistering can serve as a visual indicator of HIC occurrence and is one of the most straightforward effects to measure [2, 33, 34].

To prevent or mitigate hydrogen blistering, HIC, and SOHIC, several methods are commonly employed indi-
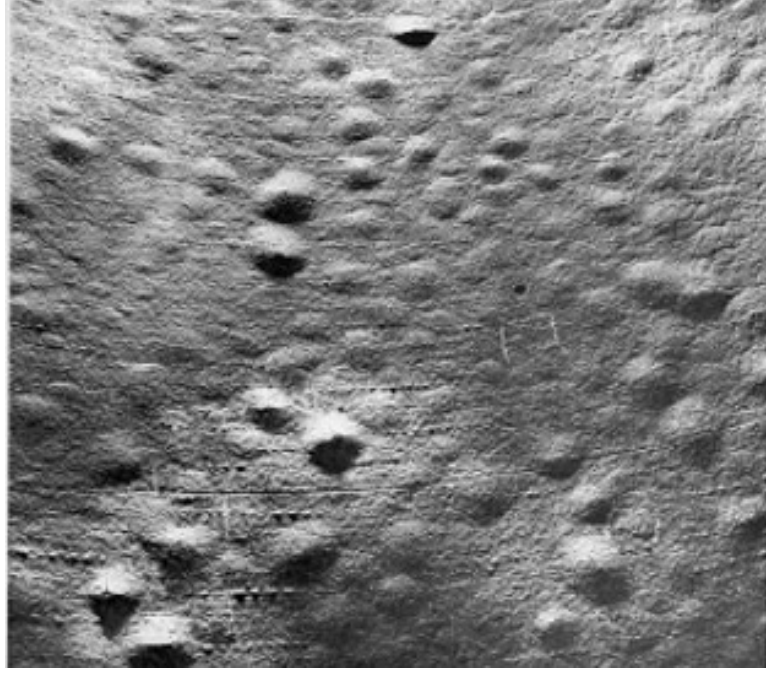
Figure 3: Blisters on carbon steel vessel wall [3].

vidually or in combination. First, heat treatment of the base material, such as normalization or quenching and tempering, can refine the grain structure and reduce banded microstructures, thereby enhancing material resistance. Second, post-weld heat treatment (PWHT) is effective in relieving residual stresses, thereby lowering the risk of SOHIC, although its effectiveness in preventing hydrogen blistering or HIC is limited. Additionally, specially designed "HIC resistant" steels typically maintain sulfur content at $<0.002\%$ and may include small amounts of calcium to modify the morphology of sulfide inclusions. This is often combined with appropriate heat treatment of the base material. In operational settings, the working environment's pH can be adjusted through surface weld overlays or the addition of neutralizing agents. For wet high-temperature operations, it is recommended to maintain the material at elevated temperatures for at least one hour per 25 mm of metal thickness to reduce the risk of crack formation [3].

2.2 THERMAL SPRAY AND HIGH VELOCITY AIR FUEL (HVAF)

Surface coating technology is an essential and economical method for protecting substrates from external erosion, corrosion, and wear. As mentioned earlier, for carbon steels used in petroleum environments, such as carbon steel S235JR, hydrogen induced cracking, sulfide stress cracking, and hydrogen embrittlement are common corrosion mechanisms in H_2S environments. Thermal spraying is an effective method to protect the carbon steel substrate, and different coating techniques and materials can be selected based on specific requirements to achieve the desired performance. Thermal spraying is one of the most effective methods for protecting new components against wear, high-temperature corrosion, residual stress, and erosion. It provides hard and dense coatings that significantly enhance material lifespan. The fundamental mechanism of thermal spraying is relatively straightforward. It involves feeding powdered, wire-like, or rod-like materials, such as metals, ceramics, cermets, and certain polymers, into a spray gun. Using a high-temperature heat source, heating the coating material to a molten or semi-molten state. Compressed air or flame flow is then employed to accelerate the molten material, forming a high-velocity particle stream that is deposited onto a pre-treated substrate surface. This process creates coatings with specific functional properties, such as wear resistance, corrosion resistance, high-temperature resistance, oxidation resistance, insulation, and thermal barrier performance [35, 36].

Thermal spraying technology has become increasingly mature and is widely applied in critical industrial sectors for wear resistant and corrosion resistant coatings, including aerospace, automotive, power generation, petrochemical, and offshore operations. One of the key advantages of thermal spraying is its ability to accommodate an extensive variety of materials. Virtually any material that can melt without decomposition is suitable for this process, making it highly versatile. Another notable advantage is that most thermal spray processes can apply coatings without significantly heating the substrate. As a result, even coatings made from materials with very high melting points can be deposited without altering the substrate's properties or causing thermal deformation. Additionally, thermal spray coatings can, in most cases, be stripped and reapplied without affecting the substrate's characteristics or dimensions, allowing for the restoration of worn or damaged coatings. Despite its numerous advantages, the primary limitation of thermal spraying lies in its substrate size constraints. It is particularly challenging to coat small, deep, or highly complex substrates using this method. Figure 4 illustrates the main schematic of the thermal spraying process [35].
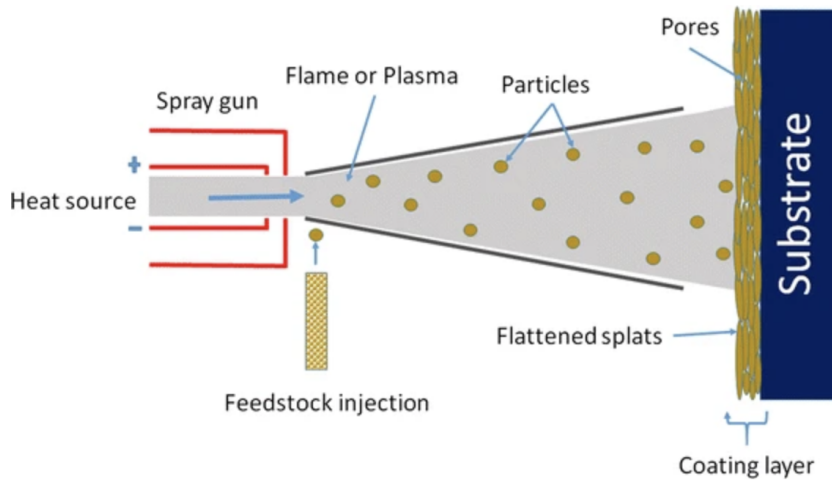
Figure 4: The schematic of typical thermal spray deposition process on flat substrate [4].

According to the development history of thermal spray technologies, they can be broadly categorized into three main types based on their specific characteristics. Figure 5 presents a classification of various thermal spray techniques in the form of a family tree.
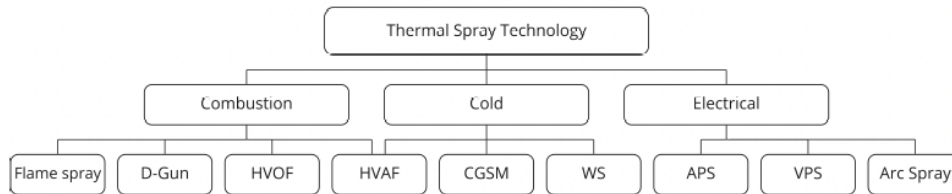
Figure 5: Family tree of the thermal spray technology [5, 6].

From the diagram above, it can be observed that high velocity oxygen fuel (HVOF), detonation gun (D-gun), and flame spray are classified under the "Combustion" category. This category represents the most fundamental method of thermal spraying, where powdered metal is melted and propelled onto a surface to form a coating. This system utilized the combustion of fuel and oxygen to generate a flame, which melted the metal wire. The molten metal was then atomized by compressed gas and sprayed onto a substrate, forming a coating. This process, now known as flame spraying, was initially limited to low melting point metals such as tin and lead

due to temperature constraints. However, subsequent technological advancements based on flame spraying led to the development of modern thermal spray techniques, including HVOF, which is the most popular thermal spray technique these days.

However, in response to the demand for corrosion resistant coatings for novel metals, arc-based thermal spray technology was introduced. This represented the second major category of thermal spray techniques, leveraging electrical energy to increase the working temperature of the machine, making it enable the spraying of higher melting point metals such as steel, zinc, and stainless steel. Technologies like atmospheric plasma spray (APS), vacuum plasma spray (VPS), and arc spray fall into this category.

The third and most recent category of thermal spray technology involves solid-state spraying. This process, known as cold spraying, achieves coatings without combustion or electrical energy. Cold spray is a unique solid-state process that derives its high kinetic energy from particle velocity rather than thermal energy. The lower operating temperature of cold spraying offers several advantages, such as control over the microstructure, reduced oxidation, and minimized porosity in the coating. Since this technique operates below the melting temperature of the feedstock material, it requires particles to undergo plastic deformation solely through kinetic energy in their solid state, limiting its applicability to specific materials. Techniques such as cold gas spraying method (CGSM), high velocity air fuel (HVAF), and warm spray (WS) fall under this category.

The HVAF technique used in this study is an advanced method that has garnered significant attention in recent years. Derived from the HVOF process, HVAF replaces pure oxygen with compressed air, which acts as both a coolant and a means of increasing the pressure within the combustion chamber.Its process operates by mixing gaseous fuel with compressed air, which is combusted in a combustion chamber to generate high-temperature, high-pressure gases. These gases are then accelerated through a specially designed nozzle, producing a high velocity gas stream. The coating material, in the form of powder, is heated to a semi-molten state and propelled at extremely high velocities toward the substrate. Upon impact, the powder particles rapidly cool, forming a dense and strongly adherent coating. HVAF operates at a combustion temperature of approximately 1,900°C, which is lower than other thermal spray techniques, such as high velocity oxygen fuel (HVOF). This lower temperature minimizes oxidation and decomposition of the coating material while achieving higher particle velocities, resulting in superior coating quality. Due to its ability to control the microstructure, reduce oxidation, and minimize porosity in the coating, the HVAF technique has been selected for coating Hastelloy C276 in this study [7]. Figure 6 provides a schematic representation of the HVAF system.
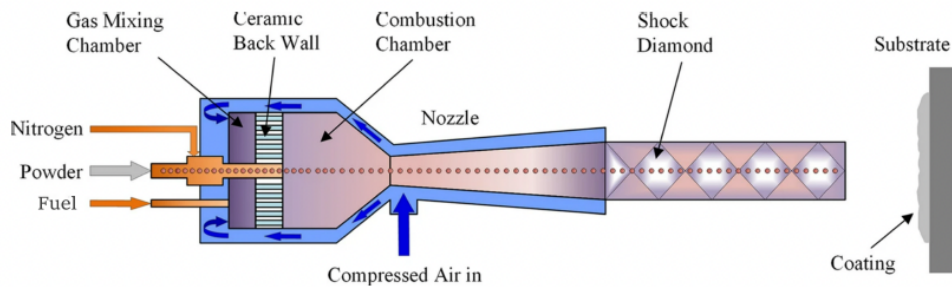
Figure 6: The schematic diagram of HVAF processes [7].

Since thermal spray coatings are composed of multiple particles, then these molten or semi-molten particles impact the substrate at high speed, flattening and solidifying into lamellar structures. The coating primarily adheres to the substrate through mechanical interlocking, with some metallurgical bonding. To achieve a uniform coating, the lamellae should be tightly stacked. However, various external factors, including temperature, impact velocity, spray angle, and particle oxidation, can influence the stacking process. The substrate's roughness and temperature variations also affect lamellar stacking. If spraying conditions are suboptimal, the lamellae

may fracture, leading to reduced adhesion, increased oxidation, and the formation of pores. Fracturing is mainly caused by localized stress, which can be mitigated through appropriate surface treatment and optimized spray conditions. Utilizing high particle velocity and lower temperature thermal spraying minimizes the risk of complete particle melting, reduces fragmentation, and enhances coating quality. Figure 7a illustrates a schematic of a HAVF thermal spray coating structure, highlighting defects such as porosity, oxides, and unmelted particles, while Figure 7b presents a cross section of an actual HVAF thermal spray coating [7–9, 37].

(a)   (b)
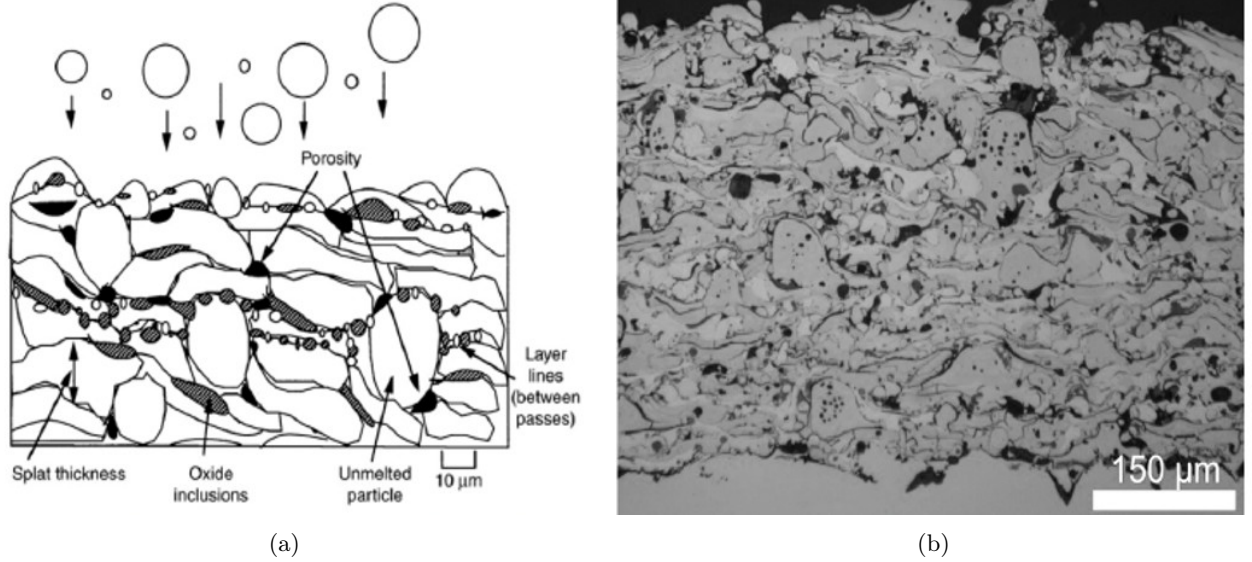
Figure 7: (a) Schematic of HVAF thermal sprayed coating microstructure [8]. (b) Cross section of a HVAF thermal sprayed coating [9].

During the formation of thermal spray coatings, porosity is inevitable. Irregular stacking, lamellar fracturing, and poor wetting contribute to porosity formation, making it one of the primary defects in thermal spray coatings. Among these, microcracks represent a specific type of porosity caused by stress accumulation during cooling, particularly in brittle materials, making ceramic coatings especially susceptible. Porosity can be categorized as either interconnected or closed. Interconnected porosity creates pathways for corrosive substances to penetrate, reducing adhesion and leading to delamination or corrosion reactions. In contrast, closed porosity compromises the coating's wear and corrosion resistance. The primary advantage of using HVAF technology in this experiment lies in its lower combustion temperature, which reduces particle overheating and oxidation, maintaining particles in a semi-molten state and enhancing coating density. Moreover, HVAF achieves higher particle velocity (800–1,200 m/s) compared to other techniques, resulting in greater plastic deformation upon impact, which helps fill voids and improve compaction. Additionally, lower thermal stress minimizes microcrack and porosity formation which leading to a more uniform coating. Because HVAF uses compressed air as the oxidant, oxide inclusions are significantly reduced, further decreasing porosity. Ultimately, HVAF coatings achieve higher density than HVOF coatings, offering superior wear and corrosion resistance [38, 39].

As previously mentioned, one of HVAF's key advantages is its ability to minimize oxidation within the coating efficiently. This is particularly critical because oxidation negatively affects the mechanical properties of the coating. Oxide particles can alter the coating's microstructure and ductility, especially in metallic coatings, where metal oxides tend to be brittle and have different thermal expansion coefficients than the base material. Oxidation can occur during particle flight or upon impact and cooling, influenced by particle stream temperature, turbulence, and carrier gas composition. HVOF produces lower air entrainment compared to plasma spraying and arc welding reducing oxidation risk, but the low temperature, high velocity nature of HVAF further decreases the probability of oxidation, making it a superior choice for oxidation-sensitive coatings [40, 41].

2.3   SEALANTS

The following sections will focus on introducing different types of sealants and applicable sealing techniques. Additionally, the importance of sealants will be discussed, along with the impact of porosity on the overall mechanical strength and wear resistance of the coating. Finally, a selection of sealant materials suitable for this experiment will be identified, followed by a more detailed analysis of their properties.

2.3.1   Porosity and the Importance of Sealants

Surface coatings serve as a protective barrier, protecting materials from environmental damage, including friction, wear, corrosion, chemical degradation, water, ultraviolet radiation, chemical exposure, contaminants, and so on. These coatings are essential for protecting substrates by enhancing material properties, functionality, and durability through their role as damage barriers [42–44]. Depending on environmental requirements, various organic, inorganic, and metallic coatings can be selectively applied to surfaces. Such coatings play a crucial role in improving corrosion and wear resistance, effectively extending the service life and performance of materials under diverse conditions [38, 45–47].

However, porosity within the coating remains a critical challenge, as it facilitates the infiltration of corrosive agents through interconnected pores and defects in the coating structure, leading to substrate degradation, especially for thermal spray coatings [48]. One of the most common issues with thermal spray coatings is excessive porosity. Although HVAF technology exhibits lower porosity compared to HVOF or other thermal spray methods [6], this issue still limits the application of HVAF coatings in environments involving corrosive media. These pores and voids are often the primary contributors to substrate corrosion and localized pitting over the coating [49].

The porosity not only reduces the corrosion resistance of the coating-substrate system but also compromises the mechanical properties of the coating, thereby diminishing its wear resistance. Porosity within the coating is also a structural defect that significantly affects its mechanical performance. When external stress is applied, these pores disrupt uniform stress distribution, leading to localized stress concentration. Stress concentration occurs when geometric discontinuities such as pores, cracks, or inclusions cause stress to accumulate in specific regions rather than being evenly distributed. This phenomenon significantly weakens the mechanical integrity of the coating, making it more susceptible to failure. The presence of porosity hinders uniform stress transmission, particularly under tensile or shear stress conditions. Stress at the pore edges is notably higher than in other regions, resulting in localized strength reduction. According to crack propagation theory, pores act as initiation points for microcracks. Under high stress, these cracks propagate along the pores, further compromising the structural integrity of the coating.

Additionally, porosity can interact with other structural defects. For instance, in certain thermal spray coatings, such as plasma sprayed or HVOF coatings, residual gas or unmelted particles may be trapped within the pores. Under high loads or cyclic stress, these gas cavities may collapse, generating microcracks and further reducing coating strength. The collapse of gas cavities can also induce localized embrittlement, accelerating failure under fatigue loading. Porosity also weakens the adhesion strength between the coating and the substrate, increasing the likelihood of delamination under stress. This issue is particularly pronounced in multilayer or functionally graded coatings, where porosity impairs interlayer stress transfer, leading to interfacial slippage or delamination.

The mechanical properties of a coating, including tensile strength, compressive strength, hardness, and toughness, are all adversely affected by porosity. Higher porosity levels reduce the effective load bearing volume of the material, increasing the stress per unit area and making the coating more prone to plastic deformation or brittle fracture. The severity of this effect depends on the size and distribution of the pores. Moreover, porosity undermines the structural continuity of the coating, facilitating crack propagation under external loads, which

may eventually lead to coating failure. This crack propagation follows a chain reaction of stress concentration, crack growth, and ultimate failure. Consequently, coatings with excessive porosity may experience brittle fracture even under relatively low external loads [50–53].

Beyond its impact on mechanical properties, porosity also degrades wear resistance. High porosity reduces material density and strength, accelerating wear rates. As porosity increases, stress concentration and surface roughness also rise, promoting localized wear. During the wear process, pores facilitate the formation and accumulation of debris. In loosely structured coatings, material around the pores is less stable and more prone to detachment during wear, generating fine debris. These debris particles may circulate within the friction interface, exacerbating wear, especially under dry friction conditions, where they can act as abrasive particles, leading to third body wear. As porosity increases, the likelihood of internal debris formation grows, significantly shortening the coating's wear lifespan. Furthermore, coatings with high porosity tend to absorb contaminants, compromising lubrication and further deteriorating wear performance [50, 51].

Therefore, applying a sealant over the coating effectively addresses these issues by sealing pores and cracks, thereby mitigating these defects. Therefore, the sealing process significantly enhances the corrosion and wear resistance of the coating. There are a variety of sealants that can be employed for sealing micropores in coatings, and their classifications will be discussed in the subsequent section [54, 55].

2.3.2 Sol-gel Technique

Pandiyarajan's study summarizes the sealing methods and materials applied to various coating materials, along with the findings of different research efforts. Commonly used sealing technologies, such as vacuum sealing, conventional impregnation sealing, ultrasonic excitation sealing, and sol-gel sealing, are highlighted. These techniques have been shown to significantly enhance the corrosion resistance and mechanical properties of different types of coatings. The following paragraphs will provide a detailed description of the sol–gel method, which is the selected the sealing technique adopted in this study [54].

The sol-gel technique is a wet-chemical technique used to create uniform and dense coatings on substrate surfaces through the hydrolysis and condensation reactions of precursors. The process begins with selecting a suitable metal-organic compound, such as a metal alkoxide, as the precursor, which is dissolved in a solvent with adjustments to achieve optimal reaction conditions. Water is then introduced to induce hydrolysis, forming a sol with nanoscale particles. The sol is applied to the substrate using methods like dip coating, spray coating, or spin coating, which is shown in Figure 9, to ensure uniform distribution. After coating, the sol undergoes a condensation reaction, transforming into a gel, followed by drying to remove residual solvent.

The adhesion of sol-gel sealing layer to metal surfaces is primarily governed by two mechanisms, chemical bonding and physical adsorption. Following hydrolysis and condensation reactions, –OH functional groups formed within the sol-gel network undergo dehydration condensation with hydroxyl groups on the native oxide layer of the metal surface, resulting in the formation of stable M–O–X bonds (Bonding between the metal and SiO_2 or ZrO_2 in this study.) In the early stages of deposition, the coating also adheres through hydrogen bonding and electrostatic interactions. Subsequent thermal treatment promotes further condensation and densification of the network, thereby enhancing the coating's adhesion strength and durability. This method is widely utilized to create functional coatings with specific properties, making it ideal for sealing and protective applications. The flow chart of the sol-gel method overview is displayed in Figure 8 [56–58].

Apart from the high adhesion to the metallic substrate, sol-gel method is also characterized by its low reaction temperature, simple preparation process, and the ability to achieve excellent sealing performance due to the good fluidity of the sol. As a result, many studies have adopted sol-gel techniques for coating sealants [59–62]

Unlike the latter methods, sol-gel does not require expensive equipment or high-vacuum environments and can be
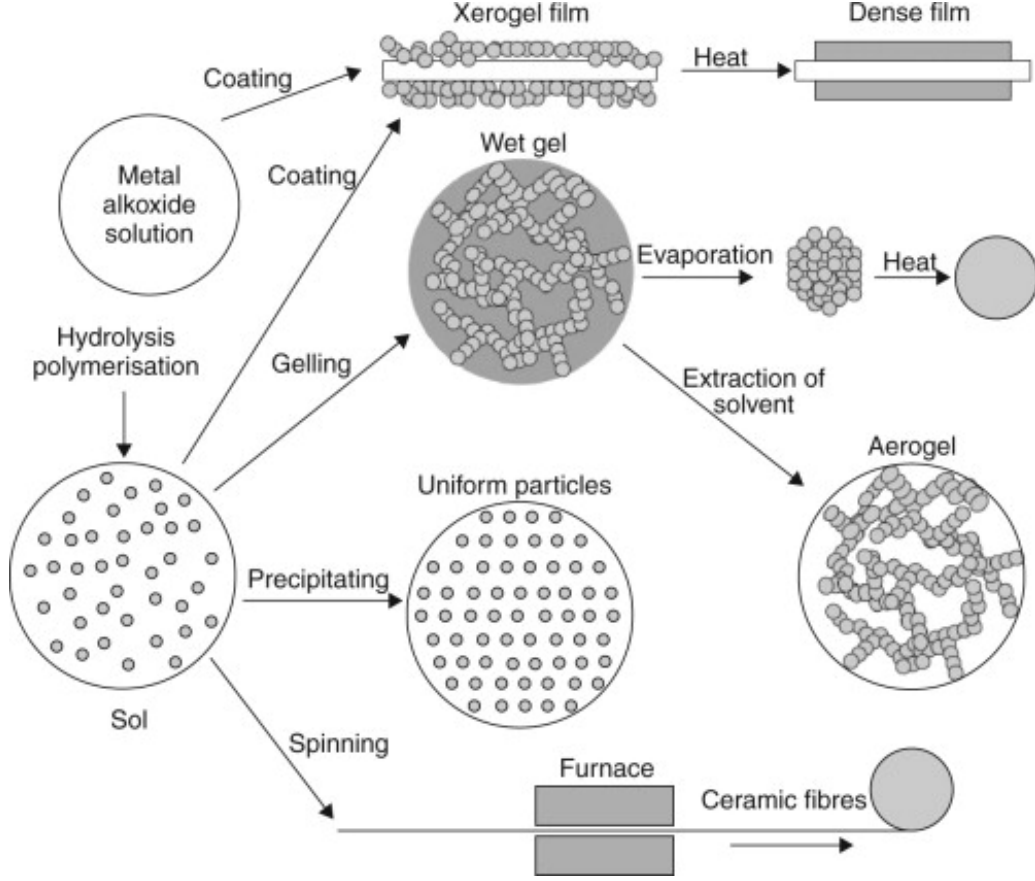
Figure 8: An overview of sol-gel method and their products [10].

conducted under relatively low-temperature conditions, making the operation significantly simpler. Moreover, previous studies have demonstrated that the sol-gel technique can produce uniform coatings at the nanoscale, providing exceptional chemical resistance, corrosion protection, and thermal stability. Additionally, the sol-gel method allows for the use of various coating techniques, enabling the application of coatings on substrates with complex geometries. Therefore, this study will adopt the sol-gel method as the primary sealing technique.

Among the commonly used methods for applying sol-gel sealing layers, dip coating, spin coating, and spray coating are the three most prevalent methods. Figure 9 illustrates schematic diagrams of each method.

Dip coating is the most intuitive and straightforward among the three, particularly suitable for flat or simply shaped substrates. The film thickness can be adjusted by controlling the withdrawal speed and solution properties. In this process, the substrate is vertically immersed into the sol, held for a set dwell time, and then withdrawn at a constant rate. After drying and thermal treatment, a uniform film forms on the substrate surface. The film formation mechanism is governed by the balance of gravitational, viscous, and surface tension forces, and can be described by the Landau–Levich equation, shown in Equation 7, where h is the final wet film thickness (m), η is the dynamic viscosity of the solution ($kg \cdot m^{-1} \cdot s^{-1}$), U is the withdrawal speed ($m \cdot s^{-1}$), γ is the surface tension ($kg \cdot s^{-2}$), ρ is the density of the solution ($kg \cdot m^{-3}$), and g is the gravitational acceleration ($m \cdot s^{-2}$) [63, 64].

$$h = 0.94 \times \frac{(\eta U)^{2/3}}{\gamma^{1/6}\sqrt{\rho g}} \tag{7}$$

Considering this study involved coating two types of substrates: 2.5 cm × 2.5 cm squares and 2 cm × 10 cm rectangular strips. Spin coating was deemed unsuitable for the elongated samples, and spray coating is generally
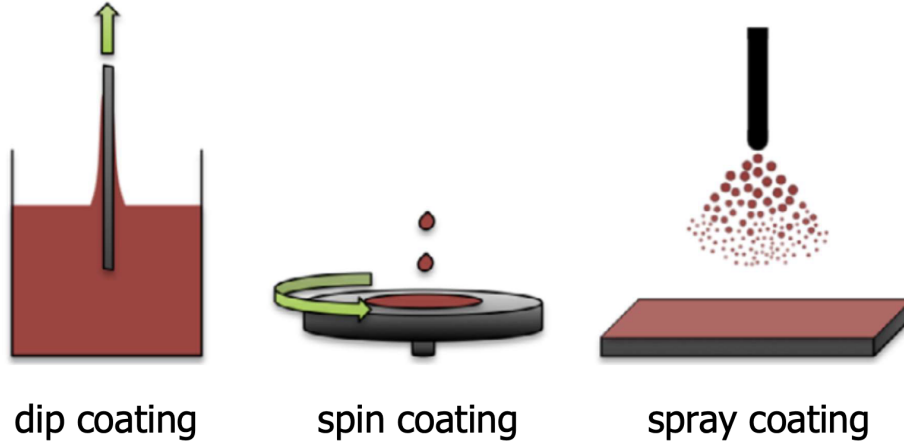
Figure 9: The schematic diagrams of different coating methods in sol-gel process [11].

more appropriate for large-scale applications and requires advanced operator control. Therefore, dip coating was ultimately selected for fabricating the sol-gel thin films in this work.

2.3.3 Material Options for Sealants

Since the application is intended for the petroleum industry, selecting a sealant material requires not only consideration of its corrosion resistance but also its ability to withstand high-temperature environments, which is equally critical. Liquid inorganic or ceramic sealants present an excellent choice as sealant materials. Furthermore, this study will employ the sol-gel method as the sealing approach as mentioned in the previous section. Therefore, in this chapter, the selection of sealant materials is narrowed to liquid inorganic or ceramic sealants that can be synthesized via the sol-gel process. From several literature, Al_2O_3, ZrO_2, TiO_2, and SiO_2 are viable candidates.

Al_2O_3:

Due to its excellent wear resistance, corrosion resistance, and high mechanical strength [65], aluminum oxide (Al_2O_3) has been widely utilized for thin film applications across various fields, including optical lenses and windows, refractory coatings, humidity sensors, anti-corrosion coatings, miniaturized devices, and integrated circuits. The synthesis and application of Al_2O_3 coatings have been achieved through several deposition techniques, such as chemical vapor deposition (CVD), atomic layer deposition (ALD), plasma spraying, magnetron sputtering, and sol-gel processing. Among these methods, sol-gel processing is considered one of the simplest and most versatile approaches, as it allows for deposition through dipping, spraying, or spin coating [66].

Despite existing research on sol-gel derived Al_2O_3 films and its use as a sealing material in some studies, the number of such investigations remains limited. To date, no research has employed the sol-gel method for Al_2O_3 as a sealing coating, particularly for sealing the pores in thermal spray coatings. This limitation may be attributed to several challenges associated with Al_2O_3 sol preparation. The synthesis requires specific precursors such as aluminum isopropoxide ($Al(OC_3H_7)_3$), aluminum chloride ($AlCl_3$), or $Al(NO_3)_3 \cdot 9H_2O$, which are prone to hydrolysis, making the preparation process challenging. Additionally, during the sol-to-gel transition, Al_2O_3 coatings exhibit a higher shrinkage rate compared to SiO_2, TiO_2 and ZrO_2, increasing the likelihood of crack formation. Furthermore, Al_2O_3 requires temperatures above 800 °C to achieve a stable and dense α-phase, whereas conventional sol-gel processing typically involves heat treatment at 400 to 600 °C, preventing the formation of

14

a high-density structure. Consequently, the sealing effectiveness of Al_2O_3 coatings remains suboptimal. Given the availability of alternative materials with superior performance, Al_2O_3 has not been widely adopted as a primary sealing material [67, 68].

SiO_2:

Another material option that is suitable for fabricating sealing coatings on Hastelloy C276 using the sol-gel method is silicon dioxide (SiO_2). SiO_2 can resist the corrosive effects of most acids, bases, and salts, and its high melting point (about 1700°C) ensures that it remains stable without decomposition or degradation even in high-temperature environments. Additionally, SiO_2 has a dense structure, exhibiting extremely low permeability to water molecules and other corrosive agents such as oxygen. Furthermore, its high hardness and excellent wear resistance provide effective protection for the underlying material against mechanical damage and external abrasion. These attributes make SiO_2 an excellent choice for sealing coatings designed to enhance the performance and durability of bottom materials [69–72].

The studies by Sun [73] and Liu [74] collectively highlight the effectiveness of SiO_2 in sealing micropores on coatings or substrate surfaces. Due to its small particle size, SiO_2 can penetrate and fill most surface defects efficiently. Although SiO_2 is generally chemically stable, it may degrade under certain acidic conditions, particularly in the presence of hydrofluoric acid (HF), where it reacts with fluoride ions to form soluble $SiF_6{}^{2-}$ complexes. Even in non-HF acidic environments, SiO_2 may undergo slow dissolution. Despite the predominance of hydrogen sulfide in many operational environments, the possibility of SiO_2 dissolution cannot be ruled out. Consequently, numerous studies have explored the incorporation of additional precursors during the sol-gel synthesis to create composite sols. This approach retains the strong penetration capability of SiO_2 nanoparticles while reducing the likelihood of coating dissolution and enhancing mechanical strength and wear resistance. SiO_2/ZrO_2 and SiO_2/TiO_2 composites are promising hybrid coating materials, which will be discussed in greater detail in subsequent sections [75, 76].

ZrO_2:

Several scientific articles indicate zirconium dioxide (ZrO_2) has excellent acid and alkali resistance and demonstrates stability across a pH range of 1 to 13 [77], and it is able to withstand temperatures exceeding 1200°C [78]. Additionally, ZrO_2 has been shown to significantly enhance the mechanical strength and wear resistance of coatings [79]. Furthermore, uniform ZrO_2 thin films can be fabricated using the sol-gel method combined with spin coating technique [80]. Therefore, these studies show that the sol-gel method is an effective method for preparing ZrO_2 coatings, and ZrO_2 has excellent chemical and thermal resistance, making it suitable for use in various corrosive environments and high temperature applications.

From the research by Szczurek [81] and Atik [82], several conclusions can be drawn. First, ZrO_2 is an effective corrosion-resistant coating material that can be fabricated using the sol-gel method, providing enhanced corrosion resistance and mechanical strength. However, its large particle size results in a less dense coating, and excessive thickness can lead to cracking. These characteristics are complementary to those of SiO_2, explaining why pure ZrO_2 sol-gel films are rarely reported in the literature. Instead, ZrO_2 is often combined with other materials to optimize coating performance. Therefore, the following section will introduce SiO_2/ZrO_2 composite sol-gel coatings for enhanced sealing and corrosion protection.

TiO_2:

Titanium dioxide (TiO_2) is another material suitable for use as a sealing coating in sol-gel processes, which exhibits excellent thermal stability as shown in numerous studies. When exposed to high temperatures, titanium forms a stable oxide layer composed of TiO_2. This oxide layer serves as a protective barrier, preventing further oxidation and thermal degradation. At 800°C, TiO_2 undergoes a phase transformation from anatase to rutile

[83]. Additionally, some research has discussed the crystal structure, thermodynamic properties, and phase transitions of TiO_2, proving that rutile is the most thermodynamically stable phase, with a melting point as high as 1570°C (1843 K) [84]. TiO_2 nanoparticles can also further enhance the thermal stability of coatings. For instance, Fan et al. demonstrated the impact of TiO_2 nanoparticles on silica aerogel composites, revealing that their addition significantly improved the collapse resistance of aerogels under high temperatures over 1000°C [85].

The study from Sippel [86] indicates that TiO_2 can endure high temperatures and exhibits exceptional thermal stability. Beyond its thermal properties, TiO_2 is an environmentally friendly material with low cost, high chemical stability, and low toxicity. Also, from the research by Boshkova [87] and Zhang [88] collectively indicate that TiO_2 itself is often employed in producing anti-corrosion coatings, or its nanoparticles are incorporated into other coating materials to enhance mechanical properties and corrosion resistance.

However, current literature on the use of TiO_2 as a standalone sol-gel coating material remains limited. Similar to previous studies on ZrO_2, this scarcity of research may be attributed to the fact that when TiO_2 is combined with other materials, such as SiO_2, the resulting thin films exhibit significantly enhanced properties by integrating the advantages of both components. Therefore, the following sections will provide a detailed discussion on the characteristics of SiO_2/TiO_2 as a sol-gel coating material.

SiO_2/ZrO_2:

Previous sections of SiO_2 and ZrO_2 coatings have demonstrated that while sol-gel coatings based on silane exhibit strong adhesion to substrates and form dense protective layers, they are susceptible to dissolution under acidic conditions and exhibit limited hardness and wear resistance. To enhance the corrosion resistance of these coatings, particularly in cases of mechanical damage, the incorporation of SiO_2 with other compounds into the sol-gel matrix is necessary. ZrO_2, known for its hardness, presents a viable option. According to Abdollahi's research [89], SiO_2/ZrO_2 composite coatings exhibit corrosion resistance improvements of approximately three-fold and sevenfold compared to SiO_2 coatings and bare substrates, respectively . Additionally, results from Gkasiorek et al. [90] reveal that the SiO_2/ZrO_2 coating possesses higher Vickers hardness is as high as uncoated 316L steel, but the polarization resistance is nearly 84 times higher.

Based on the studies above, to enhance the corrosion resistance, mechanical strength, and adhesion of coatings or substrates, sol-gel-derived SiO_2/ZrO_2 coatings represent an excellent material choice, because it integrates the advantages of both materials. Moreover, the number of studies investigating SiO_2/ZrO_2 coatings far exceeds those focusing on either SiO_2 or ZrO_2 individually, suggesting their broader applicability. Given these advantages, SiO_2/ZrO_2 coatings are well-suited for sealing the pores of Hastelloy C276 coatings, making them a promising material choice for corrosion-resistant applications.

SiO_2/TiO_2:

The previous section introduced SiO_2/ZrO_2 as an excellent sol-gel coating material, similarly, SiO_2/TiO_2 is another promising alternative. This composite material is not only suitable for photocatalytic and self-cleaning applications but also exhibits significant corrosion resistance for steel substrates. The advantages of SiO_2/TiO_2 coatings include corrosion resistance, high thermal stability, excellent mechanical strength (a characteristic of SiO_2), chemical stability, and a higher thermal expansion coefficient (a characteristic of TiO_2). From the earlier discussion, it is evident that SiO_2 possesses strong adhesion properties, allowing its coatings to firmly attach to the substrate. The addition of TiO_2 further enhances the adhesion of sol-gel coatings [91].

From some studies reviewed [92, 93], SiO_2/TiO_2 coatings are increasingly favored over pure SiO_2 or TiO_2 as corrosion-resistant coatings. The results demonstrate their effectiveness in enhancing corrosion resistance and mechanical strength. Additionally, the findings emphasize the importance of sol composition, heat treatment

duration, and environmental conditions in determining the final coating structure. Although certain aspects of SiO_2/TiO_2 coatings are less extensively studied compared to SiO_2/ZrO_2, SiO_2/TiO_2 remains a promising material for Hastelloy C276 coatings.

Comparison of the Material Options:

The previous paragraphs have provided detailed discussions on the use of Al_2O_3, SiO_2, ZrO_2, TiO_2, SiO_2/ZrO_2, and SiO_2/TiO_2 as sealing coatings, along with their respective performance outcomes. However, due to variations in substrate materials, post-coating heat treatments, and atmospheric exposure times, it is challenging to establish a unified benchmark for fair comparison among these coatings. The susceptibility of different substrates to corrosion further complicates direct comparisons. Nevertheless, as evidenced by the aforementioned studies, sol–gel-derived coatings can significantly enhance the corrosion resistance of the underlying substrates and, in most cases, also contribute to improved mechanical strength. Each coating material, however, exhibits certain limitations. For instance, while Al_2O_3 is well-regarded for its excellent corrosion and wear resistance, making it a promising candidate for sealing layers, it requires specialized precursors that are highly prone to hydrolysis, rendering the sol preparation process relatively complex. Additionally, Al_2O_3 sol–gel coatings tend to exhibit higher shrinkage during drying and calcination, which increases the risk of cracking. As a result, Al_2O_3 is often not prioritized as a primary sealing material when alternative options are available. SiO_2, on the other hand, is favored for its ultrafine particle size, which enables effective infiltration and pore filling, as well as its strong adhesion to various substrates and satisfactory corrosion resistance. However, SiO_2 coatings may degrade in certain acidic environments, particularly those containing fluorides.

To overcome this drawback, SiO_2 is frequently combined with other oxides, such as ZrO_2 and TiO_2, to form composite coatings with enhanced hardness and wear resistance. ZrO_2 and TiO_2 both exhibit corrosion resistance and advantages like excellent mechanical strength and high thermal expansion coefficient. Nevertheless, their relatively large particle sizes often result in less dense coatings, making them less suitable as standalone sealing materials. Their properties, however, can be combined with the infiltration and adhesion capabilities of SiO_2, and thus their integration in SiO_2/ZrO_2 and SiO_2/TiO_2 composite sol–gel coatings offers synergistic advantages.

These composite systems effectively combine the strong penetration and adhesion of SiO_2 with the mechanical robustness or thermal expansion resistance of ZrO_2 and TiO_2, positioning them as the most promising candidates among the sol–gel coatings discussed for use as sealing layers on Hastelloy C276 substrates. Compared to both, literature on the use of SiO_2/ZrO_2 as sol-gel materials is significantly more abundant than that on SiO_2/TiO_2. Therefore, given the available resources and existing knowledge base, this study ultimately selected SiO_2/ZrO_2 as the sol-gel material system. It is noteworthy that there have been no prior studies specifically employing SiO_2/ZrO_2 composite sol–gel coatings for the sealing of thermal spray coatings. Therefore, the ultimate performance of the system must still be validated through experimental investigation.

3 RESEARCH GOALS

Building upon Section 1 and 2, this chapter focuses on the core objective of the study: Developing strategies to extend the service life of HVAF-sprayed Hastelloy C276 coatings in H_2S-containing environments.

Leveraging the selected fabrication method, namely the sol-gel process, and the chosen material system, SiO_2/ZrO_2, the chapter further refines and articulates the central research question.

Main Goal:

The primary aim of this study is to experimentally determine the extent to which a sol-gel SiO_2/ZrO_2 sealing layer can enhance the durability of HVAF sprayed Hastelloy C276 coatings under H_2S-containing environments.

Design of Experiments:

The ultimate objective is to evaluate whether applying a sol-gel SiO_2/ZrO_2 sealing layer can improve the durability of HVAF-sprayed Hastelloy C276, thereby extending its service lifespan. Durability was assessed from three perspectives:

1. Mechanical properties, including microhardness and wear resistance.

2. Corrosion resistance

3. Hydrogen induced cracking (HIC) Resistance

To this end, an uncoated HVAF sprayed Hastelloy C276 specimen (without any sol-gel SiO_2/ZrO_2 sealing layer) was used as the control. Two experimental configurations were prepared:

- **Two-layer sol-gel sample**: one SiO_2 layer followed by one SiO_2/ZrO_2 layer.

- **Five-layer sol-gel sample**: one SiO_2 layer followed by four SiO_2/ZrO_2 layers.

The first layer was exclusively SiO_2 to ensure superior adhesion to the substrate, while subsequent SiO_2/ZrO_2 layers were applied to take advantage of the higher hardness imparted by ZrO_2. Comparative testing among the control, two-layer, and five-layer configurations enabled evaluation of the influence of coating thickness on durability, as well as determination of whether four SiO_2/ZrO_2 layers outperform a single SiO_2/ZrO_2 layer in enhancing performance.

4 MATERIALS AND METHODS

This chapter outlines the preparatory steps for the testing and analysis of substrates and coatings, and it is divided into two main parts. The first part details the sample preparation and the materials employed in this study. The second part describes the testing methodologies, experimental setups, parameter configurations, and procedural workflows used for sample evaluation.

4.1 MATERIALS AND SAMPLE PREPARATION

This section provides a detailed description of the sample preparation procedures, including the materials of the substrates, HVAF thermal spray coatings, and sol-gel sealing layers used in this study, and the compositions of each material are specified, along with the fabrication processes for both the HVAF sprayed coatings and the sol-gel sealing coatings.

4.1.1 Materials

In this study, carbon steel S235JR was selected as the substrate material, while the HVAF sprayed coating was composed of Hastelloy C276. For the sol-gel sealing layer, a composite of ZrO_2 and SiO_2 was employed. The following paragraphs provide a detailed discussion of the information of these three materials.

Substrate Material - S235JR Carbon Steel

S235JR carbon steel is a widely used low-carbon structural steel. The designation "S" represents structural steel, while "235" indicates a minimum yield strength of 235 MPa. The "JR" suffix denotes that the steel exhibits a minimum absorbed energy of 27 J during a V-notch impact test conducted at 20°C. Due to its excellent plasticity, toughness, and weldability, S235JR steel is commonly utilized in the manufacturing of mechanical components such as shafts, brackets, and machine parts. Additionally, it is frequently used for internal components inside pressure vessels, as well as in marine industries, including ship hull construction. Table 1 displays the chemical composition of S235JR carbon steel.

C	Mn	Cu	Al	Mo	Si	P	S	Fe
0.16	0.4	0.03	0.04	0.03	0.016	0.05	0.017	Rest

Table 1: Chemical composition of S235JR carbon steel, wt.%.

The primary chemical composition of S235JR steel, aside from its main constituent iron (Fe), includes carbon (C), manganese (Mn), copper (Cu), aluminum (Al), molybdenum (Mo), silicon (Si), phosphorus (P), and sulfur (S). The careful control of these elemental compositions ensures favorable weldability and mechanical properties. The yield strength and tensile strength of S235JR steel vary with thickness. For steel plates with a thickness of up to 16 mm, the minimum yield strength is 235 MPa, while the tensile strength ranges from 360 to 510 MPa, with an elongation after fracture of approximately 26%. As thickness increases, slight reductions in yield strength and elongation after fracture may be observed. Within the temperature range of 20 to 300°C, the linear thermal expansion coefficient is approximately 12 µm/m·K, while thermal conductivity ranges between 40 and 45 W/m·K. The specific heat capacity is approximately 460 to 480 J/kg·K within the range of 50 to 100°C. These physical properties demonstrate the thermal stability of S235JR steel, ensuring consistent performance across various temperature and environmental conditions [94–96].

However, like all carbon steels, S235JR is highly susceptible to corrosion in industrial environments, which can lead to failure and structural degradation, as well as costly maintenance and productivity losses. Due to its relatively high sulfur content (> 0.001 wt%), S235JR is particularly vulnerable to hydrogen induced cracking. This susceptibility is one of the key reasons why S235JR was selected as the substrate material in this study,

as it facilitates the observation and analysis of HIC related degradation. To enhance the corrosion resistance of S235JR in H_2S-containing environments, particularly for demanding applications such as oil industry pipelines, this study employs a dual protective coating system. The system comprises a HVAF thermal sprayed coating and a sol-gel derived sealing layer, which are anticipated to work synergistically to provide superior protection against corrosive environments.

HVAF Coating Material - Hastelloy C276 (NiCrMoW)

One of the primary advantages of thermal spray coatings is the wide range of materials that can be utilized. Metal and metal-ceramic coatings are predominantly employed due to their superior durability, corrosion resistance, and mechanical performance. Thermal spray coatings can be further categorized into sacrificial and non-sacrificial coatings [97–99]. In the petroleum industry, non-sacrificial coatings are predominantly used as corrosion protection materials due to their ability to withstand high-temperature and highly acidic environments. Among these materials, nickel-based alloys are the most commonly selected due to their exceptional corrosion resistance, thermal stability, and mechanical strength. In addition to nickel, elements such as chromium (Cr), nitrogen (N), molybdenum (Mo), and tungsten (W) are frequently incorporated into these alloys to enhance their corrosion resistance. For example, Cr contributes to the formation of a stable passive oxide layer, providing additional resistance in corrosive environments, while Mo is commonly added to improve resistance to pitting and crevice corrosion [100].

Winters' study presents a comparison of commonly used non-sacrificial coating materials, including Hastelloy C276, Inconel 625, 316L stainless steel, 22Cr, and Metco 505/Metco 16C, which are displayed in Figure 10. Among these, Hastelloy C276 has been selected for this study due to its superior resistance to H_2S environments and its low probability of coating defects compared to other materials [6].

Material	Hastelloy C276	Inconel 625	316L	22Cr	Metco 505/ Metco 16C
Corrosion Resistivity (H_2S)	++	+	+/-	+	+
Erosion Resistance	+	+	+/-	+	+
Compatibility with HVAF	Yes	Yes	Yes	Yes	Yes
Cost-effectiveness	+/-	+/-	++	+/-	+/-
Effect on HSE	Minimal	Minimal	Minimal	Minimal	Minimal
Chance of Defects	++	+	+/-	+	+

Figure 10: Material options thermal spray in the sour environment against HIC [6].

Hastelloy C276 is a nickel based superalloy renowned for its outstanding corrosion resistance, making it particularly suitable for harsh chemical environments. Its chemical composition primarily consists of nickel, chromium, and molybdenum, which collectively contribute to its excellent resistance to a wide range of corrosive media while maintaining stable mechanical properties. The detailed chemical composition of Hastelloy C276 is presented in Table 2. Crum et al. reported that at room temperature, Hastelloy C276 exhibits a tensile strength of approximately 690 MPa, a yield strength of around 283 MPa, and an elongation at break of nearly 50%. Furthermore, this alloy retains its favorable mechanical properties at elevated temperatures, making it suitable for high-temperature applications. Shi's research also confirmed that Hastelloy C276 demonstrates excellent corrosion resistance under high-temperature and high-pressure conditions [101, 102].

Sol-gel Sealant Material - SiO$_2$ and ZrO$_2$

Ni	Mo	Cr	Fe	W	Mn	Co	V	S	C
57	15-17	14.5-16.5	4-7	3-4.5	1	2.5	3.5	0.03	0.03

Table 2: Chemical composition of Hastelloy C276 (NiCrMoW), wt.% [6].

The sol formulations for SiO_2 and ZrO_2 used in this study were adapted from the work of Gąsiorek et al. [90]. For the SiO_2 sol, the main oxide precursors were tetraethoxysilane (TEOS, Aldrich, 98%) and dimethyldiethoxysilane (dMdEOS, Sigma-Aldrich, >97%), with ethanol (EtOH, Honeywell, >99%) as the solvent and hydrochloric acid (HCl, Honeywell & Fluka) used to provide an acidic environment. For the ZrO_2 sol, butanol (BuOH, Merek, >97%) was used as the solvent, while zirconium butanolate (ZrOBu, Sigma-Aldrich, 80 wt% in 1-butanol) served as the precursor. Acetylacetone (AcAc, Sigma-Aldrich, >99%) was added as a chelating agent to stabilize the zirconia sol by slowing the hydrolysis and condensation reactions. Acetic acid (CH_3COOH, Sigma-Aldrich, >99.7%) was then used to adjust the pH and maintain an acidic environment. All chemicals were used as received, without any further purification.

4.1.2 Sample Preparation

This section describes the sample preparation procedure. Carbon steel S235JR with a thickness of 8 mm was used as the substrate material. The steel plates were cut using a Discotom-6 precision cutting machine, as shown in Figure 18a, into two different sizes, 100 mm × 20 mm and 25 mm × 25 mm. The larger specimens (100 mm × 20 mm) were designated for HIC immersion tests, while the smaller specimens (25 mm × 25 mm) were prepared for all other characterization tests.

After cutting, the samples were subjected to grinding. Although a rougher surface can enhance the adhesion of HVAF coatings to the substrate, surface rust and oxide layers formed during storage need to be removed. Therefore, wet grinding was performed using silicon carbide sanding papers, starting from 80 grit and progressing up to 4000 grit.

Subsequently, the samples were sent to RWTH Aachen University IOT, for HVAF coating with Hastelloy C276. Prior to the coating process, grit blasting was carried out to increase surface roughness. The blasting material used was Corundum F-20, a high-purity white fused alumina (Al_2O_3) with a particle size range of 850 to 1200 μm, which is typical for such surface treatments. To ensure uniformity during grit blasting, the blasting gun was positioned at an angle of approximately 60° to the horizontal surface and maintained at a distance of 5–10 cm from the substrate.

Following grit blasting, the substrate surface was rinsed with isopropanol prior to coating. The Hastelloy C276 coating was subsequently applied using a Kermetico AK07 HVAF system. The spray gun was mounted on an ABB IRB4600 robotic arm to ensure coating consistency and reproducibility across all samples.

The coated samples were divided into three batches, totaling 12 specimens: four larger samples (100 mm × 20 mm) and eight smaller samples (25 mm × 25 mm). Each batch was coated separately. The first two batches consisted of the larger samples, with two specimens coated per batch, resulting in four coated large samples. The third batch involved coating all eight small samples simultaneously. The Table 3 summarizes the HVAF spraying parameters, which were optimized through iterative trials. The ABB IRB4600 robotic arm was programmed to translate horizontally during spraying to achieve uniform coating, with additional vertical movements performed outside the coating zone.

A target coating thickness of 250 μm was specified for this experiment. Based on the selected parameters, which are shown in Table 3, the coating deposition per pass was estimated to be 13-15 μm. Therefore, 20 passes were required to achieve the desired thickness. After every 10 passes, compressed air was used to cool

(a) Corundum F-20 powder for grit blasting.
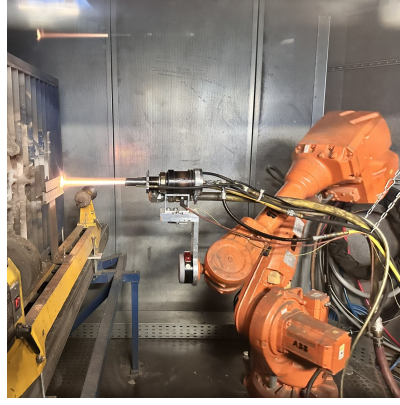
(b) The Kermetico AK07 HVAF machine and ABB IRB4600 robotic arm.
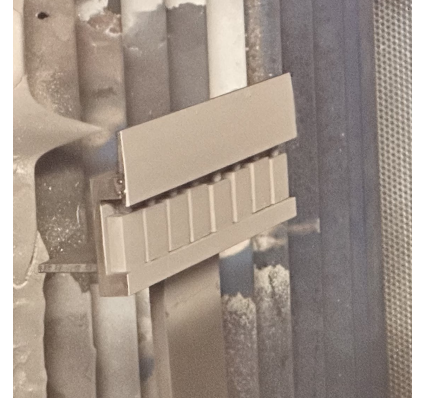
(c) The sample holder of HVAF thermal spray.

Figure 11: Facilities of HVAF thermal spray.

the samples, rapidly reducing the substrate surface temperature. Upon completion of the spraying process, the coating thickness was measured using a micrometer caliper. Despite setting the target thickness at 250 μm, slight variations were observed during deposition, with the final coating thickness ranging from approximately 260 to 280 μm.

Process Parameters	Value
Feedstock Materials	NiCrMoW (Hastelloy C276)
Powder size in μm	15-45
Air pressure in MPa	0.66
Propane pressure in MPa	0.55
Carrier gas N2 in SLPM	37.2
Nozzle length in mm	180
Powder feed rate in min^{-1}	3.5
Gun velocity in mm/s	1000
Spray distance in mm	250
Meander width in mm	5
Coating deposition per pass in μm	13-15
Overlays	20

Table 3: Process parameters setting for HVAF coating.

Following the HVAF spraying of the Hastelloy C276 coating, the next step involved the application of a sol-gel-derived SiO_2/ZrO_2 sealing layer. Prior to sol-gel deposition, the as-sprayed (unpolished) surface of the coating–substrate system was characterized for surface roughness. Since each dip-coated sol-gel layer is approximately 0.5-2 μm thick, an excessively rough HVAF surface could impair adhesion and result in poor coverage. Surface roughness constants (Ra, Rq, Rz) of the as-sprayed coating were found to be significantly larger than the sol-gel layer thickness, highlighting the need for surface smoothing. To address this, the HVAF sprayed surface was wet ground and polished. To minimize potential damage to or excessive thinning of the coating, the coarse SiC papers, 80 and 180 grit, were omitted, and grinding began with 320 and progress to 4000 grit, followed by polishing with 3 μm and 1 μm diamond disks.

The sol-gel formulations for SiO_2 and ZrO_2 were adapted from Gąsiorek et al. [90]. The SiO_2 sol was prepared using TEOS : dMdEOS : EtOH : HCl = 1 : 1 : 4 : 0.02 (volume ratio), and the ZrO_2 sol using ZrOBu : BuOH : AcAc : CH_3COOH = 1 : 4 : 0.5 : 0.5 (volume ratio). The preparation order was found to be crucial. For the SiO_2 sol, EtOH and HCl were first mixed to form a homogeneous acidic medium, followed by dMdEOS, and finally TEOS. This order prevents premature hydrolysis and condensation of TEOS, improving sol uniformity. In the case of the ZrO_2 sol, ZrOBu was first added to BuOH. As ZrOBu is highly sensitive to water, direct contact must be avoided to prevent rapid hydrolysis and white precipitate formation. Next, AcAc was introduced to chelate Zr^{4+} and suppress unwanted reactions. Finally, CH_3COOH was added to adjust the pH value and stabilize the sol. The sol of SiO_2, ZrO_2, and SiO_2/ZrO_2 are displayed in Figure 12. It was observed that the SiO_2 sol appeared transparent, while the ZrO_2 sol exhibited a pale yellow color. Upon mixing the two in equal volume, the resulting SiO_2/ZrO_2 sol showed an even lighter shade of yellow.

(a) SiO_2 sol   (b) ZrO_2 sol   (c) SiO_2/ZrO_2 sol
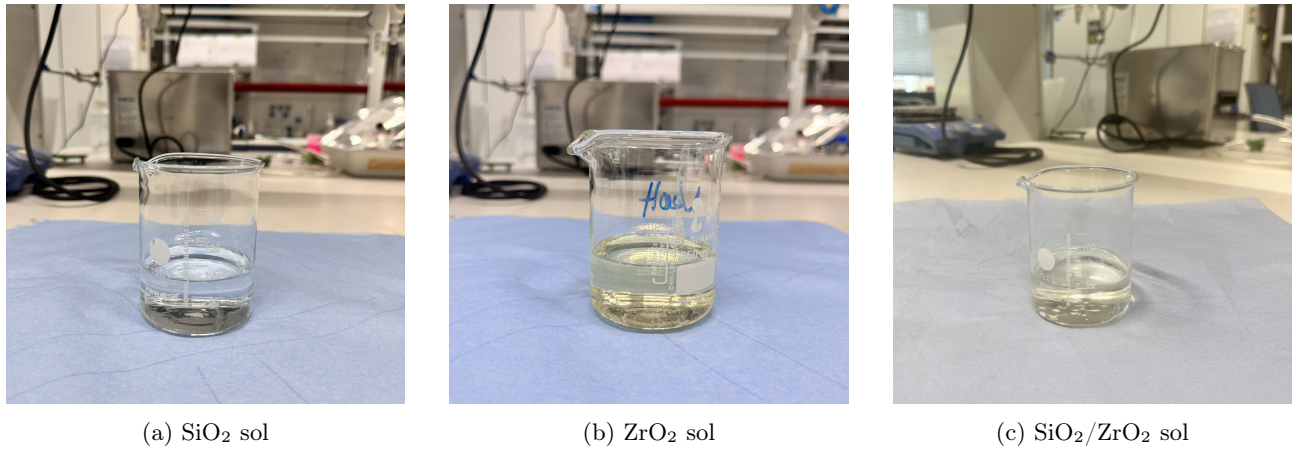
Figure 12: The images of SiO_2, ZrO_2, and SiO_2/ZrO_2 sol

Two types of sol-gel sealing layer configurations were prepared, one consisting of two layers and the other of five layers, as shown in Figure 13b and 13c. These configurations were compared with the unsealed HVAF sprayed Hastelloy C276 substrate system, and its schematic is illustrated in Figure 13a. In both cases, the first layer consists of pure SiO_2. To enhance the adhesion between the sol–gel sealing and the HVAF sprayed Hastelloy C276, the subsequent layers are composed of SiO_2/ZrO_2 sol, which serves to increase the overall hardness of the sealing layer. Moreover, the process of filtration needs to be performed after applying each layer. The samples were prepared in two sizes, 100 mm × 20 mm and 25 mm × 25 mm, and both of them are 8 mm thick. Solution volumes were adjusted to ensure adequate coverage, accounting for losses during filtration. A total volume of 300 mL of each sol was prepared for the final decision. After applying the first SiO_2 layer, the remaining sol was mixed with the same volume of ZrO_2 for the subsequent layers.

The dip coating machine and the process are illustrated in Figure 14. According to the protocol proposed by Gąsiorek et al. [90], the dip coating withdrawal speed was initially intended to be set at 34.12 mm/min. However, the dip coating equipment used in this study only allowed withdrawal speeds of 30 mm/min and 40 mm/min. To avoid wasting the limited number of actual experimental samples, preliminary tests of applying the sol-gel layers were first conducted using Hastelloy C22 plate, an alloy with a chemical composition closely resembling that of the HVAF sprayed Hastelloy C276 coating. The elemental composition of Hastelloy C22 is listed in Table 4.

Hastelloy C22 was selected as a surrogate substrate due to its compositional similarity to Hastelloy C276, and its surface roughness could be matched through identical wet grinding and polishing procedures. Although the intrinsic porosity between the two alloys may differ, this approach was considered the most practical under current resource constraints.
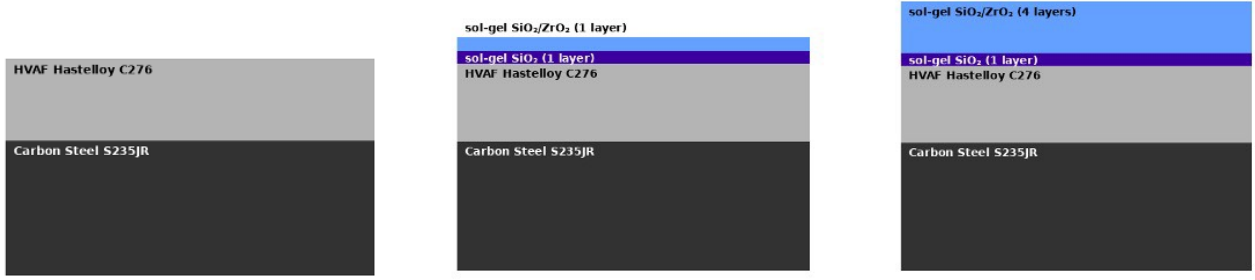
(a) The schematic of HVAF Hastelloy C276-substrate system without sol-gel sealing layer

(b) The schematic of 2 layers sol-gel-HVAF Hastelloy C276-substrate system

(c) The schematic of 5 layers sol-gel-HVAF Hastelloy C276-substrate system

Figure 13: The images of SiO_2, ZrO_2, and SiO_2/ZrO_2 sol
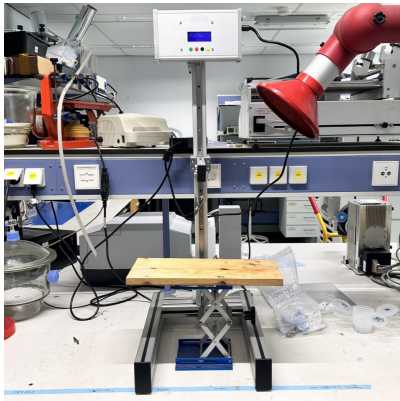
(a) The machine image of Dip Coater RDC 15
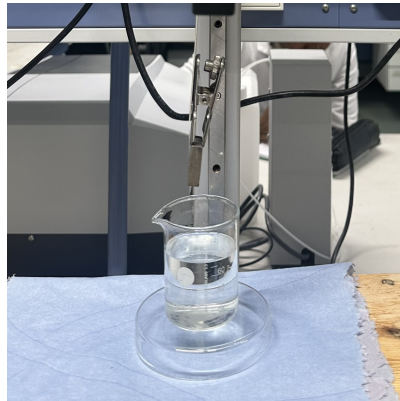
(b) The image of coating a 2.5 cm × 2.5 cm sample
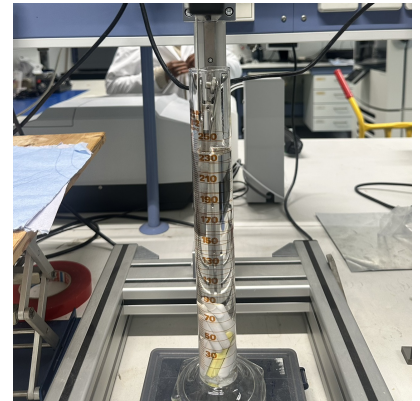
(c) The image of coating a 2 cm × 10 cm sample

Figure 14: The images of dip coating machine and its process

Ni	Mo	Cr	Fe	W	Mn	Co	Si	C
56	13	22	3	3	0.5	2.5	0.08	0.01

Table 4: Chemical composition of Hastelloy C22 (NiCrMoW), wt.% [12].

Experimental observations revealed that setting the withdrawal speed to 30 mm/min resulted in excessive localized solvent evaporation, leading to the visible formation of white particulate deposits on the substrate surface, as shown in Figure 15. Subsequent EDS analysis (Figure 16) confirmed that these particles were predominantly ZrO_2, indicating severe non-uniformity in the sol-gel sealing layer. Such defects could significantly affect the reliability of subsequent electrochemical and mechanical tests.

To mitigate this non-uniformity, both the immersion and withdrawal speeds were increased to 40 mm/min while maintaining a dipping time of 60 seconds. This adjustment effectively eliminated the visible particle formation on the surface. Hence, a dipping and withdrawal rate of 40 mm/min and a residence time of 60 seconds were selected as the final dip coating parameters for all subsequent experiments.

After each coating layer, samples were air dried at room temperature and then heated at 80 °C for 1 h to remove residual volatiles and reduce the risk of cracking, thereby improving interfacial bonding and densification. It was essential to allow the samples to return to room temperature before applying the next layer to avoid interlayer adhesion defects. Upon completion of all layers, a final thermal treatment was conducted at 200 °C for 2 h.

Figure 15: The white particles which can be seen on Hastelloy C22.

Formula	mass%	Atom%	Sigma	K ratio	Line
C	10.17	22.21	0.04	0.0014690	K
O	30.07	49.31	0.13	0.0418516	K
Si	12.88	12.03	0.07	0.0428105	K
Cl	1.56	1.16	0.03	0.0049307	K
Cr	7.26	3.66	0.07	0.0284781	K
Mn	0.71	0.34	0.05	0.0028115	K
Ni	3.46	1.55	0.07	0.0142858	K
Zr	33.87	9.74	0.17	0.1095548	L
Total	100.00	100.00			
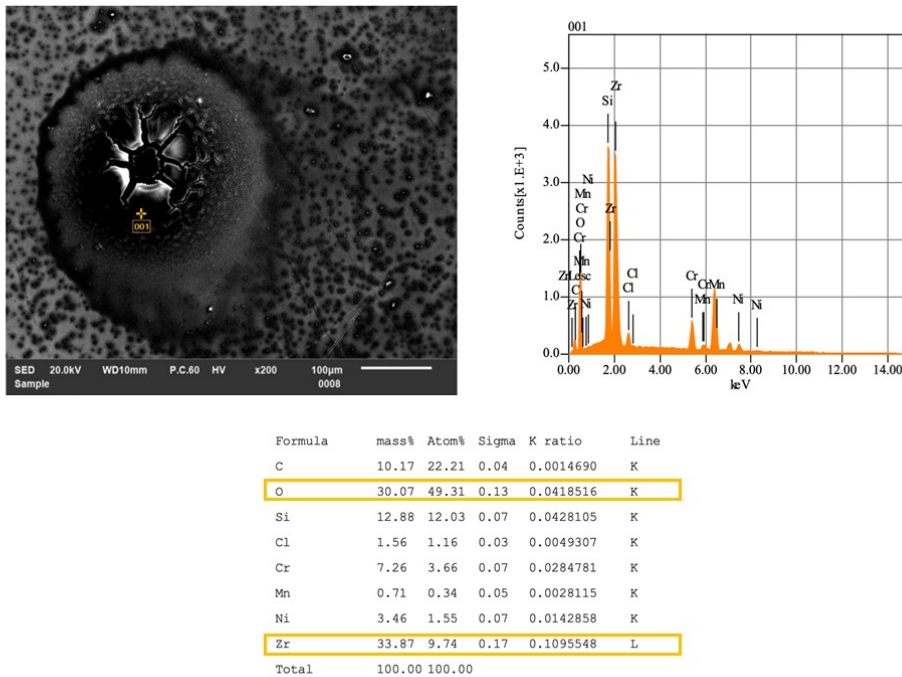
Figure 16: Spectrum mode EDS analysis in "point" configuration of the white particles on the surface.

4.2 TESTING METHODS

This section provides a detailed description of the sample characterization procedures. The overall testing process was divided into three parts, covering the carbon steel S235JR substrate, the HVAF sprayed Hastelloy C276 coating, and the sol-gel derived ZrO_2 sealing layer. The properties which need to be tested in this research

are summarized in Table 5.

Measurement Items	Parts to be Measured	Instrument Used
Surface morphology (top & cross-section)	Substrate (Carbon Steel S235JR)	Optical Microscope (VHX-7000N)
	HVAF Coating (Hastelloy C276)	
	Sol-gel Coating (SiO$_2$/ZrO$_2$)	
Microstructural analysis	Substrate (Carbon Steel S235JR)	SEM (JEOL JSM-IT100)
	HVAF Coating (Hastelloy C276)	
	Sol-gel Coating (SiO$_2$/ZrO$_2$)	
Elemental composition	Substrate (Carbon Steel S235JR)	SEM-EDS
	HVAF Coating (Hastelloy C276)	
	Sol-gel Coating (SiO$_2$/ZrO$_2$)	
Surface roughness (Ra, Rq, Rz)	HVAF Coating (Hastelloy C276)	VHX-7000N with surface analysis module
	Sol-gel Coating (SiO$_2$/ZrO$_2$)	
Porosity	HVAF Coating (Hastelloy C276)	SEM images + ImageJ software
Microhardness (top surface)	HVAF Coating (Hastelloy C276)	Microhardness Tester (Struers DuraScan G5)
	Sol-gel Coating (SiO$_2$/ZrO$_2$)	
Wear resistance	HVAF Coating (Hastelloy C276)	Ball-on-disk tribometer TRB3
	Sol-gel Coating (SiO$_2$/ZrO$_2$)	
Corrosion resistance	HVAF Coating (Hastelloy C276)	OCP, PDP, and EIS
	Sol-gel Coating (SiO$_2$/ZrO$_2$)	
HIC resistance	HVAF Coating (Hastelloy C276)	Immersion test in H$_2$S environment + OM measurement (CSR, CTR, and CLR)
	Sol-gel Coating (SiO$_2$/ZrO$_2$)	

Table 5: List of properties to be characterized

The first phase of testing focused on the carbon steel S235JR substrate, emphasizing surface characterizations of both the top surface and cross section. Scanning electron microscopy (SEM) and optical microscopy (OM) were employed for morphological and phases analysis. In addition, energy dispersive X-ray spectroscopy (EDS) was used to analyze the elemental composition of the substrate surface to confirm its chemical structure.

The second phase involved property characterization of the Hastelloy C276 coating after HVAF thermal spraying. Similar to the substrate analysis, SEM, OM, and EDS were utilized to investigate the surface morphology and elemental composition of the coating on both the top surface and cross section. In addition to these analyses, the coating was evaluated for surface roughness, porosity, wear resistance and surface hardness. Electrochemical properties were also assessed using open circuit potential (OCP) , electrochemical impedance spectroscopy (EIS), and potentiodynamic polarization (PDP) tests. Finally, the coated samples were exposed to a hydrogen sulfide-rich environment to evaluate their resistance to hydrogen induced cracking.

The third phase of testing was conducted after applying the sol-gel derived SiO$_2$ and ZrO$_2$ sealing layer. This phase included all the characterization methods used for the Hastelloy C276 coating, allowing for direct comparison between sealed and unsealed coatings to assess the additive effect of the sealing layer. Additionally, coatings with different sealing layer thicknesses were compared to evaluate the influence of thickness on coating properties.

It is worth noting that porosity measurements were initially planned for the SiO$_2$/ZrO$_2$ sol-gel-coated samples to evaluate the extent of pore coverage. However, this measurement was ultimately not performed due to the inherent transparency of the SiO$_2$/ZrO$_2$ sol-gel sealing, which makes it difficult to visually distinguish pore-filling behavior in SEM images. This means reliable pore detection using ImageJ was not feasible, and any analysis derived from such images would lack accuracy. Therefore, the porosity evaluation of the coated samples may be a potential topic to research in the future.

The subsequent subsections will provide a comprehensive description of the experimental setups, parameter

settings, and experimental procedures for each characterization method.

4.2.1 Surface Morphology and Microstructure

This section focuses on the evaluation of the metallurgical properties of the samples, including key surface characterizations. Typical features analyzed include inclusions within the substrate, oxidation and porosity formed in the coating, as well as the surface roughness of the samples both before and after coating. The characterization was performed using optical microscopy (OM) and scanning electron microscopy (SEM) as the primary techniques. In addition, energy dispersive spectroscopy (EDS) played a critical role in determining the elemental composition and assessing the extent of oxidation.

Optical Microscopy (OM)

The optical microscope used in this study was the Keyence VHX-7000N Digital Microscope, shown in Figure 17b, which was employed to examine both the substrate and coated samples. For the substrate, characterization included both the top surface and cross section. Prior to analysis, the substrate samples were sectioned, mounted in conductive resin, and subjected to wet grinding using silicon carbide sanding papers, progressing from 80 grit to 4000 grit. The samples were then polished using 3 μm and 1 μm diamond disks and etched in Nital solution for 10 seconds to reveal the microstructure. The primary objectives of the substrate analysis were to identify the number of phases present, evaluate the effect of the rolling direction on the grain structure, and analyze pre-existing cracks and defects, including inclusions. Magnifications of 200×, 500×, and 700× were employed for these observations, and the results were further analyzed in conjunction with SEM findings.

For the HVAF coating, both the as-sprayed surface and the surface subjected to wet grinding and polishing were evaluated. This also includes the top surface and the cross section of the coating. The polishing process involved sequential grinding with silicon carbide papers ranging from 80 grit to 4000 grit, followed by polishing with 3 μm and 1 μm diamond disks. Surface characterizations were performed at magnifications of 200×, 500×, and 700×, consistent with the substrate analysis. In addition to morphological evaluation, particular attention was given to surface roughness measurements.

Surface roughness was evaluated rather than linear profiles, as surface measurements provide a more accurate representation of the overall topography. Three key roughness parameters were analyzed, including the arithmetic average roughness (Ra), the maximum profile height (Rz), and the root mean square roughness (Rq). The goal of this analysis was to determine whether the polished or unpolished HVAF sprayed Hastelloy C276 surface provides a more suitable base for subsequent sol-gel sealing layer application. Surface roughness was measured using the built-in surface analysis function of the VHX-7000N Digital Microscope at 300× magnification, with each measured area covering approximately 950 μm × 750 μm. To ensure data reliability, five independent measurements were conducted for each sample, and the final surface roughness values were obtained by averaging all collected measurements.

For the sol-gel SiO_2/ZrO_2 sealing system, surface characterization was conducted in a manner consistent with the HVAF coating. Unlike the HVAF coating, roughness measurements for the sol-gel SiO_2/ZrO_2 layer were performed only on untreated surfaces. This is because the dip coated sol-gel sealing layer is extremely thin, typically the total thickness is in the range of 0.3–2 μm. Any mechanical surface preparation, such as wet grinding and polishing, could easily damage the sealing and lead to inaccurate results.

Scanning Electron Microscopy (SEM) and Energy Dispersive Spectroscopy (EDS)

The scanning electron microscope (SEM) used in this study was the JEOL JSM-IT100, as shown in Figure 17c, which was employed for the examination of both substrate and coating samples.

For the substrate, both the top surface and cross section were analyzed. Sample preparation followed the same

procedures as for OM, including sectioning, mounting in conductive resin, wet grinding, polishing, and etching. The primary aim of SEM analysis was to complement the OM results and confirm the identification of the phases present within the microstructure. Observations were performed at magnifications of $200\times$, $500\times$, and $700\times$, and the results were interpreted in conjunction with the iron phase diagram. Another focus of the SEM analysis was elemental characterization of both the substrate and inclusions, which was carried out using the SEM's built-in energy-dispersive spectroscopy (EDS) function. For EDS, the analysis type was set to "spectrum," with a scan time of 3 minutes to achieve high accuracy. Each test was conducted at $500\times$ magnification, analyzing the entire field of view and three specific points, one of which included an inclusion. This procedure was repeated three times, and the nine result data in total were then averaged to improve reliability.

For the HVAF coating, no additional sample preparation was required prior to analysis. SEM observations were conducted at magnifications of $200\times$, $500\times$, and $700\times$. In addition to surface morphology, porosity measurements were performed using ImageJ software on $500\times$ SEM images of both the coating's top surface and cross section. To exclude interfacial oxide scales, a final filter was applied to eliminate particles with a circularity below 0.10 μm^2 and over 1 μm^2. Besides porosity, elemental analysis of the coating surface was also conducted using EDS. In contrast to the substrate analysis, both "spectrum" mode to determine overall elemental composition and "map" mode to visualize the distribution of oxygen within the coating and assess the extent of oxidation were employed. The EDS map detection was performed at $500\times$ magnification with a scan time of 5 minutes and spectrum detection with 3 minutes. The results were analyzed alongside the spectrum data.

For the sol-gel-derived SiO_2/ZrO_2 coating, no additional embedding step was required prior to analysis, similar to the HVAF sprayed Hastelloy C276 coating. As noted in the previous OM section, the measurements for the sol-gel layer were only conducted on the untreated surface. This is because wet grinding and polishing could easily damage the thin sol-gel sealing layer and compromise the accuracy of the measurements. SEM and EDS analyses of the sol-gel sealing layer followed the same procedures as those used for the HVAF coating. However, unlike the HVAF coating, the sol-gel layer does not contain interfacial oxide scales, therefore, EDS analysis was performed only in "spectrum" mode rather than "map" mode.

(a) Manual cutting machine Discotom-6

(b) Digital microscope Keyence VHX-7000N

(c) Scanning electron microscope JEOL JSM-IT100

Figure 17: The machine images of cutting machine, optical microscope, and scanning electron microscope

4.2.2 Microhardness

Surface microhardness testing was conducted to determine the surface hardness of the HVAF Hastelloy C276 coating, and the sol-gel sealing layer. Given the thin nature of the sol-gel sealing layer, a microhardness tester was considered more suitable than conventional hardness testing methods. The microhardness measurements were performed using a Struers DuraScan G5, as shown in Figure 18. For the measurement of HVAF Hastelloy C276

coating and sol-gel sealing layer, the hardness was started from the top surface. Vickers hardness measurements were carried out using a diamond indenter (HV0.3) under a specified load. A $20\times$ objective lens was employed for indentation imaging, and the zoom level is set to level 1. Measurements were taken at intervals of 0.1 mm with 5 indentations. The testing area on the surface was then changed, and the process was repeated four times for each sample, totaling 20 data points. The average values were reported to ensure data reliability and accuracy.

(a) Microhardness testing machine Struers DuraScan G5

(b) Schematic of the microhardness test

(c) Image of microhardness tester indentation
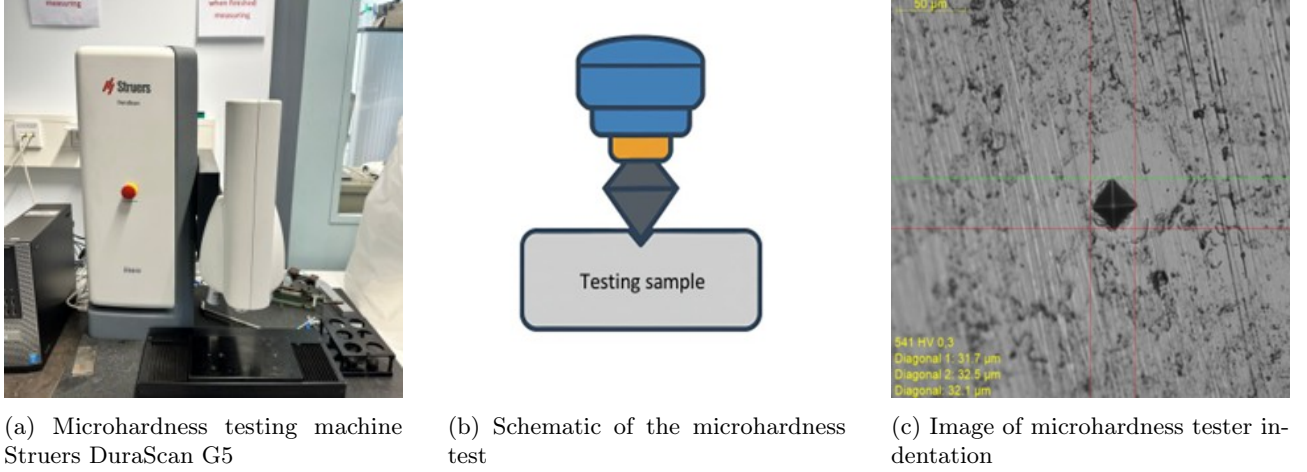
Figure 18: The machine and schematic images of microhardness measurement

4.2.3 Wear Resistance

In this study, wear resistance was evaluated using a ball-on-disk tribometer TRB3, as illustrated in Figure 19a. The aim was to determine whether the application of a SiO_2/ZrO_2 sol-gel sealing layer on HVAF sprayed Hastelloy C276 coatings improves wear resistance compared to samples coated with just Hastelloy C276. The test employed a standard ball-on-disk configuration, in which the disk refers to the specimen mounted on a rotating stage, and the ball is a 12 mm diameter alumina (Al_2O_3) sphere fixed to a loading arm above the sample.

Given the sample dimensions of 2.5×2.5 cm^2 with a thickness of 0.8 cm and the inherently high hardness of the Hastelloy C276 coating, the specimens possessed sufficient stiffness and mechanical stability to withstand standard contact loads. Accordingly, a normal load of 5 N was applied during testing to simulate frictional behavior under moderate contact pressure.

To ensure data accuracy, three different wear radii, 3.016 mm, 5.603 mm, and 8.038 mm, were tested on each sample, and the results were averaged. Theoretically, a smaller wear radius should result in a deeper wear track due to increased contact stress, and vice versa. This can also be seen in Figure 19b. During testing, care was taken to maintain the wear path within the central region of the specimen to minimize edge effects.

The sliding speed was set at 0.1 m/s with a total sliding distance limited to 100 m, ensuring that the wear depth did not exceed the coating thickness and that the wear scars remained measurable and stable. All tests were performed under ambient temperature in dry air without the use of lubricants, in order to assess the intrinsic friction and wear behavior of the surfaces.

After testing, samples were examined under an OM to observe the morphology of the wear tracks. The wear scar width and depth were measured using the advanced 3D measurement functions of the VHX-7000 digital microscope, which enabled precise quantification of the wear track geometry. The wear volume was calculated using the elliptical cross sectional area method multiplied by the track perimeter, as shown in Equation 8 and

9), where A is the cross sectional area of wear track (half area of ellipse), a is the half width of wear track cross section (major axes of ellipse), b is the depth of wear track cross section (minor axes of ellipse), V is the wear volume, and l is the wear track circumference. When calculating the track circumference, before multiplied by 2π, the original radius (3.016 mm, 5.603 mm, or 8.038 mm) was adjusted by adding half of the wear track width 0.6 mm (equivalent to the ball radius), as illustrated in Figure 19c.

(a) Wear Resistance testing machine TRB3 pin-on-disk tribometer.

(b) The wear track of different radius, 3.016, 5.603, and 8.038 mm.
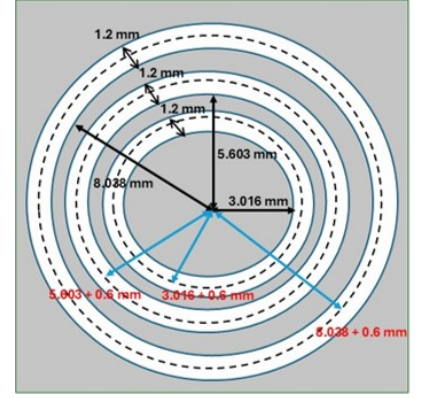
(c) Schematic of the radius for calculating the wear track circumference.

Figure 19: The machine and schematic images of wear resistance measurement.

$$A = \frac{1}{2}\pi ab \qquad (8)$$

$$V = A \cdot l \qquad (9)$$

Although approximating the wear track cross section as an ellipse introduces some error, it is significantly more accurate than assuming a circular shape, as illustrated in Figure 20. This deviation is considered minor and does not substantially affect the overall wear volume estimation.
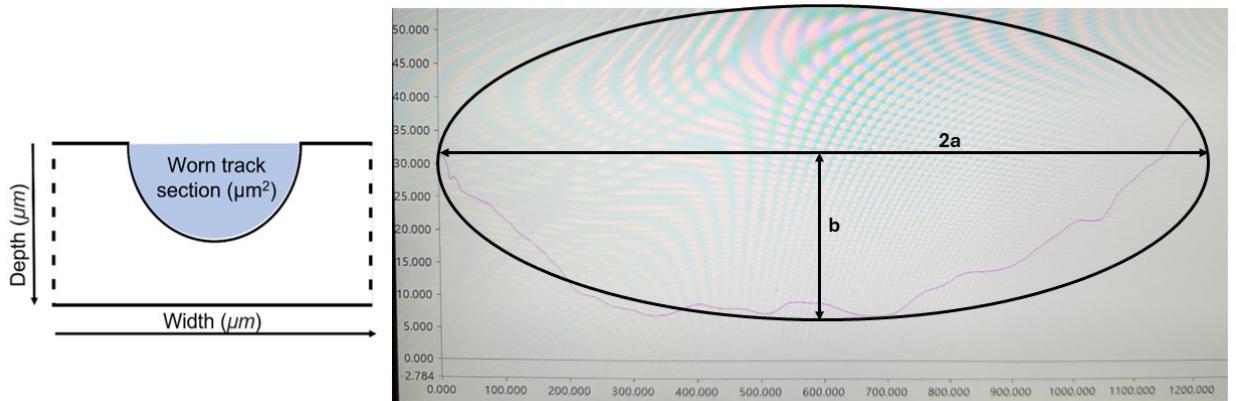
Figure 20: Schematic of wear track cross sectional area calculation.

Finally, the wear rate was calculated in accordance with ASTM G99, using Equation 10, where V is the wear volume (mm^2), F is the applied normal load (N), and s is the sliding distance (m).

$$\text{Wear rate} = \frac{V}{F \cdot s} \qquad (10)$$

30

4.2.4 Electrochemical Properties

To evaluate the corrosion protection performance of the sol-gel sealing layer on the substrate system, electrochemical measurements were employed as the primary analytical method. The most commonly used techniques included open circuit potential (OCP), potentiodynamic polarization (PDP), and electrochemical impedance spectroscopy (EIS). Given the complexity of corrosion behavior, a single measurement is often insufficient for comprehensive characterization. However, due to the limited number of specimens available, this study ultimately employed two samples each for the five-layer and two-layer sol-gel sealed HVAF Hastelloy C276, as well as one sample with only the HVAF Hastelloy C276 coating for EIS testing. Additionally, one specimen from each of the three coating types was subjected to PDP testing on two different surface areas to enhance data reliability. These electrochemical tests provide insight into the expected service life of the materials under corrosive conditions. All electrochemical measurements were conducted using a conventional three-electrode configuration. The test sample served as the working electrode (red lead), while either an Ag/AgCl was used as the reference electrode (white lead) due to their stable potentials. A platinum plate was used as the counter electrode (blue lead) to complete the circuit. The schematic of the three-electrode cell setup is shown in Figure 21.
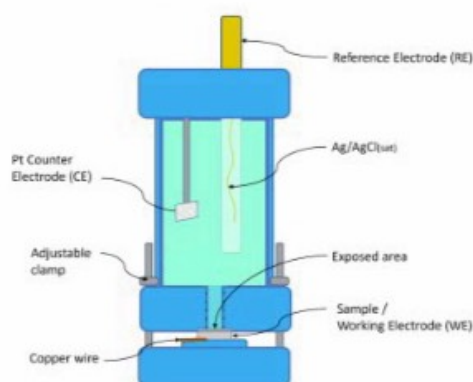
(a) Schematic of electrochemical cell set-up for OCP, EIS and PDP measurements
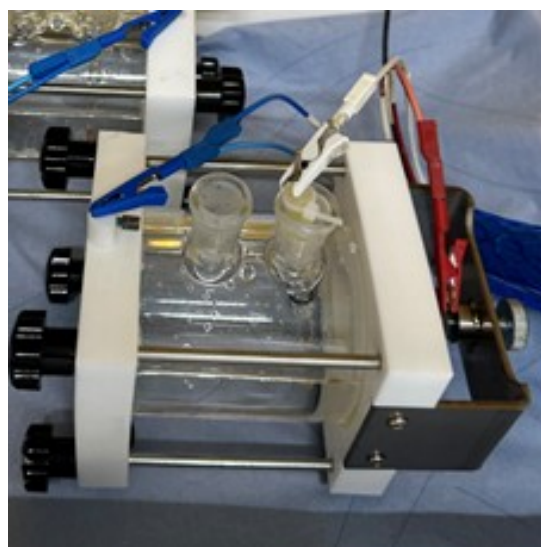
(b) Actual electrochemical cell setup for OCP, EIS and PDP measurements

Figure 21: Electrochemical cell setup

All electrochemical tests in this study were conducted at room temperature using a 0.1 M NaCl solution as the electrolyte. The test specimens were categorized into three groups as mentioned: (1) samples coated with one layer of sol-gel SiO_2 and another one layer of sol-gel SiO_2/ZrO_2 (two layers in total), (2) samples coated with one layer of sol-gel SiO_2 and another four layers of sol-gel SiO_2/ZrO_2 (five layers in total), and (3) samples with only the HVAF sprayed Hastelloy C276 coating, which is without any sol-gel sealing layer. All samples were tested in a conventional three-electrode cell, with an exposed working area of 0.785 cm^2. The three electrode system was connected to a Bio-Logic CSP-300 multichannel potentiostat, and all experiments were controlled via EC-Lab software. The electrochemical evaluation was divided into two main parts, including EIS and PDP, also as mentioned in the previous paragraphs. The combined results from these tests were used to compare the corrosion protection performance of samples with and without the sol-gel sealing layer. Prior to both EIS and PDP measurements, OCP measurements were performed to determine the system's steady-state reference potential. Since EIS was used to monitor changes in impedance over a three-week period and samples could not be moved during the test, two specimens per group were allocated specifically for EIS measurements. In

contrast, PDP testing was more time efficient and allowed measurements at two different regions on the same sample surface. After completing one PDP scan, the electrode position was shifted to a new area on the same sample to perform the second scan.

All PDP and EIS measurements were preceded by a 1 hour OCP stabilization period to ensure a steady reference potential. The OCP measurement window was defined with an voltage range minimum and maximum of -2.5 V and +2.5 V, respectively. These values do not influence the measured OCP values but serve to define the instrument's permissible detection limits, thereby preventing the system from exceeding its operational safety range. For EIS testing, the total measurement duration was set to 21 days, with measurements conducted once per day. The frequency range spanned from 10 mHz to 100 kHz, with an excitation voltage of 10 mV sinusoidal amplitude. The corrosion resistance of the coating was evaluated by analyzing the magnitude of the impedance |Z| at low frequency, 10 mHz, from both Bode and Nyquist plots. PDP measurements were conducted at a scan rate of 0.5 mV/s, starting from a potential 300 mV below the OCP and sweeping up to 1500 mV above the OCP or until breakdown occurred. The corrosion behavior was assessed by plotting corrosion potential (E) versus the absolute value of the corrosion current density taken in logarithmic form log|i|, and the corrosion rate was calculated using the built-in analysis tools and formulas available in the EC-Lab software.

4.2.5 HIC Resistance

The immersion test conducted in this study was performed in accordance with NACE TM0284, a widely recognized industry standard for evaluating the hydrogen induced cracking resistance of materials in sour environments. This test is designed to determine the suitability of materials for acidic environments, as well as their barrier properties and corrosion resistance. It involves immersing metal samples in a solution containing H_2S, NaCl, and CH_3COOH in distilled water at approximately 25 °C for 96 hours, followed by post-test examination. The setup is shown in Figure 22.

In this study, four samples measuring 10 cm × 2 cm were tested, including one carbon steel S235JR substrate, one with HVAF coated Hastelloy C276, one with two-layer SiO_2/ZrO_2 sol-gel and HVAF coated Hastelloy C276, and one with five-layer SiO_2/ZrO_2 sol-gel and HVAF coated Hastelloy C276. By comparing the test results among these samples, the protective performance of the 250 μm thick HVAF Hastelloy C276 coating and the potential enhancement provided by the sol-gel sealing layers were assessed. Quantitative evaluation was conducted by calculating the crack sensitivity ratio (CSR), crack length ratio (CLR), and crack thickness ratio (CTR) on the surface of cross section to determine the susceptibility of the coatings to HIC and their effectiveness in shielding the underlying substrate.

The acidic test solution was prepared in a separate vessel using H_2S gas, NaCl, and CH_3COOH. A mixture of 5 wt% NaCl, 0.5 wt% CH_3COOH, and distilled water was first prepared to yield an initial pH around 2.7. This solution was immediately sealed and purged with nitrogen gas at 100 cm^3/min per liter of solution near the bottom of the container for 60 minutes. After purging, the samples were placed into the testing vessel, the prepared solution was transferred in, and nitrogen purging was repeated under the same conditions. Following this, H_2S gas was introduced into the solution via bubbling at a rate of 200 cm^3/min per liter of solution for 60 minutes, and a constant H_2S overpressure was maintained to ensure saturation throughout the test. At the conclusion of the 96-hour exposure, iodometric titration and pH measurements were performed to confirm an H_2S concentration of at least 2300 ppm and a pH value below 4.0.

Post-immersion evaluations were performed using OM to assess changes on the sample top surface, such as blistering, and SEM to examine cross sectional morphology. The SEM analysis enabled the calculation of CSR, CLR, and CTR, which are standard metrics for quantifying HIC susceptibility. The formulas are shown in Equation 11, 12 and 13, where a represents the total crack length (mm), b represents the maximum crack depth (mm), W represents the sample width on the surface of cross section (mm), and T represents the sample

(a) Equipment setup for the immersion test, and all samples are inside the test container.

(b) Appearance of the samples immersed during the immersion test.

Figure 22: Immersion test setup

thickness on the surface of cross section (mm), as displayed in Figure 23.
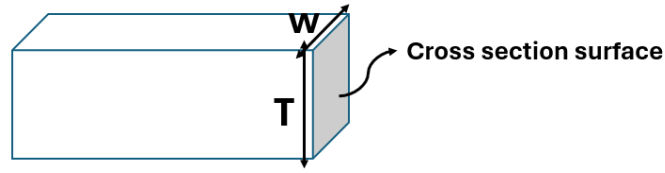
Figure 23: Illustration of W and T in the formula for calculating CSR, CLR, and CTR on the sample cross section.

$$CSR = \frac{\sum(a \times b)}{W \times T} \times 100\% \tag{11}$$

$$CLR = \frac{\sum a}{W} \times 100\% \tag{12}$$

$$CTR = \frac{\sum b}{T} \times 100\% \tag{13}$$

5 RESULTS AND DISCUSSION

This chapter provides an analysis and discussion of each experimental result presented in the previous chapter. Finally, a summary of the experimental results is presented.

5.1 SURFACE MORPHOLOGY AND MICROSTRUCTURE

This subsection discusses the OM, SEM, and EDS analysis results of the substrate, the HVAF sprayed Hastelloy C276 coating, and the SiO_2/ZrO_2 sol-gel sealing layer of varying thicknesses. Additionally, the measurements of porosity and surface roughness will also be included and analyzed in this subsection.

5.1.1 Substrate

Prior to coating, OM and scanning SEM analyses were conducted on the carbon steel SJ235 substrate to characterize its surface features and to assess its susceptibility to hydrogen-induced cracking as well as the presence of pre-existing defects.

The top surface and cross section of the substrate were first examined using OM to investigate the microstructural features, including defects, cracks, and inclusions. It should be noted that, due to the limited image clarity, the scale bar is not clearly visible. In all following OM images of this study, the scale bar located at the lower right corner corresponds to 100 μm.

(a) 200× (b) 500× (c) 700×
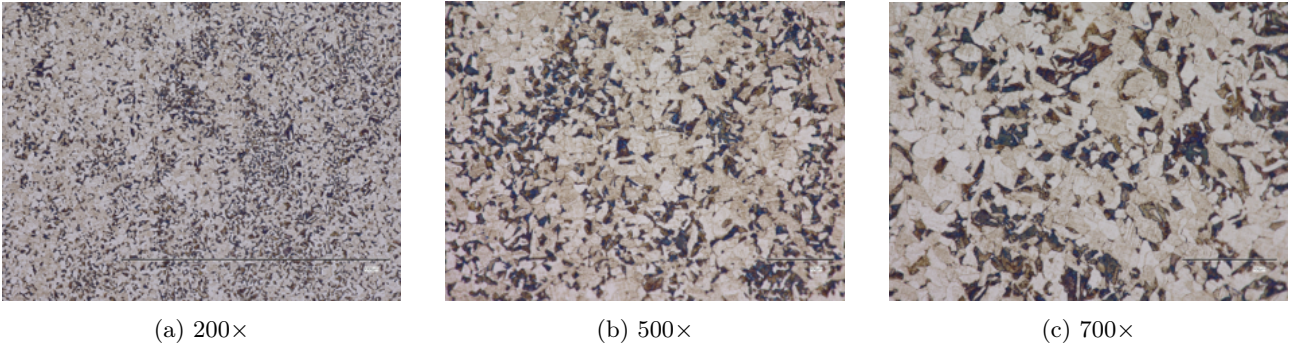
Figure 24: OM image of the carbon steel SJ235 substrate's top surface (scale bar: 100 μm)

(a) 200× (b) 500× (c) 700×
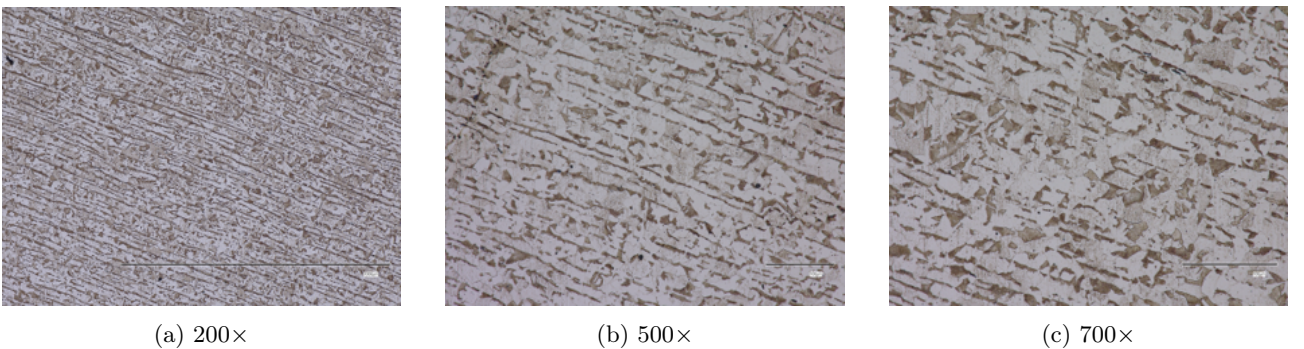
Figure 25: OM image of the carbon steel SJ235 substrate's cross section (scale bar: 100 μm)

The OM images of the top surface shown in Figure 24 and cross section shown in Figure 25 reveal distinct differences in microstructural morphology. The top surface exhibits a uniform two-phases microstructure, whereas the cross sectional view reveals an elongated, directionally oriented duplex structure, aligned with the rolling direction during substrate fabrication. At 700× magnification in the cross sectional image, several dark spots

are observed that do not appear to belong to either of the two primary phases. These dark features are presumed to be contaminants or inclusions. However, due to the limitations of optical microscopy, their precise nature cannot be determined, necessitating further analysis using SEM-EDS. In addition, phase area analysis was performed based on three $500\times$ OM images from both the top surface and cross section. As summarized in the Table 6 below, the bright phase accounted for approximately 78% of the total area on average, while the remaining 22% corresponded to the dark phase.

Area Ratio (Bright/Dark)	Measurement 1	Measurement 2	Measurement 3	Average
Top Surface	77% / 23%	78.8% / 21.2%	77.3% / 22.7%	77.7% / 22.3%
Cross Section	77.7% / 22.3%	78.5% / 21.5%	77.1% / 22.9%	77.8% / 22.2%

Table 6: Phase area analysis results based on $500\times$ OM images.

Following the OM observations, a more detailed understanding of the microstructure was obtained by combining SEM and EDS analysis. SEM images provide higher-resolution visualization of microstructural features. Figure 26 shows the SEM image of the top surface, while Figure 27 presents the cross sectional view.

(a) $200\times$ (b) $500\times$ (c) $700\times$
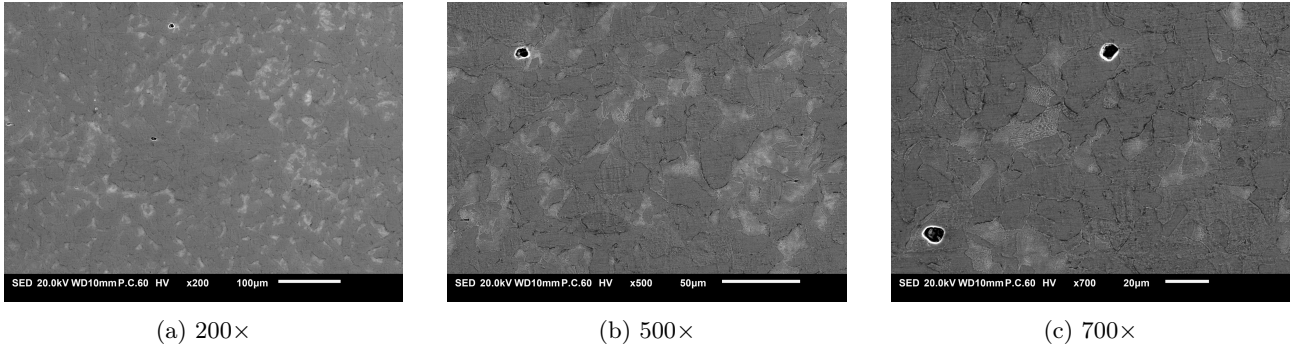
Figure 26: SEM image of the carbon steel SJ235 substrate's top surface

(a) $200\times$ (b) $500\times$ (c) $700\times$
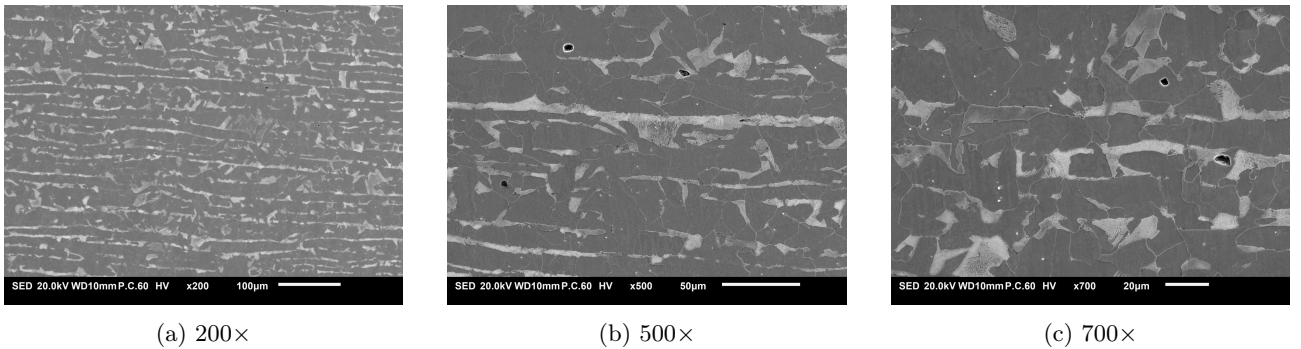
Figure 27: SEM image of the carbon steel SJ235 substrate's cross section

The microstructures observed in the SEM images were consistent with those seen in the OM images, confirming the presence of a duplex microstructure in both the top surface and cross section. The top surface exhibited a uniform duplex structure, whereas the cross section revealed an elongated duplex morphology aligned with the rolling direction.

However, upon closer examination of Figure 26c and Figure 27c, both SEM images taken at $700\times$ magnification, it can be observed that the lighter regions exhibit a distinct lamellar structure, which is a characteristic feature of pearlite. These areas can therefore be identified as pearlite grains. The remaining darker regions correspond to ferrite. Given that the carbon steel S235JR used in this study contains only 0.16 wt% carbon, this carbon

content is insufficient to form a complex microstructure comprising both pearlite and cementite. As such, the darker phase in the SEM images is identified as ferrite. This indicates that ferrite is the primary phase in S235JR carbon steel, while pearlite is the secondary phase. This conclusion is consistent with the results shown in Table 6, which indicates that ferrite accounts for approximately 78% of the total area, with pearlite comprising the remaining 22%.

Additionally, as shown in both Figure 26 and Figure 27, distinct inclusions can be clearly observed that do not belong to either of the two primary phases. These inclusions have an estimated size of approximately 10 to 20 μm. To identify their composition, a higher magnification SEM-EDS analysis was performed on the cross sectional image at 1200× using the "spectrum" analysis mode and analyzed in "point", with an accelerating voltage of 20 kV. The EDS results are shown in Figure 28.

Formula	mass%	Atom%	Sigma	K ratio	Line
C	17.60	44.94	0.03	0.0038541	K
Mg	0.11	0.13	0.02	0.0004201	K
Al	0.73	0.83	0.02	0.0030779	K
S	21.61	20.68	0.03	0.1293987	K
Ca	0.48	0.37	0.01	0.0034059	K
Mn	42.50	23.73	0.08	0.2689576	K
Fe	16.97	9.32	0.05	0.1101849	K
Total	100.00	100.00			
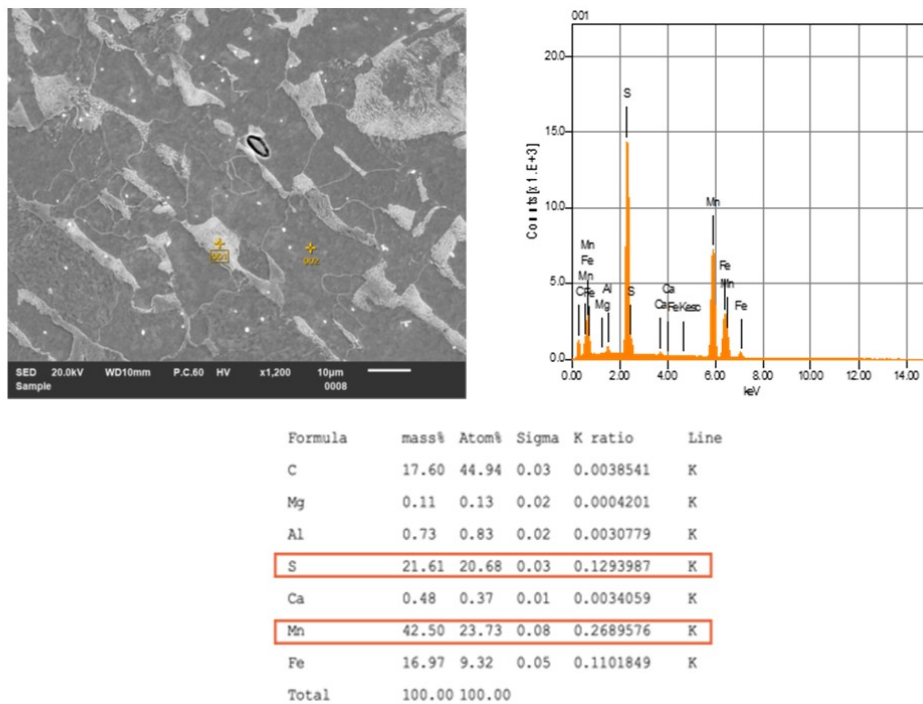
Figure 28: Spectrum mode EDS analysis in "point" configuration of inclusions on the substrate surface

The SEM-EDS results indicated that the inclusions contained a significant amount of manganese and sulfur, accounting for approximately 42.5 mass percentage and 21.6 mass percentage, respectively. Based on this composition, the inclusions are reasonably identified as manganese sulfide (MnS). TMnS inclusions are formed in carbon steels because manganese is intentionally added during steelmaking to prevent the formation of low-melting point FeS, which can cause hot shortness. The added manganese binds with sulfur to form the thermodynamically stable MnS phase, which subsequently precipitates during solidification as non-metallic inclusions. These MnS inclusions were primarily located in the central region of the steel, which is attributed to centerline segregation occurring during the solidification and cooling process of molten steel. During hot rolling, the center of the steel is the last region to solidify, leading to the preferential segregation of MnS into the central area [103].

5.1.2 HVAF Hastelloy C276 Coating

After the application of the HVAF sprayed Hastelloy C276 coating, the samples were immediately subjected to OM and SEM analysis. Based on previous studies, although HVAF coatings are generally denser than those produced by other thermal spray techniques, they still exhibit certain defects, such as pores, unmelted particles,

oxidation, and microcracks. Therefore, microscopic examination was performed to gain a clearer understanding of the surface morphology and microstructural features of the coating. In order to avoid damaging the samples, only the top surface was examined prior to the completion of the immersion test, the samples were not sectioned for cross-sectional analysis during this period.

(a) 200×   (b) 500×   (c) 700×
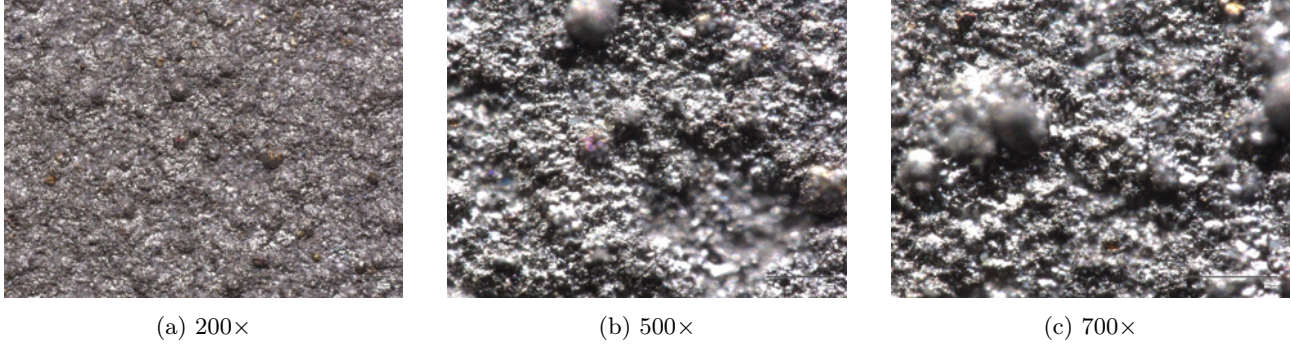
Figure 29: OM images of the unpolished HVAF Hastelloy C276 coating's top surface (scale bar: 100 μm)

(a) 200×   (b) 500×   (c) 700×
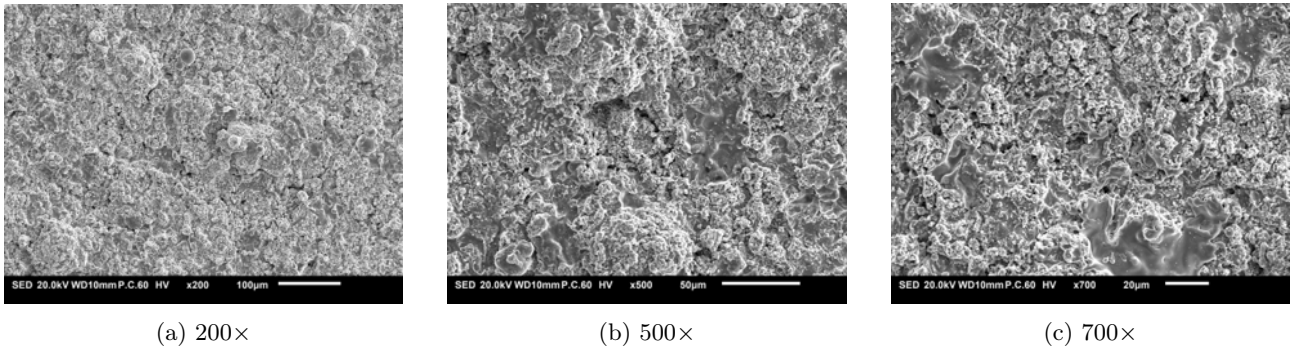
Figure 30: SEM images of the unpolished HVAF Hastelloy C276 coating's top surface

OM images, which are shown in Figure 29, revealed that the surface of the HVAF sprayed Hastelloy C276 coating was highly rough and consisted of distinct, layered particles. These particles were deposited sequentially, resulting in differences in particle height across the surface. This variation in elevation made it difficult to achieve uniform focus in OM imaging, often leading to blurred areas in the images. In contrast, the SEM images shown in Figure 30 exhibited significantly better clarity, with no signs of defocusing. In addition to morphological analysis, an EDS "spectrum" mode analysis in "area" configuration was performed on the coating. As displayed in Figure 31, the elemental composition was consistent with the nominal composition of Hastelloy C276, with nickel as the primary element, followed by chromium and molybdenum. A detectable amount of oxygen was also present, which may be attributed to surface oxidation, one of the typical defects observed in thermal spray coatings. However, on the unpolished coating surface, it was difficult to distinguish the specific regions where oxidation had occurred. While SEM images did reveal some small pores in the coating, no visible cracks or inclusions were identified. It is likely that these features may become more apparent after surface polishing. Notably, some regions in the SEM images, particularly at 500× and 700× magnifications, appeared darker and had a smeared or viscous texture. However, point analysis using EDS in spectrum mode, as shown in Figure 32, revealed that these regions had a composition nearly identical to that of Hastelloy C276. Although trace amounts of S and Sr were observed, their low mass percentages could be due to instrumental or analytical error. This suggests that the darker, viscous-looking areas correspond to fully melted Hastelloy C276 particles, whereas the surrounding spherical particles are unmelted.

Following the surface morphology analysis via OM and SEM, porosity analysis was performed on the unpolished coating using SEM images taken at 500× magnification. ImageJ software was used to quantify the porosity.

Formula	mass%	Atom%	Sigma	K ratio	Line
C	1.19	5.39	0.01	0.0004801	K
O	3.14	10.67	0.02	0.0113885	K
Cr	14.58	15.22	0.04	0.0794317	K
Fe	5.75	5.59	0.03	0.0313447	K
Ni	59.61	55.10	0.09	0.3238129	K
Mo	12.53	7.09	0.05	0.0420893	L
W	3.20	0.94	0.07	0.0081619	M
Total	100.00	100.00			
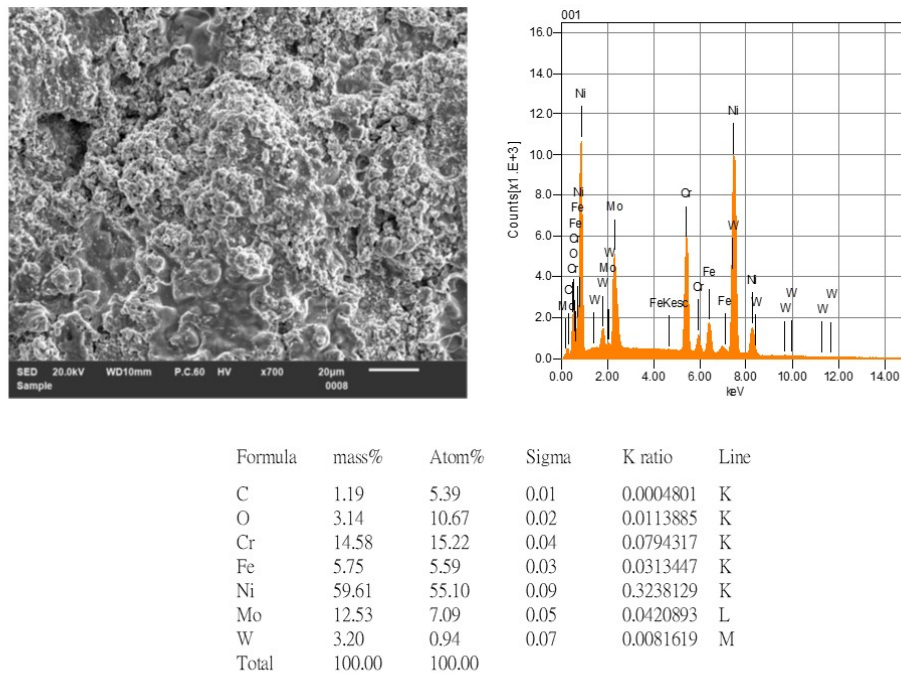
Figure 31: Spectrum mode EDS analysis in "area" configuration of unpolished HVAF Hastelloy C276 coating

Formula	mass%	Atom%	Sigma	K ratio	Line
C	2.28	10.98	0.01	0.0011483	K
S	0.09	0.16	0.03	0.0004856	K
Cr	14.34	15.95	0.03	0.0971265	K
Fe	5.69	5.89	0.02	0.0388180	K
Ni	56.15	55.29	0.07	0.3835536	K
Sr	0.40	0.27	0.06	0.0019245	L
Mo	16.79	10.12	0.09	0.0712382	L
W	4.25	1.34	0.08	0.0139870	M
Total	100.00	100.00			
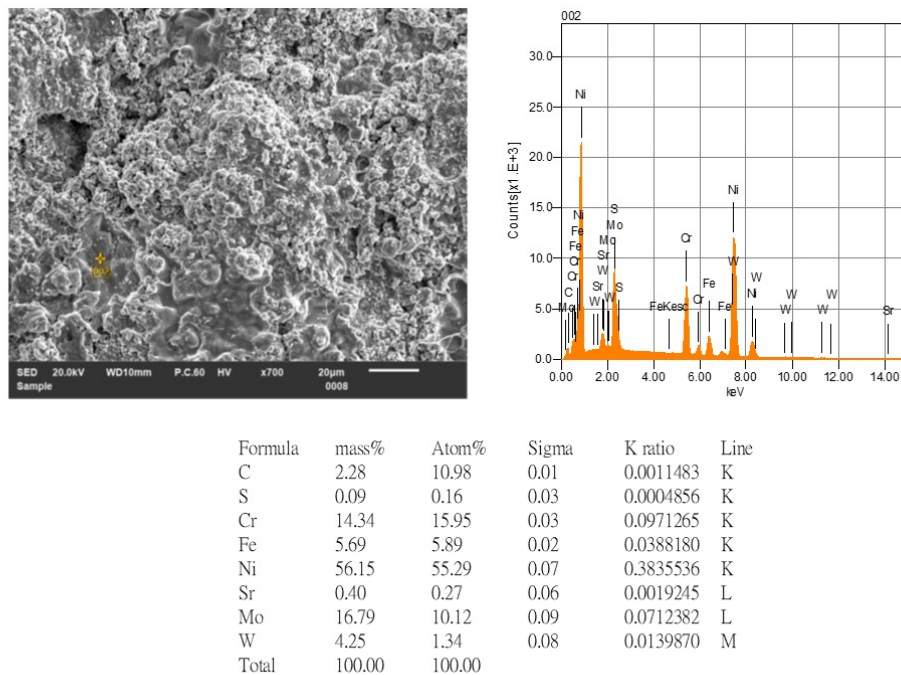
Figure 32: Spectrum mode EDS analysis in "point" configuration of the viscous-looking area on the unpolished HVAF Hastelloy C276 coating

The pore size range was defined as 0.2 to 5 μm^2, and any pores smaller than 0.2 μm^2 were excluded from the analysis. The analysis was repeated on five different SEM images to ensure statistical reliability. The resulting porosity data is summarized in Table 7.

As shown in Table 7, the unpolished HVAF sprayed Hastelloy C276 coating exhibited a low porosity of approxi-

38

	Count	Total Area (μm^2)	Average Size (μm^2)	Percentage of Area (%)
Average	1613	845.97	0.53	1.93
Standard Deviation	155	90.04	0.03	0.21

Table 7: Porosity information of the unpolished HVAF coating

mately 1.93%, with an average pore size of 0.53 μm^2. These values align well with initial expectations regarding the high density of HVAF coatings.

However, the unpolished surface was excessively rough, with a surface roughness significantly higher than the typical thickness of a single sol-gel layer deposited via dip coating, which is predicted by the Landau–Levich theory to be approximately 0.5 to 2 μm. Such high surface roughness could hinder the uniform adhesion of the sol-gel layer onto the HVAF coated surface. Therefore, it was ultimately decided to perform wet grinding and polishing on the HVAF Hastelloy C276 coating prior to sol-gel deposition to improve surface smoothness and ensure better coating compatibility.

After the wet grinding and polishing process, the HVAF sprayed Hastelloy C276 coating was re-examined using OM and SEM. As shown in the figure below, the surface morphology of the polished coating is noticeably different from that of the as-sprayed surface, highlighting the significant effect of surface treatment on the coating's topography.

(a) 200×   (b) 500×   (c) 700×
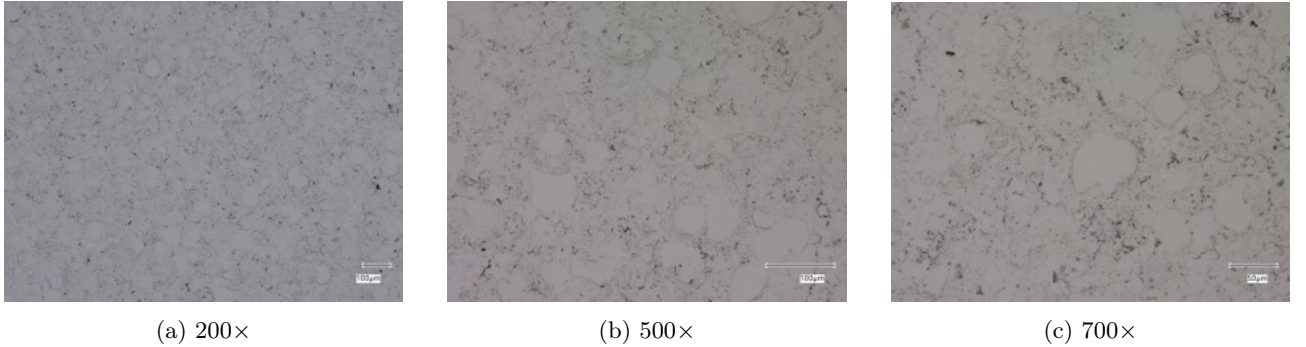
Figure 33: OM images of the polished HVAF Hastelloy C276 coating's top surface (scale bar: 100 μm)

(a) 200×   (b) 500×   (c) 700×
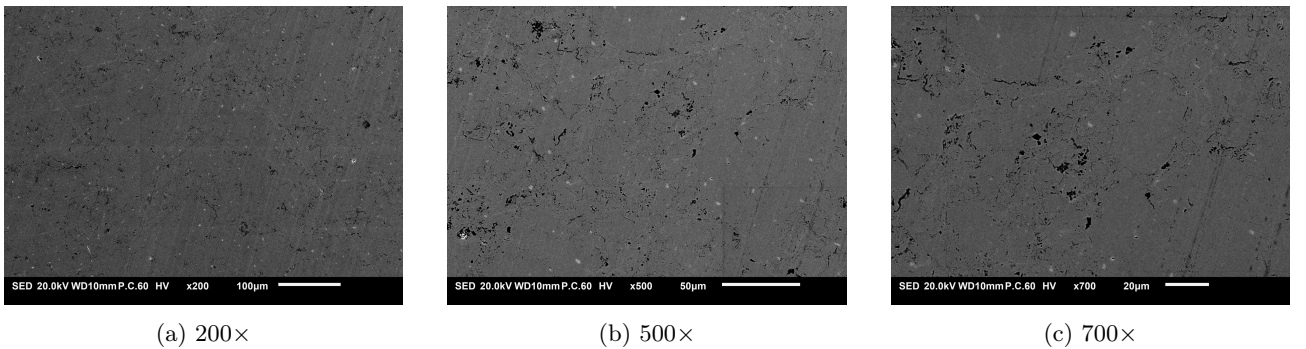
Figure 34: SEM images of the polished HVAF Hastelloy C276 coating's top surface

As shown in Figure 33, which are the OM images, and Figure 34, which are the SEM images, the surface defects commonly associated with HVAF coatings, including pores, microcracks, oxidation, and unmelted particles, became more clearly identifiable after surface treatment. These features are particularly evident at higher magnifications, such as 500× and 700×, where small pores are readily visible. In some cases, larger or interconnected pores appear to form microcracks. Additionally, the bright particles observed on the surface are presumed to

be unmelted particles. Elemental mapping via EDS in "map" mode further revealed the surface distribution of oxygen, as illustrated in Figure 35. According to the EDS mapping results, the oxygen content on the surface was relatively low, at only 6.41 at%. As a result, the corresponding map appears darker compared to elements with higher concentrations, such as Ni, Cr, and Mo. Nevertheless, this outcome confirms that oxidation did occur on the surface of the HVAF Hastelloy C276 coating. Furthermore, the distribution of oxygen in the map provides a general indication of the regions where oxidation took place.
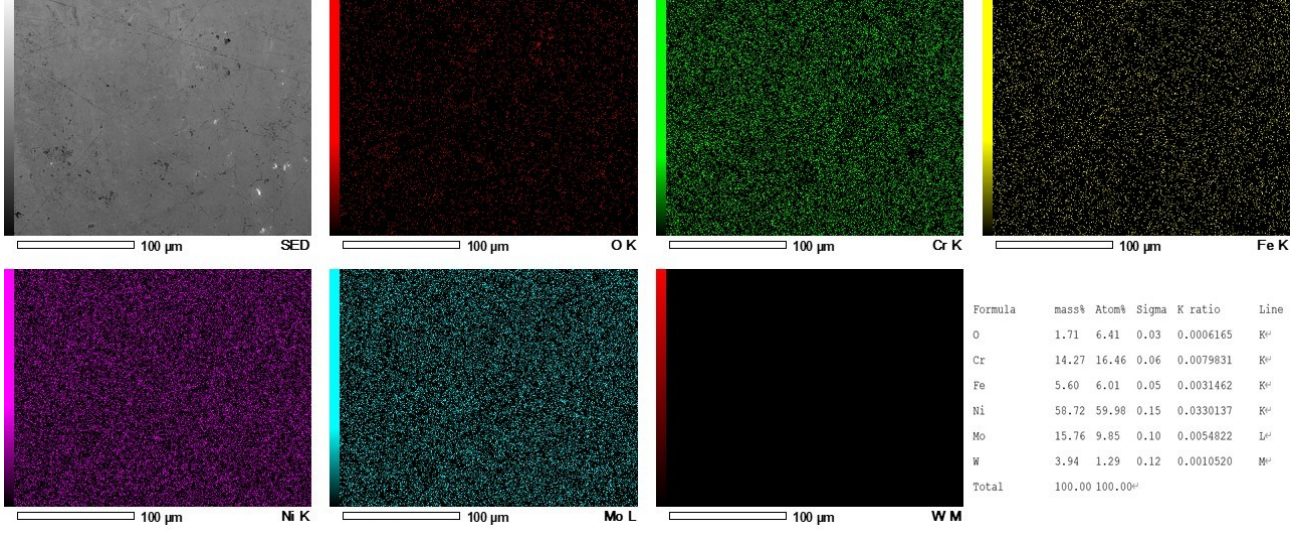
Figure 35: Map mode EDS analysis of the polished HVAF Hastelloy C276 coating

After performing wet grinding and polishing on the HVAF Hastelloy C276 coatings, porosity and surface roughness measurements were also conducted. The results are presented in the following Table 8 and Table 9, respectively.

	Ra (μm)	Rz (μm)	Rq (μm)
Average	3.33	14.95	3.91
Standard Deviation	0.28	2.66	0.25

Table 8: Roughness coefficients of the polished HVAF coating

	Count	Total Area (μm^2)	Average Size (μm^2)	Percentage of Area (%)
Average	1380	585.24	0.42	1.33
Standard Deviation	127	56.57	0.02	0.13

Table 9: Porosity information of the polished HVAF coating

As shown in Table 8, the average surface roughness values obtained from five measurements indicate a significant reduction in surface height variation and roughness parameters after surface treatment. Both Ra and Rq, commonly used roughness indicators, dropped below 4 μm, while the maximum height parameter Rz was less than 15 μm. In addition, the standard deviation values were not particularly large, suggesting that most of the measured values were close to the calculated average.

Regarding porosity, the results shown in Table 9 demonstrate a substantial reduction in total pore count, area, size, and overall porosity compared to the pre-polishing values presented in Table 7. This trend can likely be attributed to the higher surface roughness prior to wet polishing, which may have caused interparticle gaps on

the sprayed surface to be misidentified as pores by ImageJ. After polishing, the surface became smoother and some surface layers were removed, exposing previously hidden micropores and reducing the average pore size. Additionally, the improved smoothness likely enhanced the resolution and accuracy of image based porosity analysis, enabling better identification of smaller pores.

5.1.3 Sol-gel SiO$_2$/ZrO$_2$ Coating

After the deposition of the sol-gel SiO$_2$ and SiO$_2$/ZrO$_2$ coatings, no significant visual difference was observed compared to the uncoated sol-gel surface, due to the transparency and extremely thin nature of the sol-gel films. As a result, OM and SEM were employed to better characterize the surface morphology. Figures 36 through Figure 39 present the OM and SEM images of samples coated with two and five layers of sol-gel films, respectively.

(a) 200×   (b) 500×   (c) 700×
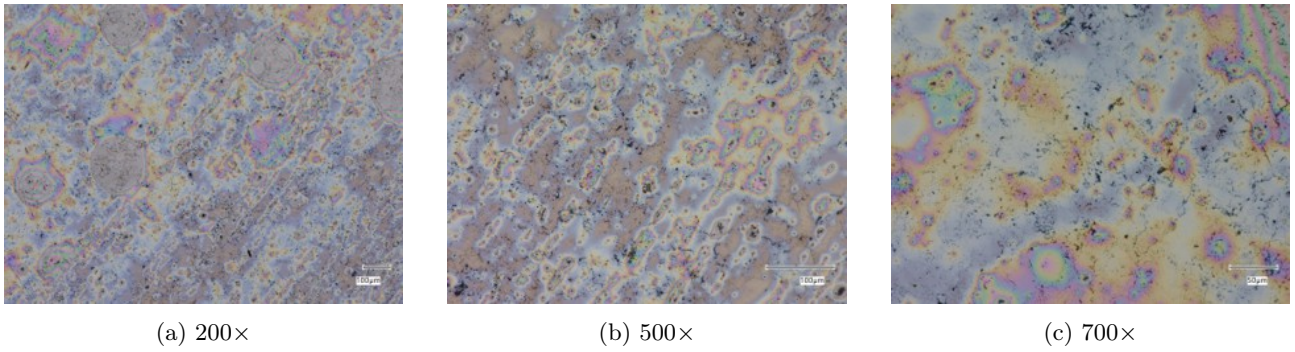
Figure 36: OM images of the 2-layer SiO$_2$/ZrO$_2$ sol-gel sealant's top surface (scale bar: 100 μm)

(a) 200×   (b) 500×   (c) 700×
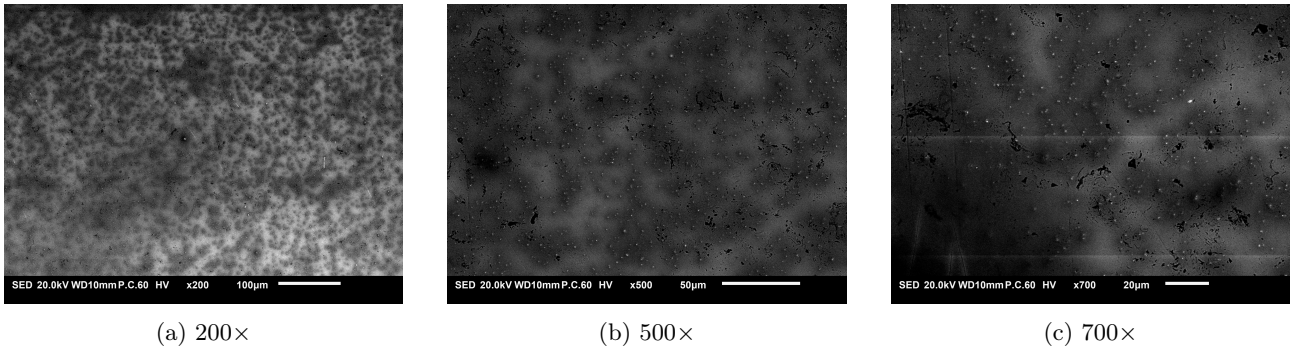
Figure 37: SEM images of the 2-layer SiO$_2$/ZrO$_2$ sol-gel sealant's top surface

As shown in the OM image in Figure 36, the most notable difference between the sample coated with two sol-gel layers and the uncoated HVAF Hastelloy C276 surface is the appearance of thin, water-stain-like iridescent films covering most of the surface. However, these are unlikely to be actual water stains, as each sol-gel layer underwent both ambient air drying and subsequent thermal treatment after deposition. Therefore, the nature of these features cannot be determined from OM alone, and further analysis using SEM and EDS is necessary to understand the surface changes resulting from the sol-gel sealing layer.

Figure 37 displays the OM image of the coated surface, revealing the presence of numerous fine particles and regions with darker coloration. These features are more clearly visible in Figure 37a (at 200× magnification). Moreover, surface pores and cracks are still observable in the image, indicating that these defects were not eliminated by the sol-gel deposition. Sol-gel layers chemically bond to the surface, forming Si–O–Metal bonds in the first layer, and Si–O–Zr or Si–O–Si covalent bonds in subsequent layers. These bonds are widely considered to provide excellent adhesion. From a mechanistic standpoint, sol-gel materials tend to coat the inner walls of

surface pores rather than completely filling them, which explains the continued visibility of such defects after coating.

| (a) 200× | (b) 500× | (c) 700× |

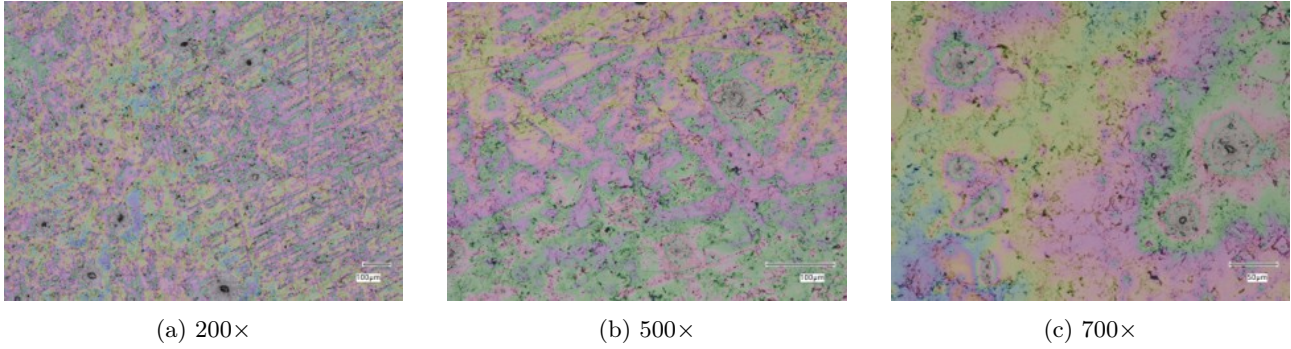Figure 38: OM images of the 5-layer SiO_2/ZrO_2 sol-gel sealant's top surface (scale bar: 100 μm)
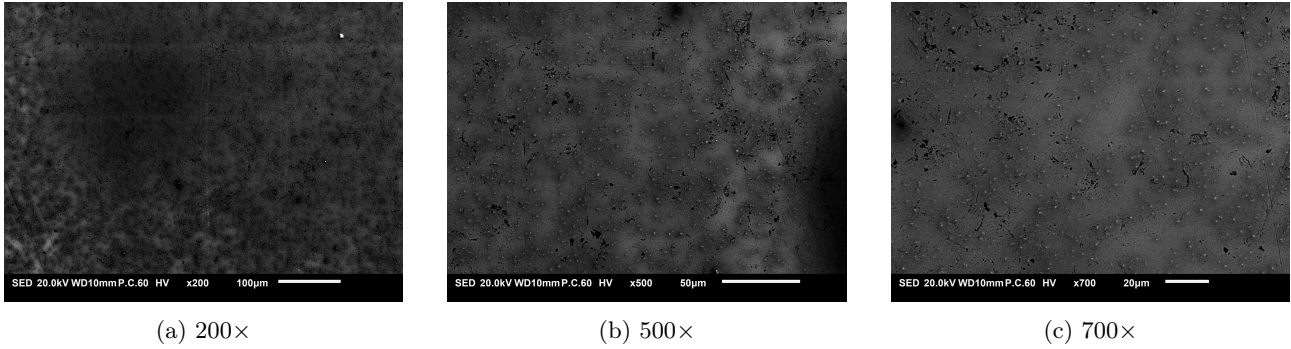

| (a) 200× | (b) 500× | (c) 700× |

Figure 39: SEM images of the 5-layer SiO_2/ZrO_2 sol-gel sealant's top surface

For the sample coated with five layers of sol-gel film, Figure 38 and Figure 39 reveal more extensive surface coverage compared to the two-layer-coated sample. In the OM image, the iridescent, water-stain-like film is significantly more pronounced and covers nearly the entire surface of the HVAF Hastelloy C276 coating, leaving very few exposed areas. The SEM images similarly show a higher density of shaded regions and bright particles than those observed on the two-layer-coated sample. These features appear more numerous and densely distributed, suggesting increased deposition and accumulation of sol-gel material. However, the exact chemical composition of these particles cannot be determined from imaging alone and requires further verification through EDS analysis.

Following the OM and SEM analyses, EDS was performed on the sample coated with five sol-gel layers using SEM images taken at 1500× magnification. This high magnification was selected to improve the accuracy of point selection and reduce potential measurement errors. However, as observed in Figure 37a and Figure 39, the contrast across the image at high magnification was relatively uniform, making it difficult to distinguish between actual surface features and shadowed regions, which is an issue inherent to this magnification level. Despite this limitation, three distinct types of regions were selected for analysis: areas containing white particles, areas without visible white particles or pores, and pore regions. For each type, four points were analyzed, resulting in a total of 12 measurement points. Points 1–4 correspond to the white particles, Points 5–8 to the regions without particles or pores, and Points 9–12 to the pore areas. The full EDS results from these 12 measurements are presented in Figure 40.

Based on the mass percentage results obtained from EDS analysis, points 1–4, which correspond to the white particles observed in the SEM images, showed approximately 15% silicon and 15% zirconium, along with about 30% oxygen. This composition suggests that these white regions are likely mixed SiO_2 and ZrO_2 particles. The

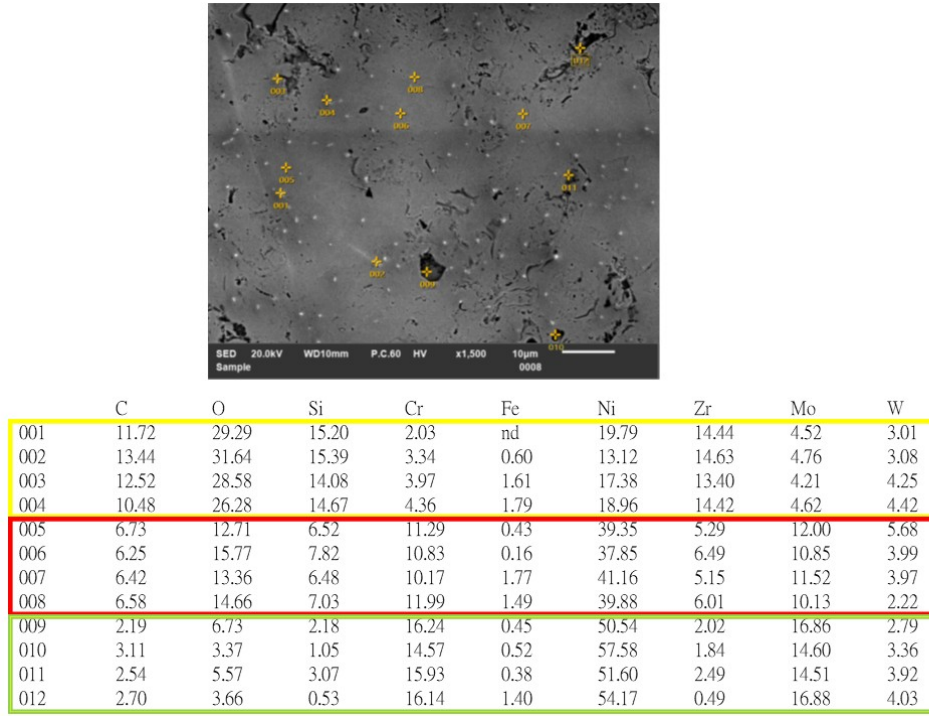|	C	O	Si	Cr	Fe	Ni	Zr	Mo	W
001	11.72	29.29	15.20	2.03	nd	19.79	14.44	4.52	3.01
002	13.44	31.64	15.39	3.34	0.60	13.12	14.63	4.76	3.08
003	12.52	28.58	14.08	3.97	1.61	17.38	13.40	4.21	4.25
004	10.48	26.28	14.67	4.36	1.79	18.96	14.42	4.62	4.42
005	6.73	12.71	6.52	11.29	0.43	39.35	5.29	12.00	5.68
006	6.25	15.77	7.82	10.83	0.16	37.85	6.49	10.85	3.99
007	6.42	13.36	6.48	10.17	1.77	41.16	5.15	11.52	3.97
008	6.58	14.66	7.03	11.99	1.49	39.88	6.01	10.13	2.22
009	2.19	6.73	2.18	16.24	0.45	50.54	2.02	16.86	2.79
010	3.11	3.37	1.05	14.57	0.52	57.58	1.84	14.60	3.36
011	2.54	5.57	3.07	15.93	0.38	51.60	2.49	14.51	3.92
012	2.70	3.66	0.53	16.14	1.40	54.17	0.49	16.88	4.03

Figure 40: Spectrum mode EDS analysis in "point" configuration of several ares on the 5-layer SiO_2/ZrO_2 sol-gel sealant

remaining detected elements were consistent with the composition of the underlying Hastelloy C276 coating, with nickel being the most abundant which is around 20%, followed by molybdenum, chromium, and tungsten, each of them is around 2–4%. Additionally, trace amounts of iron were detected at all points 2–12 except point 1, which are presumed to have originated from the underlying carbon steel S235JR substrate or the Hastelloy C276 coating, possibly due to slight exposure to the sol during the dip-coating process. However, as the iron content did not exceed 2 mass%, it is considered negligible.

At points 5–8, corresponding to regions without visible particles or pores, the EDS spectra were dominated by Hastelloy C276 elements, nickel (about 40%), molybdenum and chromium (about 10%), and tungsten (about 5%). In these regions, the mass percentages of silicon and zirconium dropped to around 5–7%, and oxygen to 12–15%. Although the concentrations of Si, Zr, and O were significantly lower than those in the white particle regions, their continued presence on the surface supports the conclusion that the sol-gel-derived SiO_2/ZrO_2 layer was successfully deposited and adhered to the HVAF Hastelloy C276 surface.

Finally, points 9–12, corresponding to pore regions, were primarily composed of Hastelloy C276 elements. The Si and Zr mass percentages were reduced to less than 3%, and oxygen content ranged from only 3–7%. This suggests that detecting SiO_2 and ZrO_2 on the inner pore walls using EDS is challenging, likely due to their minimal thickness and potential shadowing effects in recessed areas.

	Ra (μm)	Rz (μm)	Rq (μm)
Average	2.16	10.42	2.54
Standard Deviation	0.22	2.66	0.34

Table 10: Roughness coefficients of the two-layer sol-gel sealed sample

In addition, after applying the SiO_2/ZrO_2 sol-gel sealing layer, the samples were subjected to surface roughness testing. The results, as shown in Tables 10 and 11, indicate that the sol-gel sealed samples exhibit lower surface

	Ra (μm)	Rz (μm)	Rq (μm)
Average	1.91	8.89	2.23
Standard Deviation	0.13	1.49	0.12

Table 11: Roughness coefficients of the five-layer sol-gel sealed sample

roughness compared to the uncoated Hastelloy C276 samples, which is displayed in Table 8. The Ra values of two-layer and five-layer sol-gel sealed samples were approximately 2 μm, and the Rq values did not exceed 3 μm. This reduction may be attributed to the sol-gel layer partially filling surface pores and cracks, thereby smoothing the surface. However, due to the transparency of the sol-gel layer and the fact that it does not completely fill the pores, such improvements were not clearly visible under the microscope. When comparing the samples with two and five layers of sol-gel sealants, it was observed that increasing the number of layers led to a smoother surface. Nonetheless, the degree of improvement was not drastic, as the reduction in roughness parameters was relatively minor.

5.2 MICROHARDNESS

Based on the results of 20 microhardness measurements for each sample, all three configurations including the uncoated HVAF Hastelloy C276 coating, the sealing with two-layer SiO_2/ZrO_2 sol-gel, and the sealing with five-layer SiO_2/ZrO_2 sol-gel, exhibited hardness values generally ranging between 500 and 600 HV. The average values calculated from the 20 measurements for each sample are summarized in Table 12. Among the three, the sample coated with five sol-gel layers showed the highest average microhardness, followed by the two-layer coated sample, and finally the uncoated HVAF Hastelloy C276 coating. This result is likely attributed to the presence of micropores and microcracks inherent in the HVAF sprayed Hastelloy C276, which limit its surface hardness. After the application of the sol–gel SiO/ZrO coating, the ceramic layer not only possesses intrinsically high hardness but also effectively fills the pores and cracks on the substrate surface, allowing the applied load during hardness measurements to be more evenly distributed. Furthermore, surface roughness measurements revealed that the sol–gel coating significantly reduces surface roughness, with the five-layer sample being the smoothest, followed by the two-layer sample, and the uncoated sample exhibiting the highest roughness. This reduction in surface roughness also contributes to the microhardness results, as a smoother surface minimizes uneven contact during indentation, thereby enhancing the measured hardness. Consequently, the five-layer sample exhibited the highest and most consistent microhardness values, followed by the two-layer sample, while the uncoated sample showed the lowest values. In summary, although the improvement is not highly pronounced, the application of a SiO_2/ZrO_2 sol–gel sealing layer can indeed enhance the hardness of the HVAF-sprayed Hastelloy C276 system.

	Average (HV)	Standard Deviation
Hardness of Hastelloy C276 without any sol-gel	548.85	18.67
Hardness of Hastelloy C276 with 2-layer sol-gel	571.05	21.79
Hardness of Hastelloy C276 with 5-layer sol-gel	580.30	19.45

Table 12: Results of the microhardness measurement

5.3 WEAR RESISTANCE

Based on the results presented in Tables 13, 14, and

However, the difference in wear resistance between the samples with two and five layers of sol-gel sealing layer was not significant. Statistical analysis revealed that in some cases, the two-layer samples exhibited better wear

performance, while in others, the five-layer samples performed better. On average, the five-layer samples showed slightly lower wear rates than the two-layer ones, suggesting that increasing the number of sol-gel layers may help reduce wear. Nevertheless, further experimental data are needed to validate this hypothesis.

	Without sol-gel	2-layer sol-gel	5-layer sol-gel
Measurement 1 (Radius = 3.016 mm)	0.877	0.825	0.797
Measurement 2 (Radius = 5.603 mm)	0.901	0.819	0.744
Measurement 3 (Radius = 8.038 mm)	0.831	0.763	0.777
Average	0.870	0.802	0.773

Table 13: Results of the wear volume (mm^3) measurement

	Without sol-gel	2-layer sol-gel	5-layer sol-gel
Measurement 1 (Radius = 3.016 mm)	1.75E-03	1.65E-03	1.59E-03
Measurement 2 (Radius = 5.603 mm)	1.80E-03	1.64E-03	1.49E-03
Measurement 3 (Radius = 8.038 mm)	1.66E-03	1.53E-03	1.55E-03
Average	1.74E-03	1.61E-03	1.55E-03

Table 14: Results of the wear rate (mm^3/Nm) measurement

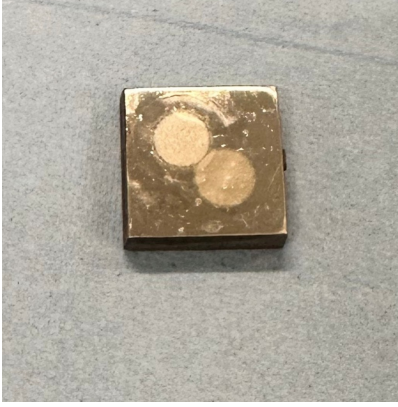|	Without sol-gel	2-layer sol-gel	5-layer sol-gel
Measurement 1 (Radius = 3.016 mm)	1.75E+06	1.65E+06	1.59E+06
Measurement 2 (Radius = 5.603 mm)	1.80E+06	1.64E+06	1.49E+06
Measurement 3 (Radius = 8.038 mm)	1.66E+06	1.53E+06	1.55E+06
Average	1.74E+06	1.61E+06	1.55E+06

Table 15: Results of the wear rate (μm^3/Nm) measurement

5.4 ELECTROCHEMICAL PROPERTIES

Figure 41 and 42 show the samples after undergoing PDP and EIS tests. The apparent differences in color are primarily due to lighting conditions, these are all the same type of sample. On the three samples tested with PDP, clear signs of corrosion are visible within the circular areas corresponding to the two measurements. In contrast, the three samples subjected to EIS testing show pronounced corrosion marks along the edges of the circular regions, whereas the interior areas exhibit less noticeable signs of corrosion.

Before conducting the PDP test, OCP measurements were first performed to confirm the stabilization of the corrosion potential. As shown in Figure 43, the time versus potential plots from the OCP tests indicate that the 5-layer sol-gel samples (blue and green lines) exhibited higher corrosion potentials than the 2-layer sol-gel samples (gray and red lines). On the other hand, the sample without sol-gel sealing layer (pink line) displayed the lowest potentials among all specimens. However, since OCP mainly serves to ensure that a stable potential is reached, performance evaluation must rely on PDP and EIS results.

Following potential stabilization, the PDP experiments were carried out, which is displayed in Figure 44. The results, plotted as corrosion potential versus log-transformed current density, exhibit the typical V-shaped polarization curve. Using the EC-Lab software's built-in Tafel extrapolation function, linear regions in the

(a) HVAF Hastelloy C276 without SiO$_2$/ZrO$_2$ sol-gel sealing layer
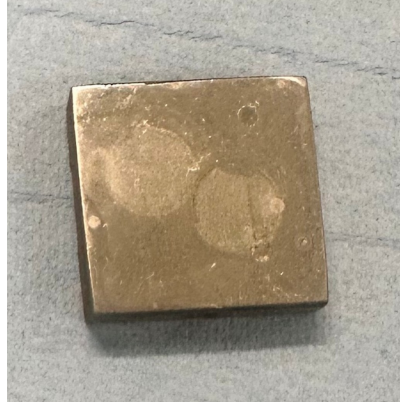
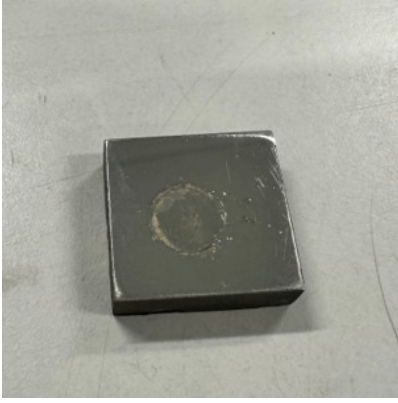(b) HVAF Hastelloy C276 with 2-layer SiO$_2$/ZrO$_2$ sol-gel sealing layer
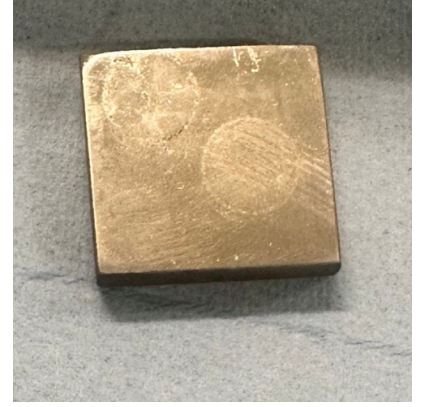
(c) HVAF Hastelloy C276 with 5-layer SiO$_2$/ZrO$_2$ sol-gel sealing layer
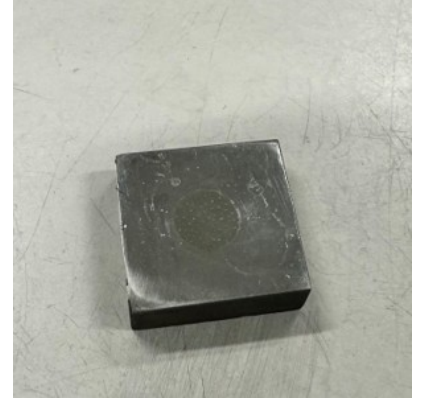
Figure 41: Picture of the samples after PDP test.

(a) HVAF Hastelloy C276 without SiO$_2$/ZrO$_2$ sol-gel sealing layer

(b) HVAF Hastelloy C276 with 2-layer SiO$_2$/ZrO$_2$ sol-gel sealing layer

(c) HVAF Hastelloy C276 with 5-layer SiO$_2$/ZrO$_2$ sol-gel sealing layer

Figure 42: Picture of the samples after EIS test.

cathodic and anodic branches were fitted, and their intersection provided the corrosion potential (E_{corr}) and corrosion current density (i_{corr}). Based on ASTM G102, the equivalent weight of Hastelloy C276 was calculated to be 22.61g, and its density was taken as 8.89 g/cm^3. These values, along with the i_{corr} obtained, were input into EC-Lab to calculate the corrosion rate, as shown in Table 16.

	E_{corr} (mV)	i_{corr} (mV)	Corrosion Rate (mm/year)
2-layer SiO$_2$/ZrO$_2$ sol-gel (1)	-300.691	0.094	9.97E-04
2-layer SiO$_2$/ZrO$_2$ sol-gel (2)	-323.826	0.098	1.03E-03
5-layer SiO$_2$/ZrO$_2$ sol-gel (1)	-295.674	0.055	5.83E-04
5-layer SiO$_2$/ZrO$_2$ sol-gel (2)	-302.814	0.026	2.76E-04
Without SiO$_2$/ZrO$_2$ sol-gel	-322.045	0.241	2.56E-03

Table 16: Results of the PDP test after Tafel extrapolation

Although the OCP results indicated that the uncoated samples exhibited the lowest stabilized potential, the PDP results revealed that they had the highest i_corr values, resulting in the greatest corrosion rates among all samples. In contrast, both the five-layer and two-layer sol–gel sealed samples showed markedly reduced corrosion rates. While some variation was observed between the two five-layer datasets, likely due to surface non-
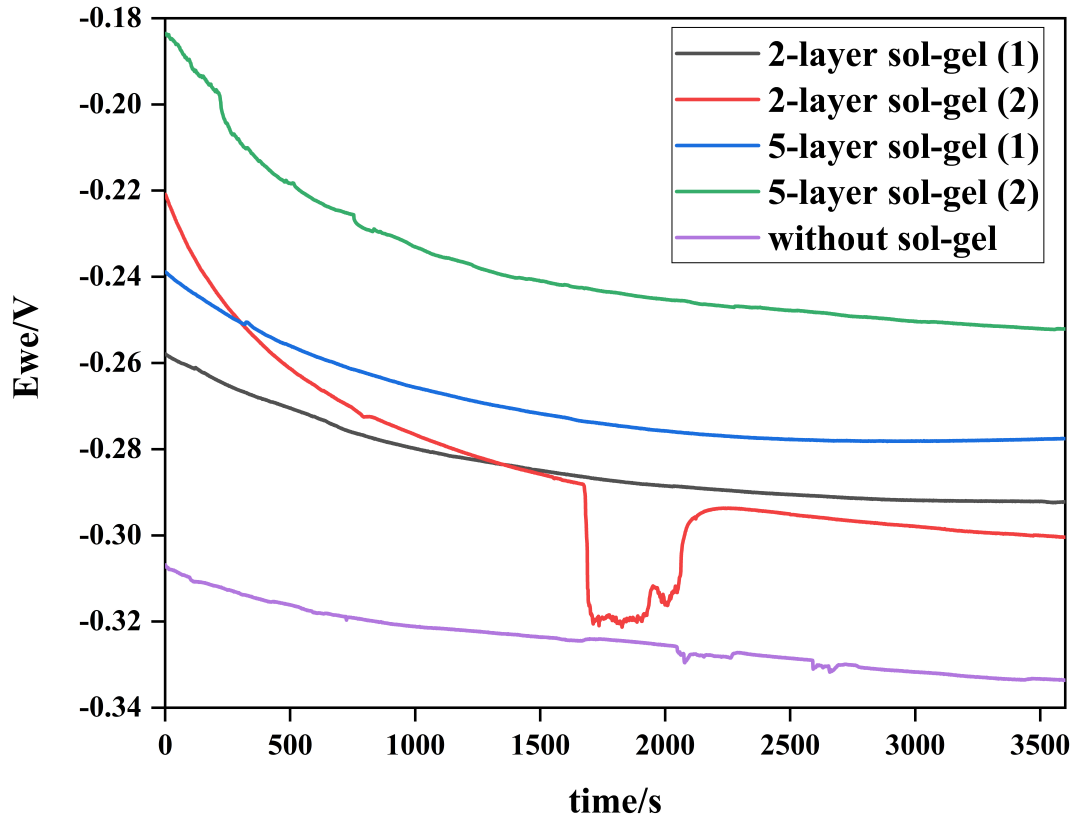
Figure 43: Result of OCP test, time v.s. potential (E)

uniformities, still both consistently exhibited the lowest corrosion rates overall, with reductions of approximately 4–10 times compared to the uncoated samples and about 2–4 times compared to the two-layer sol–gel samples. This improvement can be attributed to the SiO_2/ZrO_2 sol–gel sealing layer, which inhibits electrolyte diffusion by filling pores and cracks, increasing barrier layer thickness, and enhancing path tortuosity, while the inherent chemical inertness of SiO_2 and ZrO_2 in acidic, alkaline, and chloride-containing environments provides long-term protection. Compared with two-layer coatings, the five-layer system benefits from multiple cycles of drying and heat treatment, which more effectively fill microdefects from previous layers, resulting in a denser structure and significantly reduced permeability. Overall, the PDP results confirm that the SiO_2/ZrO_2 sol–gel sealing layer effectively suppresses corrosion, and within the tested range, increasing the number of coating layers leads to improved corrosion resistance.

Based on the EIS measurements conducted over the 21-day testing period, the Bode plot results in Figure 45 reveal pronounced impedance differences among the five sample groups, particularly in the low-frequency range of 0.01–1 Hz. The two samples coated with the five-layer sol–gel exhibited the highest and most stable impedance within this frequency range, especially the five-layer sol–gel (2) sample in Figure 45d showing the maximum |Z| value, indicating superior and consistent barrier performance. In comparison, the two samples coated with the two-layer sol–gel sealing layer displayed lower impedance values than their five-layer counterparts, although their impedance still exceeded that of the uncoated HVAF Hastelloy C276 sample.

Notably, for both the two-layer and five-layer sol–gel sealed samples, a sharp decrease in impedance was ob-
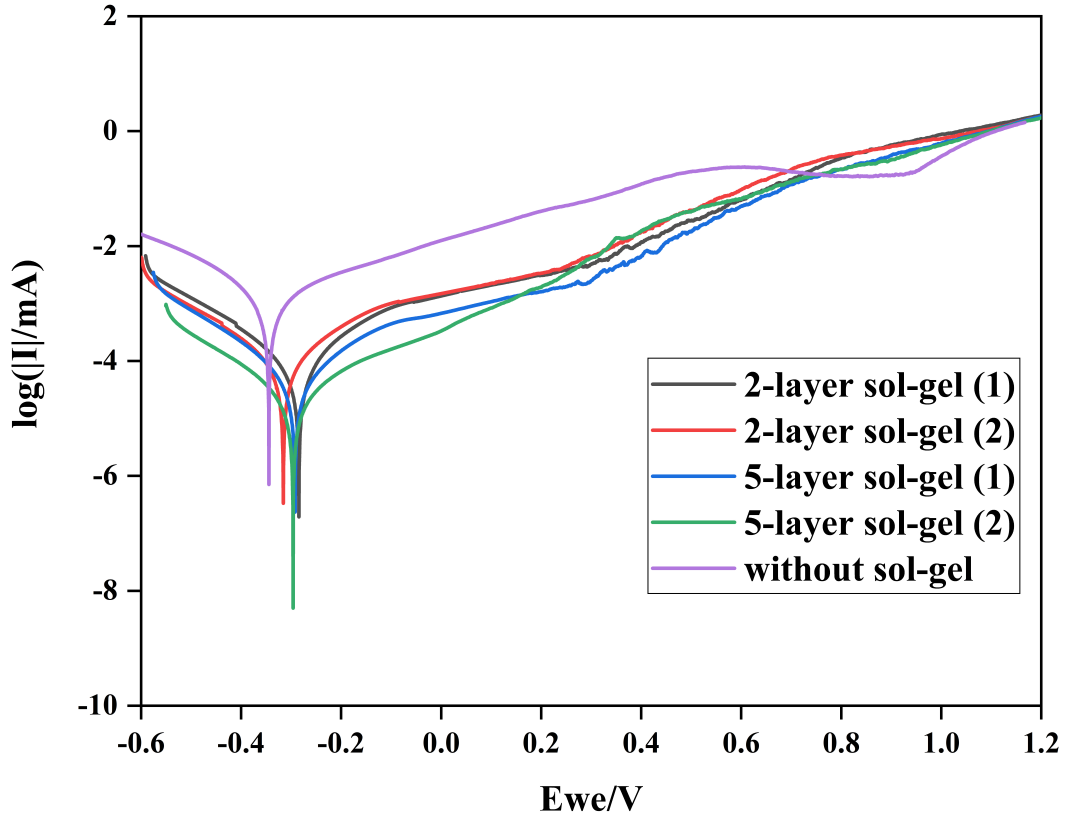
Figure 44: Result of PDP test, potential (E) v.s. log |i|

served from Day 1 to Day 3. This decline is likely attributable to the rapid penetration of the electrolyte into micropores and interfacial defects within the sol–gel sealing layer during the early exposure period, which increases capacitance, decreases resistance, and results in a swift drop in low- to mid-frequency impedance. The inherently hydrophilic nature of Si–OH and Zr–OH functional groups in the sol–gel network likely accelerates this initial water uptake. After approximately three days, most pore channels become saturated with water, and subsequent impedance changes are governed by ionic diffusion through pre-existing pathways, leading to a slower rate of impedance decline.

Despite the gradual reduction in impedance over time, all four sol–gel sealed samples maintained slightly higher impedance values than the uncoated HVAF Hastelloy C276 sample at Day 21. These results clearly demonstrate the beneficial role of the SiO_2/ZrO_2 sol–gel coating in enhancing corrosion resistance.

The Nyquist plot presented in Figure 46 further supports the earlier observations and directly corresponds to the Bode plot results, as both were obtained from measurements on the same set of samples, differing only in the method of data representation. As shown, the five-layer sol–gel (2) sample, which exhibited the highest low-frequency impedance in the Bode plot, also displays the largest semicircle in the Nyquist plot. Specifically, as illustrated in Figure 46d, its real impedance (x-axis) reaches approximately 700,000 Ω, while its imaginary impedance (y-axis) is around 350,000 Ω.

Although the five-layer sol–gel (1) sample does not reach the same impedance magnitude as the five-layer sol–gel (2) sample, its values are still markedly higher than those of the two two-layer sol–gel sealed samples. Consistent
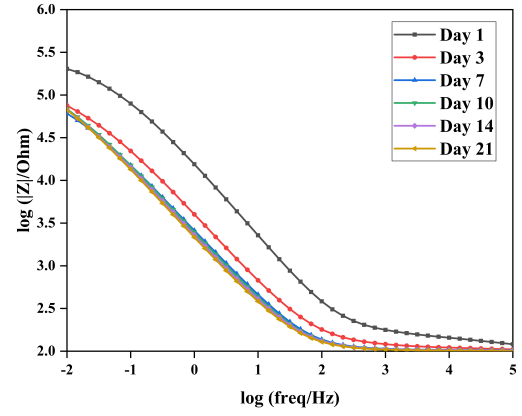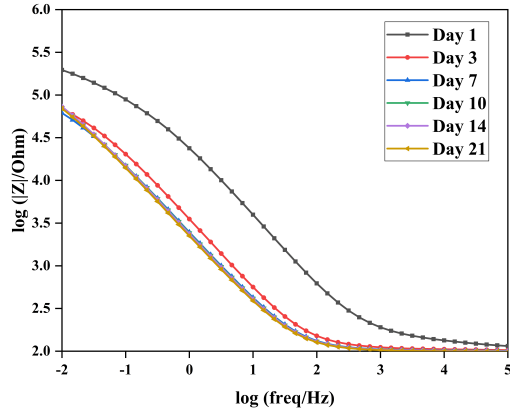
48

(a) HVAF Hastelloy C276 coating with two-layer sol-gel (1) (b) HVAF Hastelloy C276 coating with two-layer sol-gel (2)
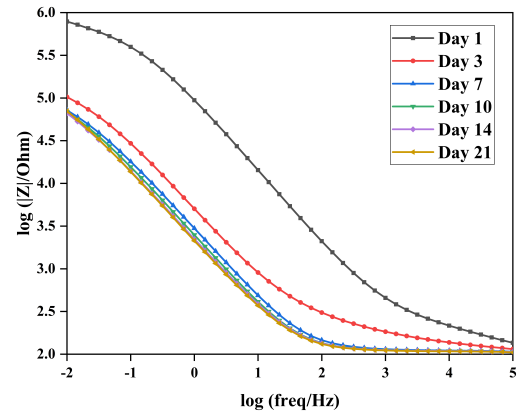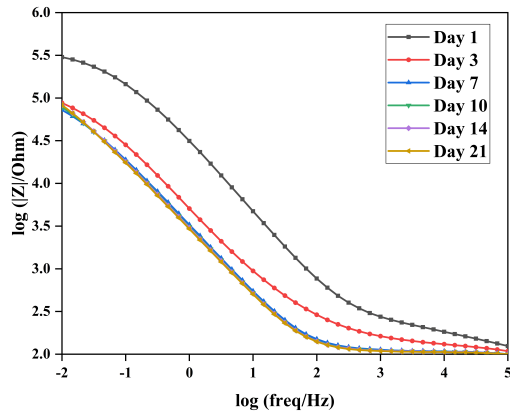
(c) HVAF Hastelloy C276 coating with five-layer sol-gel (1) (d) HVAF Hastelloy C276 coating with five-layer sol-gel (2)
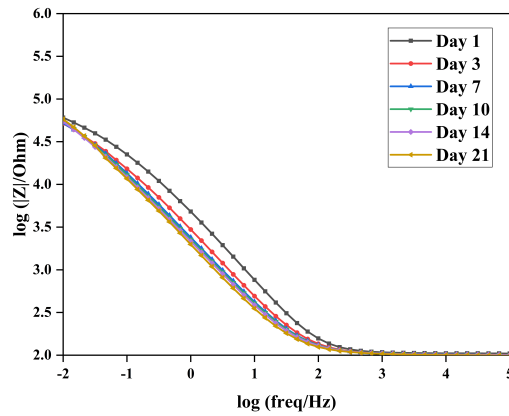
(e) HVAF Hastelloy C276 coating without sol-gel

Figure 45: Results of EIS test for 21 days, Bode plot
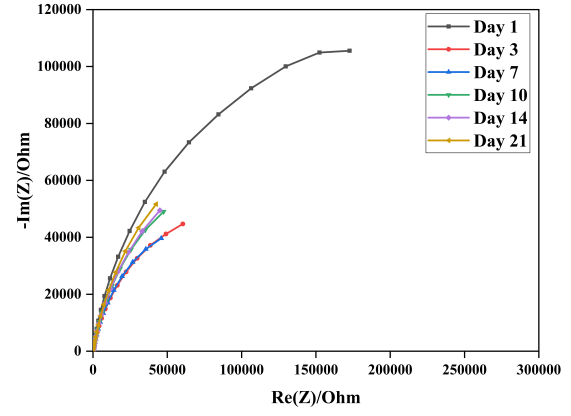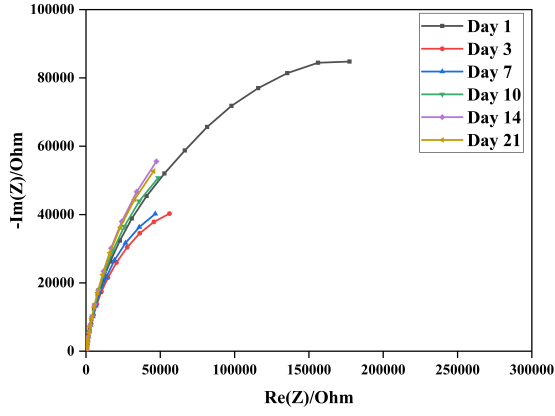
(a) HVAF Hastelloy C276 coating with two-layer sol-gel (1) (b) HVAF Hastelloy C276 coating with two-layer sol-gel (2)

(c) HVAF Hastelloy C276 coating with five-layer sol-gel (1) (d) HVAF Hastelloy C276 coating with five-layer sol-gel (2)

(e) HVAF Hastelloy C276 coating without sol-gel

Figure 46: Results of EIS test for 21 days, Nyquist plot

with the Bode plot results, the uncoated HVAF Hastelloy C276 sample exhibits the lowest impedance values in both real and imaginary part, among all five sample groups.

After the 21-day exposure period, the impedance of all sol–gel sealed samples shows a pronounced decline from Day 1 to Day 3, followed by a noticeably slower rate of decrease. Non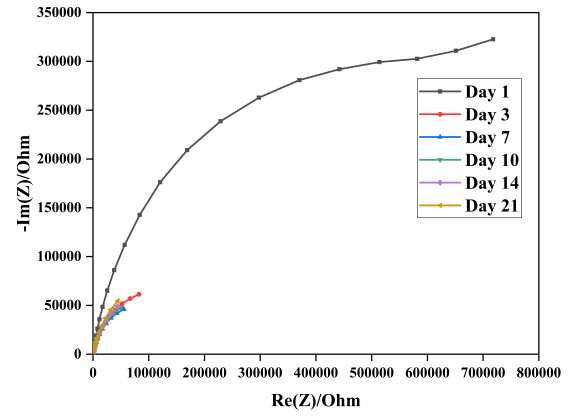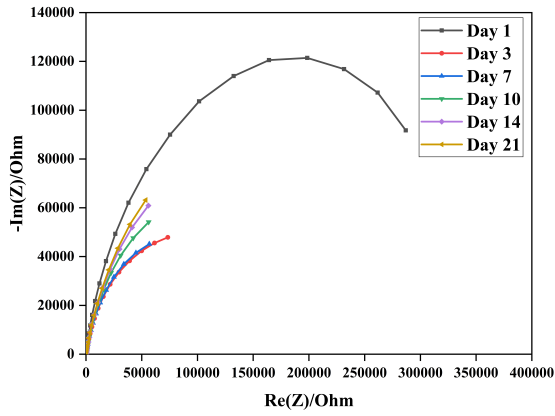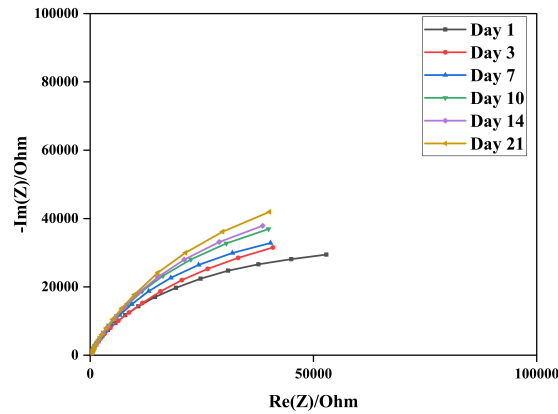etheless, even at the end of the test, all sol–gel sealed samples maintain slightly higher impedance values than the uncoated HVAF Hastelloy C276 sample.

Based on the analysis of the electrochemical results, it can be concluded that the SiO_2/ZrO_2 sol-gel sealing layer indeed demonstrates excellent stability and barrier properties in corrosive environments, confirming its potential as a protective coating. Furthermore, a positive correlation is observed between the number of sol-gel layers and electrochemical impedance: within the tested range, samples with more coating layers exhibited higher impedance values and lower corrosion rate, which enhanced the corrosion protection.

5.5 HIC RESISTANCE

After 96 hours of immersion testing, the sample surfaces appear as shown in Figure 47. It is evident that none of the samples' top surface exhibited blistering, which differs from the initial expectation. Originally, it was anticipated that the uncoated carbon steel S235JR sample would show blistering, while the samples coated with HVAF Hastelloy C276, HVAF Hastelloy C276 + two-layer SiO_2/ZrO_2 sol-gel, and HVAF Hastelloy C276 + five-layer SiO_2/ZrO_2 sol-gel would not consistent with the results reported in Winters' study [6]. However, in Winters' work, the NACE TM0284 standard test duration was extended to 240 hours. Therefore, it is reasonable to assume that the 96-hour immersion period used here was not sufficient for enough hydrogen atoms to diffuse into the steel lattice and accumulate as high-pressure hydrogen gas, which would typically lead to surface expansion or blistering.

No Coating

Only HVAF Hastelloy C276

HVAF Hastelloy C276 + 2-layer sol-gel SiO$_2$/ZrO$_2$

HVAF Hastelloy C276 + 5-layer sol-gel SiO$_2$/ZrO$_2$
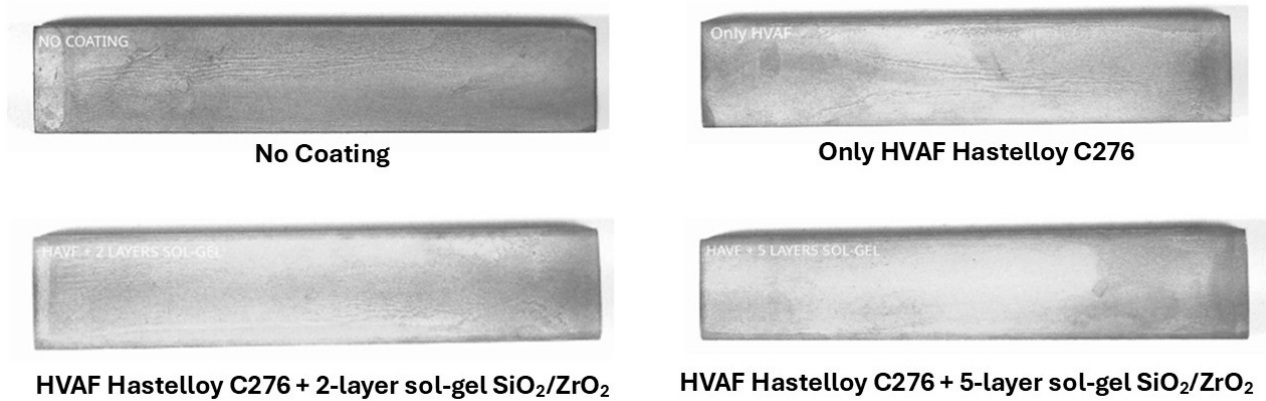
Figure 47: The top surface picture of the samples after immersion test.

Next, the samples were sectioned to observe crack formation in their cross sections and to calculate the CSR, CLR, and CTR. For each sample, three cross sectional measurements were taken, and their average values were used to determine the final results, as shown in Table 17. It is evident that the uncoated sample exhibited very high CSR, CLR, and CTR values, failing to meet the previously mentioned acceptance criteria for materials with good HIC resistance, specifically, CLR not higher than 15%, CSR not higher than 2%, and CTR not higher than 5%.

However, after applying coatings, the CSR, CLR, and CTR values for the other three samples dropped significantly. This indicates that the Hastelloy C276 coating notably improved the HIC resistance, keeping the CSR, CLR, and CTR well within the acceptable range. As illustrated in Figure 48, the three coated samples clearly exhibited shallower and shorter cracks compared to the uncoated one.

Surprisingly, among the coated samples, the one with only HVAF Hastelloy C276 showed the lowest CSR, CLR, and CTR values overall, indicating the best HIC resistance. It was followed by the HVAF Hastelloy C276 + five-layer SiO_2/ZrO_2 sol-gel sample, and finally the two-layer sol-gel sample. From these results, one could infer that adding a SiO_2/ZrO_2 sol-gel layer does not enhance HIC resistance—in fact, it might slightly diminish it. This could be because the Hastelloy C276 layer already offers excellent resistance on its own.

	CLR (%)	CSR (%)	CTR (%)
Carbon Steel S235JR Without Any Coating	37.8	4.0	11.9
Only HVAF Hastelloy C276 Coating	0.8	0.0	0.3
HVAF Hastelloy C276 + 2-layer SiO_2/ZrO_2	1.9	0.1	1.2
HVAF Hastelloy C276 + 5-layer SiO_2/ZrO_2	1.1	0.0	0.2

Table 17: Results of the values of CLR, CSR, and CTR
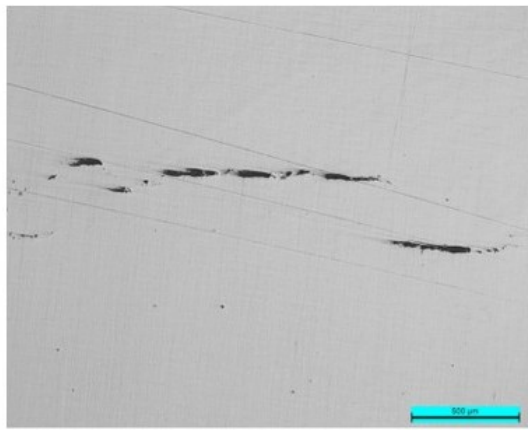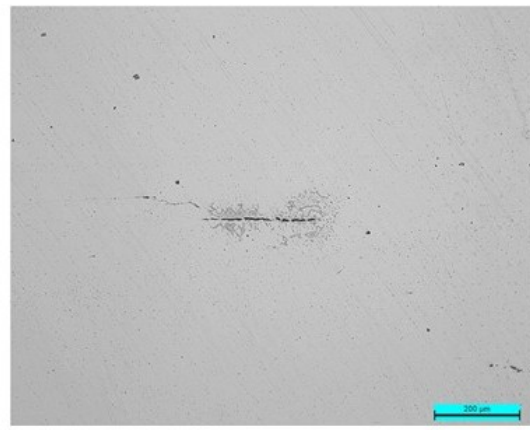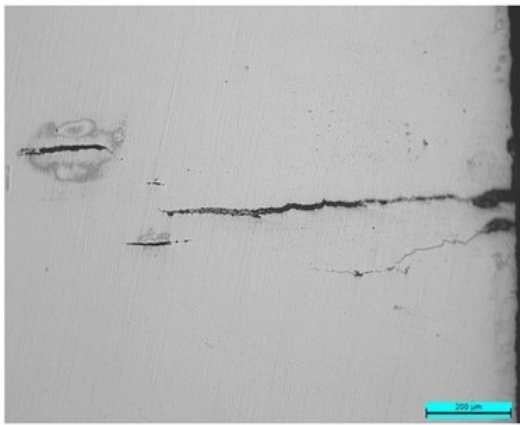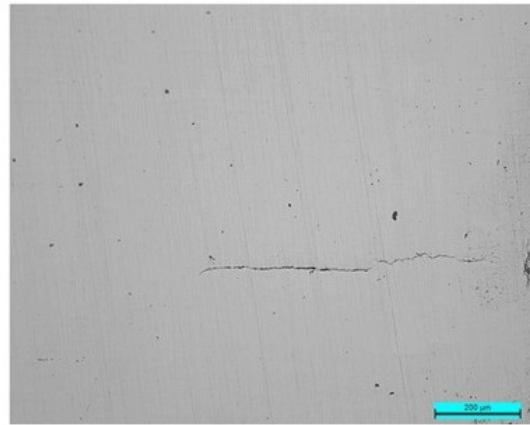
Figure 48: The cross section picture of the samples after immersion test.

That said, due to limitations in resources and cost, only one sample from each group was subjected to the HIC test. To definitively determine whether the SiO_2/ZrO_2 sol-gel layer has a negative impact on HIC resistance, or whether the observed differences in values were merely due to experimental error, future studies will need to include more extensive and repeated testing.

5.6 DISSCUSSION

By consolidating the final data for all tested properties, Table 18 provides a clear comparison of the microhardness, wear resistance, corrosion resistance, and HIC resistance among the no–sol-gel, two-layer sol–gel, and five-layer sol–gel sealing samples. In the table, green cells indicate improvements that enhance durability and thereby extend the lifespan of the underlying HVAF Hastelloy C276 coating, whereas red cells indicate negative effects on lifespan extension.

		No sol-gel → 2-layer sol-gel	No sol-gel → 5-layer sol-gel	2-layer sol-gel → 5-layer sol-gel
Mechanical Properties	Microhardness	+4.0 %	+5.7 %	+1.6 %
	Wear Rate	-8.0 %	-10.9 %	-3.1 %
Corrosion Resistance	Corrosion Rate	About 2.5 times lower	About 6 times lower	About 2 times lower
	Impedance in 21 days	5-layer sol-gel: Always the highest / No sol-gel: Always the lowest		
HIC Resistance	CLR	Increase	Increase	Decrease
	CSR	Increase	Almost the same	Decrease
	CTR	Increase	Decrease	Decrease

Table 18: Data comparison of measured properties among the three samples

The data presented in the Table 18 indicate that, in terms of wear resistance and microhardness, samples with the sol–gel sealing layer exhibit a slight improvement compared to those coated solely with the 250 μm Hastelloy C276 layer. This observation aligns with the previously discussed effect of the SiO_2/ZrO_2 sol–gel in partially filling surface pores, thereby reducing surface roughness. A smoother and more uniform surface facilitates more consistent sliding behavior and reduces uneven contact during indentation. However, while these mechanical properties show measurable gains, the magnitude of improvement remains modest. Electrochemical testing results demonstrate that, with respect to corrosion resistance in non-sulfide corrosive environments, the SiO_2/ZrO_2 sol–gel sealing layer effectively reduces corrosion rates and increases corrosion impedance, thereby enhancing overall corrosion resistance and extending the service life of both the coating and the substrate. These findings are consistent with those reported by Gkasiorek et al. [90]. Nevertheless, the present results reveal that the SiO_2/ZrO_2 sol–gel sealing layer offers no enhancement in HIC resistance. In fact, when applied in fewer layers, it may even have a detrimental effect, likely because the Hastelloy C276 coating alone already possesses inherently high resistance to HIC.

	Does the SiO₂/ZrO₂ sol-gel enhance this property?	Correlation with the number of sol-gel coating layers
Microhardness	Yes, a slight enhancement	Yes, a slight enhancement
Wear Resistance	Yes, a slight enhancement	Yes, a slight enhancement
Corrosion Resistance	Yes, a significant enhancement	Yes, a significant enhancement
HIC Resistance	For 2-layer sol-gel: Even worse For 5-layer sol-gel: No enhancement	Yes, a slight enhancement

Table 19: Summary of the final result

Table 19 summarizes the results presented in Table 18 in textual form. Overall, for all measured properties, the five-layer coating outperformed the two-layer coating, suggesting that, within a limited range of coating thicknesses, the number of SiO_2/ZrO_2 sol–gel sealing layers is positively correlated with the lifespan extension of the HVAF-sprayed Hastelloy C276 coating.

That said, SiO_2/ZrO_2 sol–gel sealing may not be the optimal choice for enhancing the lifespan of HVAF Hastelloy C276 in sulfur-rich environments. While slight improvements were observed in wear resistance and microhardness, the magnitude of these gains was modest, and the resistance to HIC showed no improvement, or even potential negative effects.

Nevertheless, experimental results confirm that the SiO_2/ZrO_2 sol–gel sealing layer provides highly effective protection for carbon steel equipment under general (non-sulfidic) corrosion conditions. When applied in environments exposed only to air rather than hydrogen sulfide, this sealing layer can substantially reduce corrosion rates. Combined with its low cost and ease of application, the SiO_2/ZrO_2 sol–gel sealing layer has strong potential for broader implementation in the petroleum industry.

6 CONCLUSION

From the results of this study, the following conclusions can be drawn:

- The SiO_2/ZrO_2 sol–gel sealing layer may not be the optimal choice for extending the service life of HVAF-sprayed Hastelloy C276 in H_2S-rich environments.

- The SiO_2/ZrO_2 sol–gel sealing layer provides only slight improvements in wear resistance and microhardness.

- No improvement in resistance to hydrogen induced cracking (HIC) was observed; in cases with fewer coating layers, potential adverse effects may occur.

- Under general conditions with exposure to air and moisture, the SiO_2/ZrO_2 sol–gel sealing layer can still offer effective corrosion protection for carbon steel equipment.

- Owing to its low cost, simple processing, and enhancement of corrosion resistance, the SiO_2/ZrO_2 sol–gel sealing layer retains substantial potential for widespread application in the petroleum industry.

7 RECOMMENDATIONS

Based on the findings of this study, it was concluded that the application of SiO_2/ZrO_2 sol-gel sealing layer does not significantly enhance the service life of HVAF sprayed Hastelloy C276 in hydrogen sulfide-rich environments. However, an unexpected observation was the sol-gel sealing layer's excellent performance in improving general corrosion resistance. These insights suggest three promising directions for future research: (1) developing alternative strategies to further extend the lifetime of HVAF Hastelloy C276 in H_2S environments, (2) optimizing sol-gel sealing layer's parameters to maximize general corrosion protection, and (3) exploring alternative materials or coating systems to replace HVAF Hastelloy C276 in sulfide-containing environments. Each direction is elaborated below.

Development of New Strategies to Extend the Lifespan of HVAF Hastelloy C276 in H_2S-Rich Environments

Future research can build upon the current work by investigating alternative materials or techniques beyond SiO_2/ZrO_2 sol-gel sealing layers. Several potential approaches including electrodeposited sealing layers to block H_2S diffusion, surface densification treatments to improve coating integrity, or the application of conformal nano-coatings via atomic layer deposition. While these methods were beyond the scope of the present study, they represent viable options that warrant further exploration and validation through targeted experimentation.

Optimization of Sol-Gel Sealants for General Corrosion Protection

Given the demonstrated improvement in general corrosion resistance, future work may focus on refining the sol-gel sealing strategy. This includes investigating the effect of additional coating layers (e.g., 1, 3, 7, or more layers) to determine whether corrosion resistance scales linearly or plateaus. Moreover, optimization of deposition techniques, such as dip coating, spin coating, or spray coating, could help improve uniformity and barrier performance. Exploring alternative sol-gel chemistries or compositions (e.g., TiO_2-based coatings) and comparing them with the current SiO_2/ZrO_2 system may also yield valuable insights.

Exploration of Alternatives to HVAF Hastelloy C276 in Sulfide-Rich Environments

Although HVAF sprayed Hastelloy C276 offers excellent protection against sulfide-induced corrosion, its high cost and process complexity limit large-scale industrial deployment. Thus, identifying alternative systems with comparable performance at reduced cost is a worthwhile objective. Potential solutions include thermal spray variants such as arc spray or HVOF combined with sol-gel sealing layers or vapor-deposited thin films (e.g., via physical vapor deposition (PVD) or chemical vapor deposition (CVD)), or the use of more economical alloys such as Inconel 625 in place of Hastelloy C276. The feasibility of these options remains uncertain and requires further literature review and experimental validation.

8 REFERENCES

[1] Mohammadtaghi Vakili, Petr Koutník, and Jan Kohout. Addressing hydrogen sulfide corrosion in oil and gas industries: A sustainable perspective. *Sustainability*, 16(4):1661, 2024.

[2] May L Martin and Petros Sofronis. Hydrogen-induced cracking and blistering in steels: A review. *Journal of Natural Gas Science and Engineering*, 101:104547, 2022.

[3] M.A. Tazelaar. Hydrogen induced cracking (HIC) stress oriented hydrogen induced cracking (SOHIC). *Shell Global Solutions International B.V., Amsterdam*, 2016.

[4] Abba A Abubakar, Abul Fazal M Arif, Khaled S Al-Athel, S Sohail Akhtar, and Javad Mostaghimi. Modeling residual stress development in thermal spray coatings: current status and way forward. *Journal of Thermal Spray Technology*, 26:1115–1145, 2017.

[5] N Espallargas. Introduction to thermal spray coatings. In *Future development of thermal spray coatings*, pages 1–13. Elsevier, 2015.

[6] Koen Winters. Effect of HVAF thermal sprayed NiCrMoW coating thickness on HIC resistance of carbon steels in sour environment, 2023.

[7] Xing Gao, Chang Li, Yan Xu, Xinxue Chen, and Xing Han. Effects of fuel types and process parameters on the performance of an activated combustion high velocity air-fuel (AC-HVAF) thermal spray system. *Journal of Thermal Spray Technology*, 30(7):1875–1890, 2021.

[8] Joseph R Davis et al. *Handbook of thermal spray technology*. ASM international, 2004.

[9] Jesper Vejlø Carstensen and Maria Lindegren. Quality control of thermal spray coatings in diesel engines. *Practical Metallography*, 50(6):369–390, 2013.

[10] S Smart, Shaomin Liu, JM Serra, JC Diniz Da Costa, A Iulianelli, and A Basile. Porous ceramic membranes for membrane reactors. In *Handbook of Membrane Reactors*, pages 298–336. Elsevier, 2013.

[11] Bertrand Faure, German Salazar-Alvarez, Anwar Ahniyaz, Irune Villaluenga, Gemma Berriozabal, Yolanda R De Miguel, and Lennart Bergström. Dispersion and surface functionalization of oxide nanoparticles for transparent photocatalytic and UV-protecting coatings and sunscreens. *Science and technology of advanced materials*, 14(2):023001, 2013.

[12] K Vignarooban, Xinhai Xu, K Wang, EE Molina, P Li, D Gervasio, and Arunachala Mada Kannan. Vapor pressure and corrosivity of ternary metal-chloride molten-salt based heat transfer fluids for use in concentrating solar power systems. *Applied Energy*, 159:206–213, 2015.

[13] Muhammad Wasim and Milos B Djukic. External corrosion of oil and gas pipelines: A review of failure mechanisms and predictive preventions. *Journal of Natural Gas Science and Engineering*, 100:104467, 2022.

[14] Satish Kumar Sharma and Sachin Maheshwari. A review on welding of high strength oil and gas pipeline steels. *Journal of Natural Gas Science and Engineering*, 38:203–217, 2017.

[15] Roman Bender, Damien Féron, Douglas Mills, Stefan Ritter, Ralph Bäßler, Dirk Bettge, Iris De Graeve, Arne Dugstad, Sabrina Grassini, Theo Hack, et al. Corrosion challenges towards a sustainable society. *Materials and corrosion*, 73(11):1730–1751, 2022.

[16] MB Kermani and Don Harrop. The impact of corrosion on the oil and gas industry. *SPE Production & Facilities*, 11(03):186–190, 1996.

[17] Gyu Tae Park, Sung Ung Koh, Hwan Gyo Jung, and Kyoo Young Kim. Effect of microstructure on the hydrogen trapping efficiency and hydrogen induced cracking of linepipe steel. *Corrosion science*, 50(7):1865–1871, 2008.

[18] Branko N Popov, Jong-Won Lee, and Milos B Djukic. Hydrogen permeation and hydrogen-induced cracking. In *Handbook of environmental degradation of materials*, pages 133–162. Elsevier, 2018.

[19] Roger A King. Sulfide stress cracking. *Trends in oil and gas corrosion research and technologies*, pages 271–294, 2017.

[20] Shao-Wei Huang, Jin-Tai Luo, Zhang-Hong Chang, Ting-En Shen, Jui-Ting Liang, Wei-Lin Hsu, Che-Wei Tsai, and Jien-Wei Yeh. Dual coating layers to enhance oxidation resistance for refractory high-entropy alloys. *Results in Materials*, 21:100508, 2024.

[21] Tee L Guidotti. Hydrogen sulfide intoxication. In *Handbook of clinical neurology*, volume 131, pages 111–133. Elsevier, 2015.

[22] Tzouliana Kraia, Georgios Varvoutis, George E Marnellos, and Michalis Konsolakis. Unveiling the role of in situ sulfidation and H_2O excess on H_2S decomposition to carbon-free H_2 over cobalt/ceria catalysts. *Catalysts*, 13(3):504, 2023.

[23] Lei Fu and Hongyuan Fang. Formation criterion of hydrogen-induced cracking in steel based on fracture mechanics. *Metals*, 8(11):940, 2018.

[24] NN Sergeev, AN Sergeev, SN Kutepov, AG Kolmakov, and AE Gvozdev. Mechanism of the hydrogen cracking of metals and alloys, part I. *Inorganic Materials: Applied Research*, 10:24–31, 2019.

[25] M Elboujdaini, VS Sastri, and JR Perumareddi. Studies on inhibition of hydrogen-induced cracking of linepipe steels. *Corrosion*, 62(1):29–34, 2006.

[26] Houyi Ma, Xiaoliang Cheng, Guiqiu Li, Shenhao Chen, Zhenlan Quan, Shiyong Zhao, and Lin Niu. The influence of hydrogen sulfide on corrosion of iron under different conditions. *Corrosion science*, 42(10):1669–1683, 2000.

[27] MA Lucio-Garcia, JG Gonzalez-Rodriguez, M Casales, L Martinez, JG Chacon-Nava, MA Neri-Flores, and A Martinez-Villafañe. Effect of heat treatment on H_2S corrosion of a micro-alloyed C-Mn steel. *Corrosion Science*, 51(10):2380–2386, 2009.

[28] Wan Keun Kim, Seong Ung Koh, Boo Young Yang, and Kyoo Young Kim. Effect of environmental and metallurgical factors on hydrogen induced cracking of HSLA steels. *Corrosion Science*, 50(12):3336–3342, 2008.

[29] WJ Liu. Modeling nucleation of hydrogen induced cracking in steels during sour service. In *Materials Science Forum*, volume 675, pages 983–986. Trans Tech Publ, 2011.

[30] Samerjit Homrossukon, Sheldon Mostovoy, and Judith A Todd. Investigation of hydrogen assisted cracking in high and low strength steels. 2009.

[31] Behrooz Beidokhti, A Dolati, and AH Koukabi. Effects of alloying elements and microstructure on the susceptibility of the welded HSLA steel to hydrogen-induced cracking and sulfide stress cracking. *Materials Science and Engineering: A*, 507(1-2):167–173, 2009.

[32] Richard J Pargeter. Susceptibility to SOHIC for linepipe and pressure vessel steels-review of current knowledge. *NACE CORROSION*, pages NACE–07115, 2007.

[33] MG Isakov, VI Izotov, VA Karpel'ev, and GA Filippov. Kinetics of the damage formation in a low-carbon low-alloy steel upon hydrogenation. *The Physics of Metals and Metallography*, 90(3):302–308, 2000.

[34] Marie C Tiegel, May L Martin, Annegret K Lehmberg, Martin Deutges, Christine Borchers, and Reiner Kirchheim. Crack and blister initiation and growth in purified iron due to hydrogen loading. *Acta Materialia*, 115:24–34, 2016.

[35] Sagar Amin, Hemant Panchal, et al. A review on thermal spray coating processes. *transfer*, 2(4):556–563, 2016.

[36] Maher I Boulos, Pierre L Fauchais, and Joachim VR Heberlein. *Thermal spray fundamentals: from powder to part.* Springer, 2021.

[37] Rajeev Dhiman, André G McDonald, and Sanjeev Chandra. Predicting splat morphology in a thermal spray process. *Surface and Coatings Technology*, 201(18):7789–7801, 2007.

[38] Esmaeil Sadeghi, Nicolaie Markocsan, and Shrikant Joshi. Advances in corrosion-resistant thermal spray coatings for renewable energy power plants: Part II—effect of environment and outlook. *Journal of Thermal Spray Technology*, 28:1789–1850, 2019.

[39] Monica Campo, Monica Carboneras, MD López, Belen Torres, P Rodrigo, Enrique Otero, and J Rams. Corrosion resistance of thermally sprayed Al and Al/SiC coatings on Mg. *Surface and Coatings Technology*, 203(20-21):3224–3230, 2009.

[40] D Zhang, SJ Harris, and DG McCartney. Microstructure formation and corrosion behaviour in HVOF-sprayed Inconel 625 coatings. *Materials Science and Engineering: A*, 344(1-2):45–56, 2003.

[41] S Deshpande, S Sampath, and H Zhang. Mechanisms of oxidation and its role in microstructural evolution of metallic thermal spray coatings—case study for Ni-Al. *Surface and Coatings Technology*, 200(18-19):5395–5406, 2006.

[42] C Vinoth Kumar, G Rajyalakshmi, and Jessica Kartha. Insights on anti-corrosion coating of magnesium alloy: a review. *Journal of Bio-and Tribo-Corrosion*, 9(1):13, 2023.

[43] Imhade P Okokpujie, Lagouge K Tartibu, Hameed O Musa-Basheer, and AOM Adeoye. Effect of coatings on mechanical, corrosion and tribological properties of industrial materials: a comprehensive review. *Journal of Bio-and Tribo-Corrosion*, 10(1):2, 2024.

[44] Jayant Gopal Thakare, Chandan Pandey, MM Mahapatra, and Rahul S Mulik. Thermal barrier coatings—a state of the art review. *Metals and Materials International*, 27:1947–1968, 2021.

[45] Behzad Fotovvati, Navid Namdari, and Amir Dehghanghadikolaei. On coating techniques for surface protection: A review. *Journal of Manufacturing and Materials processing*, 3(1):28, 2019.

[46] Jianyong Yang, Hua Liu, Wen Gao, Linfen Su, and Kaiyong Jiang. Effect of different fillers on the microstructural evolution and high temperature oxidation resistance of Mo-Si-B coatings prepared by pack cementation. *International Journal of Refractory Metals and Hard Materials*, 100:105625, 2021.

[47] A López-Ortega, R Bayón, and JL Arana. Evaluation of protective coatings for offshore applications. corrosion and tribocorrosion behavior in synthetic seawater. *Surface and Coatings Technology*, 349:1083–1097, 2018.

[48] Mario Rosso, A Scrivani, Daniele Ugues, and S Bertini. Corrosion resistance and properties of pump pistons coated with hard materials. *International Journal of Refractory Metals and Hard Materials*, 19(1):45–52, 2001.

[49] J Knuuttila, P Sorsa, T Mäntylä, J Knuuttila, and P Sorsa. Sealing of thermal spray coatings by impregnation. *Journal of thermal spray technology*, 8:249–257, 1999.

[50] HZ Ye, DY Li, and RL Eadie. Influences of porosity on mechanical and wear performance of pseudoelastic TiNi-matrix composites. *Journal of materials engineering and performance*, 10:178–185, 2001.

[51] OC Brandt. Mechanical properties of HVOF coatings. *Journal of Thermal Spray Technology*, 4(2):147–152, 1995.

[52] Q Chen, DY Li, and Bruce Cook. Is porosity always detrimental to the wear resistance of materials?—a computational study on the effect of porosity on erosive wear of TiC/Cu composites. *Wear*, 267(5-8):1153–1159, 2009.

[53] T Vans, E Rajamaki, and K Korpiola. Mechanical properties of thermal spray coatings. 2001.

[54] Narayanasamy Pandiyarajan and Peerawatt Nunthavarawong. Recent advancements in sealants solutions for surface coatings: A comprehensive review. *Journal of Bio-and Tribo-Corrosion*, 10(3):61, 2024.

[55] B Wielage, U Hofmann, S Steinhauser, and Gi Zimmermann. Improving wear and corrosion resistance of thermal sprayed coatings. *Surface engineering*, 14(2):136–138, 1998.

[56] Jacques Livage. Sol-gel processes. *Current Opinion in Solid State and Materials Science*, 2(2):132–138, 1997.

[57] Sumio Sakka. *Handbook of sol-gel science and technology. 1. Sol-gel processing*, volume 1. Springer Science & Business Media, 2005.

[58] C Jeffrey Brinker and George W Scherer. *Sol-gel science: the physics and chemistry of sol-gel processing*. Academic press, 2013.

[59] Serena Esposito. "traditional" sol-gel chemistry as a powerful tool for the preparation of supported metal and metal oxide catalysts. *Materials*, 12(4):668, 2019.

[60] Mei Yu, Huan Dong, Haobo Shi, Liangliang Xiong, Chong He, Jianhua Liu, and Songmei Li. Effects of graphene oxide-filled sol-gel sealing on the corrosion resistance and paint adhesion of anodized aluminum. *Applied Surface Science*, 479:105–113, 2019.

[61] Rita B Figueira. Hybrid sol-gel coatings for corrosion mitigation: A critical review. *Polymers*, 12(3):689, 2020.

[62] A Venkateswara Rao, Sanjay S Latthe, Satish A Mahadik, and Charles Kappenstein. Mechanically stable and corrosion resistant superhydrophobic sol-gel coatings on copper substrate. *Applied Surface Science*, 257(13):5772–5776, 2011.

[63] Levich Landau and B Levich. Dragging of a liquid by a moving plate. In *Dynamics of curved fronts*, pages 141–153. Elsevier, 1988.

[64] Per Møller and Lars Pleht Nielsen. *Advanced surface technology*. Møller & Nielsen, 2013.

[65] Monica Trueba and Stefano P Trasatti. γ-alumina as a support for catalysts: a review of fundamental aspects. *European journal of inorganic chemistry*, 2005(17):3393–3403, 2005.

[66] Gabriela Aristia, Le Quynh Hoa, Marianne Nofz, Regine Sojref, and Ralph Bäßler. Study of Al_2O_3 sol-gel coatings on X20Cr13 in artificial north german basin geothermal water at 150° c. *Coatings*, 11(5):526, 2021.

[67] Dongjiang Zhang, Rui Yu, Xuelei Feng, Xuncheng Guo, Yongkang Yang, and Xiqing Xu. Enhanced mechanical properties of Al_2O_3 nanoceramics via low temperature spark plasma sintering of amorphous powders. *Materials*, 16(16):5652, 2023.

[68] Ashleigh E Danks, Simon R Hall, and ZJMH Schnepp. The evolution of 'sol-gel'chemistry as a technique for materials synthesis. *Materials Horizons*, 3(2):91–112, 2016.

[69] R Hofman, JGF Westheim, T Fransen, and PJ Gellings. Improved SiO_2-coatings against high temperature sulphidation by internal stress reduction. *Le Journal de Physique IV*, 3(C9):C9–865, 1993.

[70] Qunfeng Zeng. Thermal stability and high-temperature super low friction of γ-Fe_2O_3@SiO_2 nanocomposite coatings on steel. *Lubricants*, 12(6):223, 2024.

[71] Zhuangzhuang Han, Jian Yuan, Peijing Tian, Bing Liu, Jinqi Tan, and Qi Zhang. Preparation of highly transparent and wear-resistant SiO_2 coating by alkali/acid dual catalyzed sol-gel method. *Journal of Materials Research*, 38(13):3316–3323, 2023.

[72] Joachim Gross, Gudrun Reichenauer, and Jochen Fricke. Mechanical properties of SiO_2 aerogels. *Journal of Physics D: Applied Physics*, 21(9):1447, 1988.

[73] Wei Wei Sun, Mu Qin Li, Yan Gao, and Jiang Liu. Double sealing of ultrasonic micro-arc oxidation coating on pure magnesium by nano-SiO_2 particles and SiO_2 sol sealing agent. *Advanced Materials Research*, 1030:48–51, 2014.

[74] Liu Jianguo, Gong Gaoping, and Yan Chuanwei. Enhancement of the erosion–corrosion resistance of Dacromet with hybrid SiO_2 sol–gel. *Surface and Coatings Technology*, 200(16-17):4967–4975, 2006.

[75] RG Munro and SJ Dapkunas. Corrosion characteristics of silicon carbide and silicon nitride. *Journal of research of the National Institute of Standards and Technology*, 98(5):607, 1993.

[76] M Herrmann, J Schilm, G Michael, J Meinhardt, and R Flegler. Corrosion of silicon nitride materials in acidic and basic solutions and under hydrothermal conditions. *Journal of the European Ceramic Society*, 23(4):585–594, 2003.

[77] Qian JIANG, Guizhi ZHU, Jiawei CHEN, Hong QI, and Nanping XU. Corrosion resistance of ZrO_2 nanofiltration membranes. *Journal of the Chinese Ceramic Society*, 41(12):1632–1637, 2013.

[78] Maik Finsel, Maria Hemme, Sebastian Döring, Jil SV Rüter, Gregor T Dahl, Tobias Krekeler, Andreas Kornowski, Martin Ritter, Horst Weller, and Tobias Vossmeyer. Synthesis and thermal stability of ZrO_2@SiO_2 core-shell submicron particles. *RSC advances*, 9(46):26902–26914, 2019.

[79] Bing Zhang, Ruohan Xia, Yao Yan, Jia Liu, and Zisheng Guan. Highly transparent and zirconia-enhanced sol-gel hybrid coating on polycarbonate substrates for self-cleaning applications. *Materials*, 16(8):3138, 2023.

[80] Ognian Dimitrov, Irina Stambolova, Sasho Vassilev, Katerina Lazarova, Tsvetanka Babeva, and Ralitsa Mladenova. Surface and morphological features of ZrO_2 sol-gel coatings obtained by polymer modified solution. *Materials Proceedings*, 2(1):6, 2020.

[81] Jolanta Szczurek, Anna Gąsiorek, Anna Szczurek, Bartosz Babiarczuk, Maciej Kowalski, Paweł Karolczak, Walis Jones, Roman Wróblewski, Jakub Adamek, Artur Maciej, et al. Changes in protective properties of zirconia and silica sol-gel layers over time. *Surface and Coatings Technology*, 455:129220, 2023.

[82] Mohamed Atik and Michel A Aegerter. Corrosion resistant sol-gel ZrO_2 coatings on stainless steel. *Journal of non-crystalline solids*, 147:813–819, 1992.

[83] Luciano Velardi, Luigi Scrimieri, Antonio Serra, Daniela Manno, and Lucio Calcagnile. Effect of temperature on the physical, optical and photocatalytic properties of TiO_2 nanoparticles. *SN Applied Sciences*, 2:1–6, 2020.

[84] Imran Ali, Mohd Suhail, Zied A Alothman, and Abdulrahman Alwarthan. Recent advances in syntheses, properties and applications of TiO_2 nanostructures. *RSC advances*, 8(53):30125–30147, 2018.

[85] Caide Fan, Jialu Lu, Chengjie Duan, Chengbin Wu, Jiming Lin, Ruoxiang Qiu, Zehui Zhang, Jianming Yang, Bin Zhou, and Ai Du. Effect of titanium dioxide particles on the thermal stability of silica aerogels. *Nanomaterials*, 14(15):1304, 2024.

[86] Carol Sippel, Waleska Campos Guaglianoni, and Carlos Pérez Bergmann. Titanium dioxide nanomaterials for renewable energy applications. *Environmental Applications of Nanomaterials*, pages 73–96, 2022.

[87] Nelly Boshkova, Irina Stambolova, Daniela Stoyanova, Silviya Simeonova, Nikolay Grozev, Georgi Avdeev, Maria Shipochka, Ognian Dimitrov, Vasil Bachvarov, Miglena Peshova, et al. Protective characteristics of TiO_2 sol-gel layer deposited on Zn-Ni or Zn-Co substrates. *Coatings*, 13(2):295, 2023.

[88] Zhang Na, Yu Shengxue, Xing Qian, Chen Xiaolei, Zhang Mingxian, and Shen Dejiu. Corrosion performance of composite MAO TiO_2 sol-gel coatings on magnesium alloy AZ91D. *Journal of Materials Engineering and Performance*, 27:6080–6086, 2018.

[89] Behnam Abdollahi, Daryoush Afzali, and Zahra Hassani. Corrosion inhibition properties of SiO_2-ZrO_2 nanocomposite coating on carbon steel 178. *Anti-Corrosion Methods and Materials*, 65(1):66–72, 2018.

[90] Jolanta Gąsiorek, Anna Mazur-Nowacka, Anna Szczurek, Bartosz Babiarczuk, Wilhelm Jan Tic, Joanna Guziałowska-Tic, Jerzy Kaleta, and Justyna Krzak. Influence of zirconia and organic additives on mechanical and electrochemical properties of silica sol-gel coatings. *Materials*, 14(9):2389, 2021.

[91] Sigamani Saravanan and Raghvendra S Dubey. Fabrication, characterization of TiO_2/SiO_2 multilayers using sol-gel spin coating method. *: , , ,* 10(1):63–69, 2019.

[92] S Vives and Cathy Meunier. Mixed SiO_2–TiO_2 (1: 1) sol-gel films on mild steel substrates: Sol composition and thermal treatment effects. *Surface and Coatings Technology*, 202(11):2374–2378, 2008.

[93] Manuel Gutierrez Martinez, Lizangela Guerra, Barbara Bermudez Reyes, Roberto Cabriales, and Luis A Reyes. Characterization of SiO_2-TiO_2 coatings on 316L stainless steel substrates. *Journal of Advanced Materials and Processing*, 6(1):3–13, 2018.

[94] Abderraouf Madjdi Mebarek, Mounira Bourebia, Lakhdar Laouar, and Nassim Bouchelaghem. Effect of ball burnishing process on surface roughness and corrosion behavior of S235JR steel. *The International Journal of Advanced Manufacturing Technology*, 130(7):3431–3444, 2024.

[95] Paweł Grzegorz Kossakowski. Simulation of ductile fracture of S235JR steel using computational cells with microstructurally-based length scales. *Journal of theoretical and applied mechanics*, 50(2):589–607, 2012.

[96] Alicja K Krella, Dominika E Zakrzewska, and Artur Marchewicz. The resistance of S235JR steel to cavitation erosion. *Wear*, 452:203295, 2020.

[97] Denny A Jones. Principles and prevention. *Corrosion*, 2:168, 1996.

[98] John W Oldfield. Electrochemical theory of galvanic corrosion. In *Galvanic corrosion*. ASTM International, 1988.

[99] XG Zhang. Galvanic corrosion. *Uhlig's Corrosion Handbook*, 51:123, 2011.

[100] Shiladitya Paul. Corrosion of carbon steel in supercritical CO_2/H_2S and its mitigation using coatings. In *NACE CORROSION*, pages NACE–2019. NACE, 2019.

[101] Hong Shi, Zhigang Gao, Zhongbiao Fan, Yuanyuan Ding, Yanxin Qiao, and Zhiyuan Zhu. Corrosion behavior of alloy C-276 in supercritical water. *Advances in Materials Science and Engineering*, 2018(1):1027640, 2018.

[102] James R Crum, Brian A Baker, Debajyoti Maitra, and Julian Roberts. Custom cold working of nickel alloy tubulars for size, strength and corrosion resistance. In *NACE CORROSION*, pages NACE–2013. NACE, 2013.

[103] Virgínia Bertolo, Quanxin Jiang, Sebastian Scholl, Roumen H Petrov, Ude Hangen, Carey Walters, Jilt Sietsma, and Vera Popovich. A comprehensive quantitative characterisation of the multiphase microstructure of a thick-section high strength steel. *Journal of Materials Science*, 57(13):7101–7126, 2022.